Transmembrane molecular machines

Matthew A. Watson

Thesis presented for the degree of

Doctor of Philosophy

The University of Edinburgh

2014

Declaration

I declare that this thesis is written by myself and that the work presented here is entirely my own, except where indicated in the text. The work was carried out in the School of Chemistry at the University of Edinburgh. It has not been submitted in part, or in a whole, for any other degree.

Matthew A. Watson
June 2014

Acknowledgements

First and foremost I must thank Dr Scott Cockroft for taking me on to study for my PhD in his group – in addition to being engaging, inspiring and helpful he is trusting and egalitarian, all of which have made my experience in the group very instructive, constructive and rewarding. I am grateful to all the members of the group for their parts in creating the convivial atmosphere that we work in everyday, in the order that I encountered them – James Brown, Lina Mati, Lixu Yang, John Brazier, Cath Adam, Michael Ochsenkuehn, Tom Hubbard, Kamila Muchowska, Justinas Slikas, Nicholas Dominelli Whiteley and Antoine Bader. I'm looking forward to continuing to work with and alongside you in the near future. Thanks to the University of Edinburgh for providing the fertile soil in which we grow the tree of knowledge. I am of course indebted to my family particularly to my Mother for my life, to both her and my father for my genetic predispositions and quirks of which I am proud. My sisters and brothers make me feel admired and loved as much as I love and admire them. And to all my friends without whom I would be lost indeed.

Alexa with whom I love more each day, thank you.

Finally I am grateful to the EPSRC for providing the funding that allowed me to conduct my PhD.

Abstract

Transmembrane molecular machines are ubiquitous in nature. These evolved systems demonstrate superlative elegance and efficiency of operation. Imitation and hijacking of biological components such as proteins and DNA has emerged as a means of imparting desirable characteristics to rationally designed synthetic molecular machines. This thesis presents work towards various synthetic transmembrane molecular machines based on alpha-haemolysin (α-HL).

Chapter One reviews progress towards synthetic transmembrane machines, introducing natural examples, defining criteria for being ‘a molecular machine’ cataloguing examples and trends in synthetic molecular machines in solution, on surfaces and in membranes. Examples are evaluated in terms of their machine like behaviour and α-HL emerges as a particularly promising component in the development of synthetic transmembrane molecular machines.

Chapter Two examines solvent isotope effects resulting from substitution of hydrogen by deuterium in water at the nanoscale – on the rates of transmembrane ion transport and transmembrane translocation of ssDNA through α-HL, both of which are of concern in the context of building molecular machines which use α-HL as a component.

Chapters Three to Six look at different machine applications of related transmembrane architectures based on individual transmembrane rotaxanes constructed in α-HL from DNA/PEG copolymer ‘thread’ strands and DNA ‘primer’ strands.

Chapter Three uses this approach to observe translational motion of the thread strand in both directions along the z-axis due to nucleotide incorporation and pyrophosphorolysis in real-time with single-nucleotide resolution.

Chapter Four provides the first demonstration of asymmetrical, hysteretic cyclical behaviour in the translational motion of the thread strand by incorporation of a nicking site which resets the system after nucleotide incorporations have occurred.

Chapter Five introduces a novel variant of the rotaxane architecture using a circularised primer strand which allows real time observation of rolling circle amplification at the single molecule level by coupling the process to the unidirectional translocation of the thread strand.

Chapter Six considers the use of the vestibule of α-HL as a transmembrane DNA ligase mimic with the DNA thread/primer complex as substrate.

List of Abbreviations

α-HL	Alpha-haemolysin
Ac	acetate
AcOH	Ethanoic acid
ADP	Adenosine diphosphate
ATP	Adenosine triphosphate
BHMM	Bayeesian hidden Markov model
BSA	Bovine serum albumin
CPG	Controlled porosity glass
C-P-Q	Carotenoid-porphyrin-quinone
DMT	dimethoxytrityl
dNTP	Deoxynucleotide triphosphate
dsDNA	Double stranded DNA
MeCN	Acetonitrile
NEB	New England Biolabs
PAGE	Polyacrylamide gel
PEG^{phos}	Polyethylene glycol
P_i	Inorganic phosphate
PP_i	Pyrophosphate
QS	Quick-stick DNA ligase
RCA	Rolling circle amplification
RTX	Rotaxane
smRCA	Single molecule rolling circle
ssDNA	Single stranded DNA
TEAA	Triethylammonium acetate
T_m	Melting temperature

Lay Summary

Life depends on the operation of billions of proteins some of which behave like machines – in that they consume fuel and do work, such as pumping molecules into and out of cells. In chemistry and biology there is a drive to understand the operation of such machines and to mimic their operation in artificial systems with novel function. This thesis reviews the natural inspiration for and the progress on artificial systems, with a focus on the systems that operate at the membrane interface between chemically distinct compartments. It then goes on to present designs and demonstrations of the operation of some recently invented systems that mimic natural counterparts.

The work has implications for the future design and development of so-called molecular machines which constitute an increasingly studied field of research with far reaching potential to affect all areas of human endeavour.

Contents

Chapter One

Towards synthetic transmembrane molecular machines

Abstract

Nature’s molecular machines are a constant source of inspiration for the chemist. These hierarchically structured protein and nucleic acid-based machines facilitate the relative placement of atoms to ‘tolerances much smaller than the radius of the atom’[1], for example in the synthesis of small molecules involved in cellular function. Evolution has led to the proliferation of diverse natural molecular machines whose interplay make up life[2]. In the construction of synthetic systems there is an analogous ‘evolutionary’ process. From the initial idea to mimic the molecular machines of nature, different approaches have led to separate branches of research. The branches exhibit different inherent levels of complexity and scope from small two-state switchable molecules in solution[3,4] and on surfaces[5,6], to natural molecular machines that have been modified to give improved or novel functions[7,8,9].

One feature of many natural molecular machines is their association with biopolymers which restrict the degrees of freedom in which they can move in response to the Brownian regime of the cell[10,11]. This has been mimicked in the construction of synthetic molecular machines based on rotaxanated or catenated architectures which similarly restrict the degrees of freedom available to their constituent parts[12], biological molecules such as DNA have been repurposed as diverse molecular machines[13,14,15,16] combinations of enzymes that have been entrained on polymeric molecular scaffolds of synthetic or biological origin afford better kinetics in multi-step reactions than the same enzymes do diffusing freely in solution[17,18].

Many natural molecular machines function only when incorporated into lipid bilayer membranes[19,20]. This allows the molecular machines in question to exploit the chemical or potential gradients between spatially close but chemically distinct environments to fuel part of their work cycle[21,22]. Incorporation into artificial or biological membranes thereby presents an easily realisable route to constructing sophisticated synthetic transmembrane molecular machines.

This chapter is currently being drafted for submission to *Chemical Society Reviews*.

1.1 Nature's molecular machines

Life on Earth is composed of the interplay of what can be considered as billions of molecular machines[23]. Each of these natural molecular machines operate in an energetic environment where the dominant energetic factors on the length scale of the biomolecules are random thermal fluctuations[24]. Indeed, it has been said that proteins are 'kicking screaming stochastic molecules'[25]. The surface presented by the enzyme to the bulk and hence to substrate molecules is moving rapidly on the picosecond timescale due to thermal forces (Figure 1.1a). If an enzyme and a substrate randomly approach each other in the correct orientation they are able recognise each other. Mutual compatibility between the steric bulk, hydrophobicity, charge, and hydrogen–bonding sites on a substrate and enzyme allows the substrate molecule to be isolated from the random thermal forces of the bulk (Figure 1.1b). Once an enzyme complex is formed, this pairing is entropically 'funnelled' towards having an increasing probability of molecular fragments being brought into the correct orientation and with sufficient energy to react in the active site of the enzyme[26].

The constant fluctuation of the enzyme leads to a range of energetic states for the enzyme-substrate complex, tuning the energy barrier between the initial complex energy maxima, the transition state energy minima and the complex energy maxima post reaction[26b] (Figure 1.1c). The rate of reaction and position of the equilibrium is often limited by the rates of diffusion and concentrations of the substrates, enzymes and products. For freely diffusing enzymes catalysing the turn-over of freely diffusing substrates, the rates of fluctuation are governed by the temperature and hence the amount of time that the system is arranged in a condition in which the components can react.

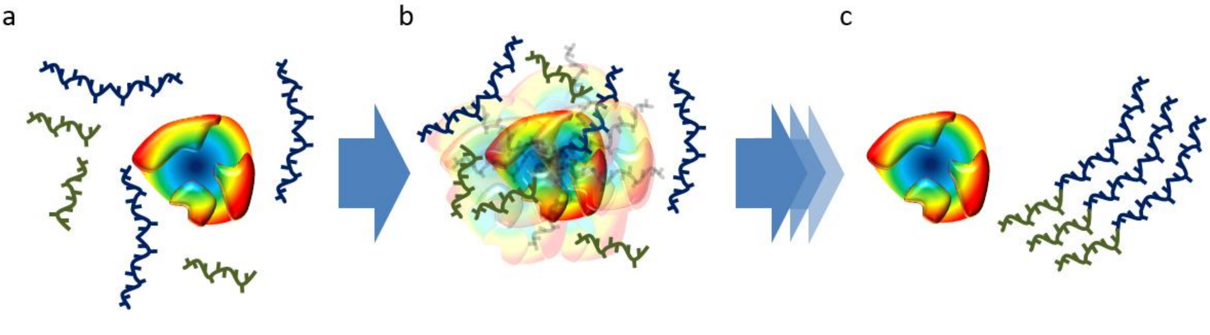

Figure 1.1 Cartoon of an enzyme catalysing the reaction between two biopolymers. The colour map of the enzyme represents the interaction energy penalty incurred for association of the reactants with the surface of the enzyme, the 'bottom of the funnel' is shown in blue. Association of the reactants and the enzyme is often entropically favoured by the displacement of water molecules into the bulk.

A. Linearly processive nucleic acid-manipulating molecular motors

It is clear that entropic fluctuations at the molecular level constitute one of the greatest challenges that the evolution of life has had to overcome. Yet, despite this constant Brownian buffeting, many of life's fundamental reactions are both highly processive and rapid. In response, numerous biomolecular motors have evolved to counteract this entropic challenge by acting in linearly processive modes on polymeric substrates. As a result, and despite billions of years of evolution from shared ancestral forms, a surprisingly high degree of structural homology exists between molecular machines found in different species[2, 19]. In fact, it is these molecular machines on which the central dogma of biology rests[27] (Figure 1.2). In short, DNA is maintained and manipulated by motor proteins such as polymerases[28,29] and helicases[30], which processively translocate along their linear DNA tracks at rates of up to 38 bases per second[31]. This genetic information is transcribed by similarly processive RNA polymerase enzymes into mRNA strands that is then translated by the ribosomal complex into peptides which are then folded into their active 3D conformations by solvophobic self-assembly or by ATP fuelled chaperonins (Figure 1.2d).

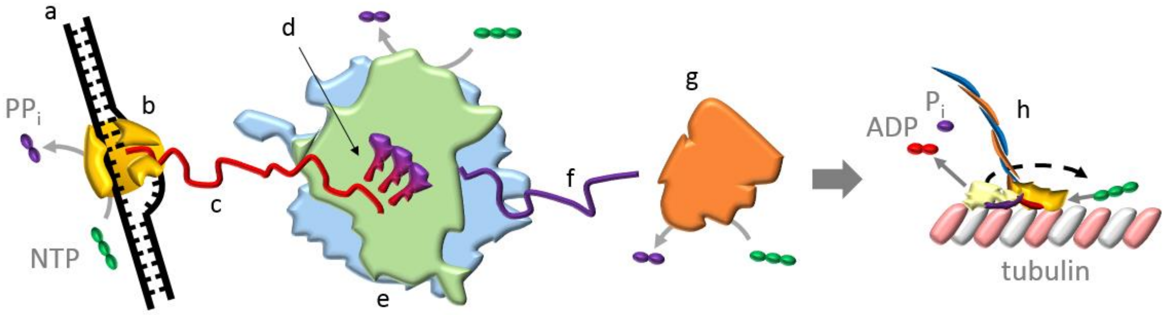

Figure 1.2 The central dogma of biology[1]. Double-stranded DNA helix **a** is transcribed by RNA polymerase **b** into mRNA **c** which is then associated with amino acid bearing tRNAs **d** in the active site of the ribosome complex **e**. Here the ribosome transcribes the RNA into protein by using energy from the bond in GTP to catalyse the formation of peptide bonds between adjacent amino acid residues at the expense of the bond between the tRNA and the amino acid. The growing peptide chains **f** pass to chaperonins **g** which use ATP to drive a cycle of conformational change that results in the folding of the nascent peptide chain into a functional protein that might form part of a motor protein such as kinesin **h**.

B. The ribosomal protein factory

The translation of an mRNA transcript by ribosomal molecular machinery during the synthesis of polypeptides is perhaps the most impressive example of a natural molecular machine. A detailed explanation of the structure[32] and function[33] of the ribosomal complex are beyond the scope of this review, but the basic operation of the ribosome can be simply understood in terms of a work cycle. The work cycle depends on the reversible non-covalent association of protein and RNA components (ribosomal subunits) with linear messenger ribonucleic acid polymer substrates (mRNA) and transfer ribonucleic acids (tRNA) bearing amino acid monomers (Figure 1.2d)[32,34]. This assembly undergoes cycles of conformational change driven by tRNA binding, GTP binding, hydrolysis and release. This process drives peptide bond formation between adjacent associated amino acid monomers and ratcheting of the complex along the substrate polymer with extrusion of the growing polypeptide chain (Figure 1.2f). The extruded protein sequences fold into three-dimensional protein structures (perhaps with assistance of ATP-fuelled chaperonins[35] as shown in Figure 1.2g), which themselves might be involved in manipulating DNA, or in transporting molecular cargoes within cells[36] and through lipid membranes[37]. Since the ribosome produces all of the known proteinaceous molecular machines found in nature, the entire process can be likened to a self-replicating robotic assembly line.

C. Protein walkers

Another class of linearly processive, yet functionally distinct enzymes are the myosin and kinesin motor proteins,[36] which ‘walk’ directionally along actin and tubulin filaments respectively. They move due to a cycle of ATP binding, hydrolysis and release of ADP + P_i that induces conformational changes, which change the affinity of the foot for the filament. The cycles of association and dissociation from the filament bias their movement due to Brownian motion in a ratcheted fashion. In the case of kinesin (Figure 1.3) the ‘feet’ work cooperatively since both feet must be associated with the tubulin filament to catalyse the ATP hydrolysis step. The net directional movement of the walker arises due to the polarity of the filament meaning that the free foot always prefers to reassociate ‘ahead’ of the bound foot. The diastereomeric nature of the interaction between the filament and the feet of the walker combined with the tension of the stem region of the protein assembly mean that there is a lower barrier to movement of one foot past the other in one helical sense than the other such that the motor operates in a cyclical fashion[38].

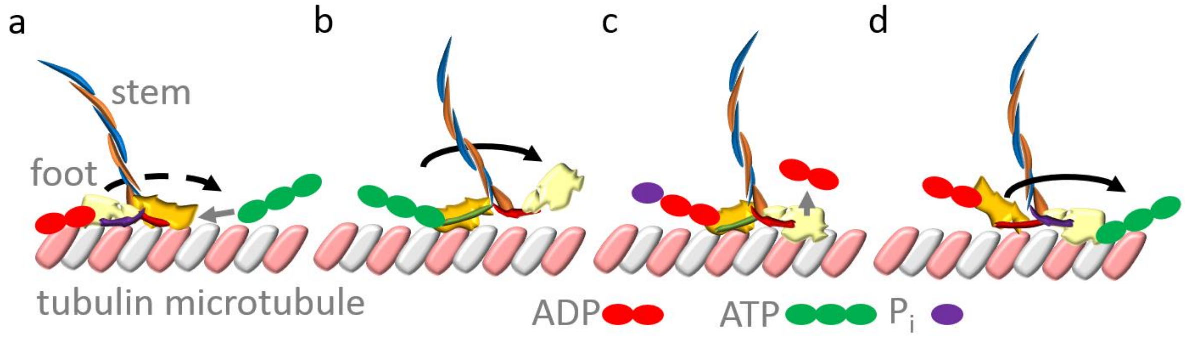

Figure 1.3 Cycle of ATP-driven movement of a kinesin walker on a microtubule[38]. **a** ATP binding anchors the front foot to the filament **b T**he rear foot then dissociates and reassociates ahead of the strongly bound foot **c** and ADP dissociates inducing a conformational change that causes hydrolysis of ATP and dissociation of P_i at the rear foot which then **d** undergoes the same cycle of dissociation as the first foot.

Interestingly the actions of myosin V and kinesin have also been shown to have a synergistic effect on each other's operation. Each motor moves along its track with a characteristic step length, however with the two motors coupled the overall step length for one cycle of operation is increased[39].

D. Rotary motor enzymes

An additional means of overcoming the constant entropic buffeting at the molecular scale is the anchoring of motor proteins within the two-dimensional constraints of a lipid membrane. A classic example of this, and one of the most studied classes of natural molecular machines are the ATP (synth)ase rotary motors[22] (Figure 1.4). These molecular machines comprise two closely associated component motors. A hydrophobic F_0 motor resides in the membrane, while a hydrophilic F_1 motor[40] is mechanically engaged with the F_0 motor but resides in the cytosol. The two motors are held in close association by the a,b,δ subunit of the stator[41]. The structures of each motor are now well-elucidated, and structures at ever finer resolution are consistently being published[42,43]. In addition, experiments that dissect the mechanisms of operation of these motor proteins continue to emerge[44,45,40]. The F_1 motor is composed of 6 alternating α and β domains which together have three-fold symmetry and are arranged around a central γ/ε -subunit spindle. It can usefully be thought of as analogous to a macroscopic three stroke rotary motor[46]. The F_0 motor is composed of 10-15 identical subunits arranged symmetrically in a ring (c-ring) around the spindle. The assembled complex operates in two reciprocal modes. The ATP synthase mode catalyses the formation

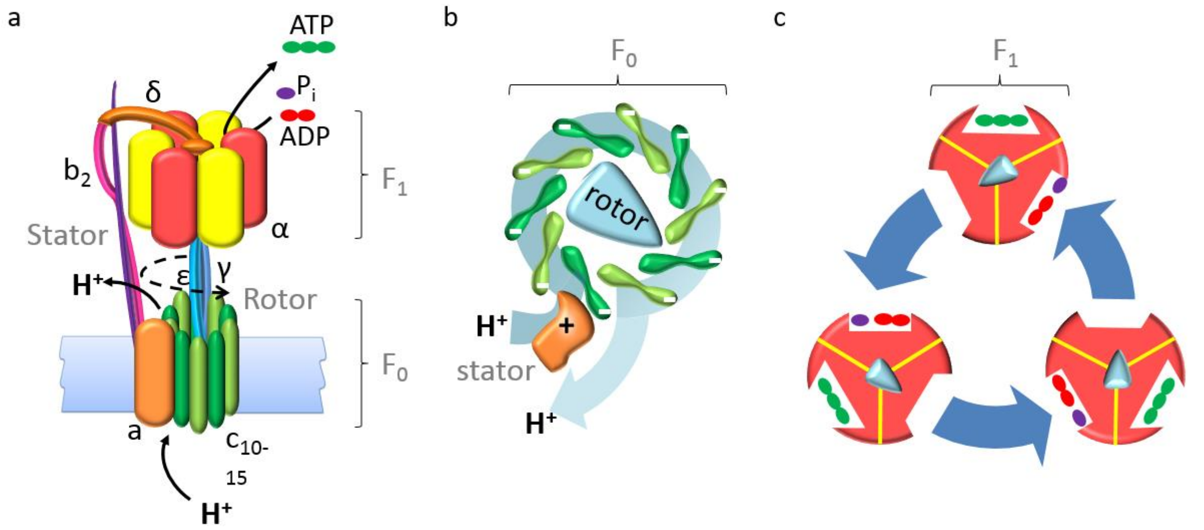

Figure 1.4 Archetypal ATP synthase[22] **a** Cartoon of the complete transmembrane assembly. **b** View down the central axis of the F0 motor domain in ATP synthase mode, influx of H^+ to the F_0 complex on the trans side of the bilayer leads to ratcheting of the c-ring in one direction by sequential electrostatic biasing of thermal fluctuations, these in turn rotate the spindle which drives the conformational changes in the F_1 domain that catalyse the production of ATP from ADP and P_i. **c** Cycle of conformational changes in ATPase and membrane potential-generating mode. ATP binding-hydrolysis-release occurs in a cooperative sequential manner at each of the active sites in turn with a corresponding conformational change that drives the rotation of the c-ring and hence affords ratcheted pumping of cations across the membrane.

of ATP from ADP and P_i at the active sites of the F_1 motor by coupling unidirectional rotation (driven by cation-motive force through the F_0 motor) to a cycle of conformational changes in the F_1 motor. Conversely, the reverse mechanism generates a transmembrane cation gradient by coupling sequential ATP-driven conformational changes to unidirectional rotation of the spindle and c-ring. The rotary ATP (synth)ase is a transmembrane rotaxane where the F_1 motor domain is the macrocycle and the F_0 c-ring and spindle are the thread. This topological relationship underpins another very impressive class of natural transmembrane molecular machines - bacterial flagella. These transmembrane rotaxanated architectures share certain features and operate in a similar way to ATP synthase; they are highly symmetrical about the z-axis and they convert a transmembrane cation-motive force into unidirectional rotary motion of the rotor relative to the stator. This occurs *via* a ratcheted mechanism that biases Brownian motion[47], and is responsible for bacterial motility[48]. Cryo-electron tomography studies of the flagella assembly combined with analysis of the protein sequences by Zhao et al[49] showed the evolutionarily conserved morphology of flagellar motors spanning a number of different species such as *Eschericia coli* and *Borrelia burgdorferi*.

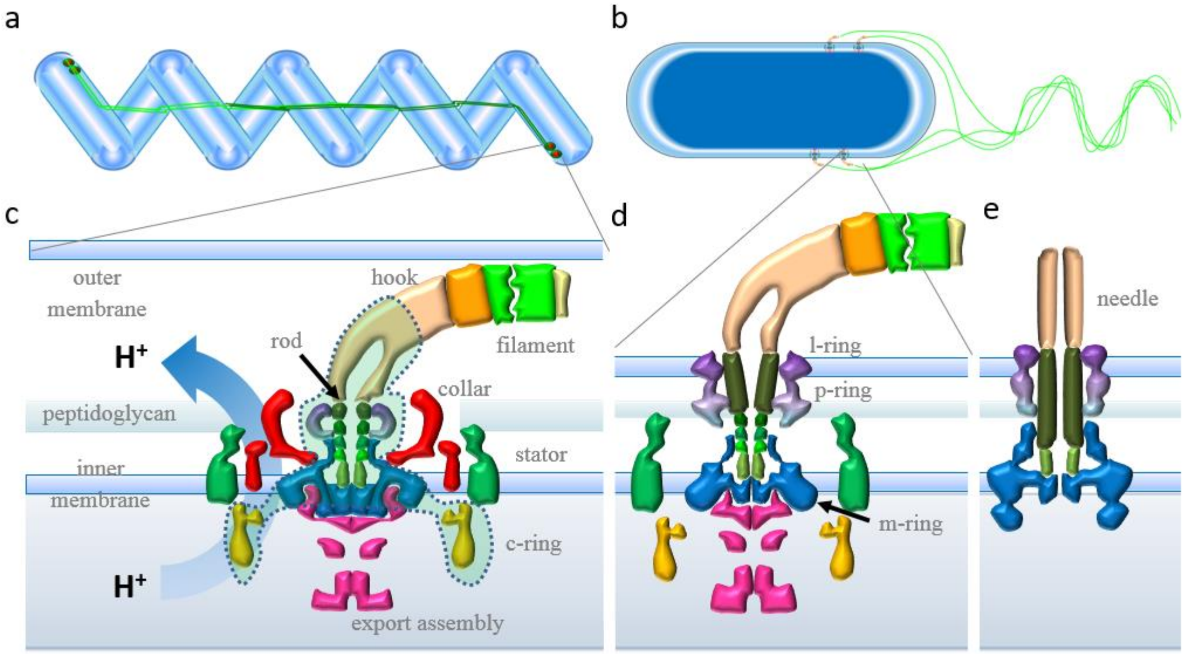

Figure 1.5 External and periplasmic bacterial flagellae[49] and type III injectisome[21]. **a** Helical cellular morphology of *B.burgdorferi* with periplasmic filament. **b** Oblate spheroid cellular morphology of *E.coli* with external filament. **c** Cross-section of *B. burgdorferi* individual motor complex, note the red collar which serves as an extension of the stator anchoring the complex to the peptidoglycan envelope for stability *in lieu* of the outer membrane. Protons exit the cell through the c-ring, transiently changing the electrostatic interaction between the c-ring and the stator, generating a torque in an analogous fashion to ATP synthase, which causes the rotation of all the components aside from the stator and collar. **d** Cross-section of *E.coli* individual motor complex. Components are isochromic with their functional homologs in *B. burgdorferi.* The last ring of the rod (dark green) is extended to span the extended l-ring and p-ring, which anchor the complex to the outer membrane. **e** Cross-section of the type III injectisome showing the evolutionarily conserved homologous structure with the flagellar assemblies.

In both cases the stator is anchored to the inner membrane of the bacterial cell, the rotor includes an L-shaped protein ‘hook’ and an extended whip-like filament structure made of a protein called flagellin. The flagellin filament is assembled from monomers extruded through the conserved central channel, which self-assemble in a highly symmetrical manner[50]. Although the flagellae in *E.coli* and *B. burgdorferi* are very similar in composition and identical in their principal of operation, these organisms have very different cellular morphologies. In *E.coli*, the hook and filament reside outside the cell (Figure 1.5b) and adopt a helical conformation behind the cell due to the rotation of the thread, converting a torque into a linear thrust. However, in *B.burgdorferi* and other spirochetes (Figure 1.5a) the periplasmic space is extended such that the hook and filament reside within it and transfer the force exerted by the rotational torque to the outer cell membrane (Figure 1.5c). This results in a net directional movement of the whole cell due to the helical morphology of the cell. Interestingly, there is a surprising degree of structural homology between flagellae and the bacterial type III injectisome, which transfers proteins into host cells during bacterial infection (Figure 1.5e)[21].

E. Reciprocating transmembrane antiporters

Among the most important natural molecular machines are the transmembrane pumps that maintain the homeostatic balance of analytes within cells. There are a number of distinct types of such pumps and they have been extensively reviewed[51]. An illustrative example of one such pump has recently had its mechanism of action elucidated by Lee and coworkers[52] (Figure 1.6), who obtained the crystal structure of the active conformation of the Na^+ /H^+ antiporter NapA isolated from *Thermus thermophilus*. The antiporter transports protons in one direction at the same time as transporting a sodium ion in the opposite direction across a membrane. The functional assembly is a protein homodimer with each half comprising two subunits, a core responsible for the binding to H^+/Na^+ and a subunit responsible for dimerisation. The core contains an aspartate residue D157 at the interface between the subunits, which binds the Na^+ and H^+ ions in a negatively charged cavity at different points in the cycle of operation. The assembly will cycle through the two conformational states as long as the pH is low enough on one side of the membrane to protonate the D157 residue. This example showcases one mechanism by which natural transmembrane molecular machines, and by extrapolation synthetic ones, can function - the exploitation of a transmembrane gradient.

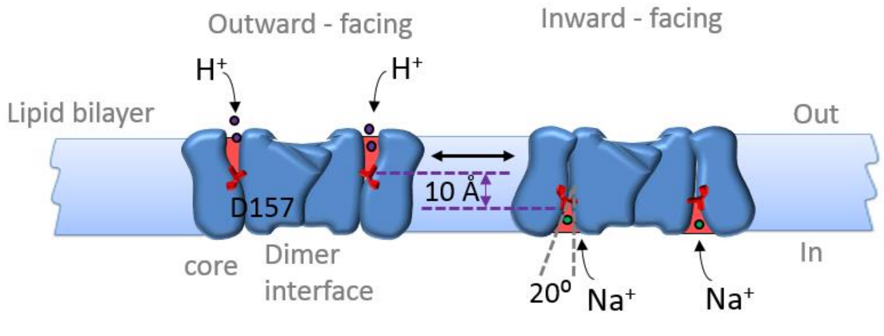

Figure 1.6 Schematic representation of the Na^+/H^+ antiport mechanism in NapA[52]. At pH < 6.8 core residue D157 will bind H^+ eliciting a conformational change – the core domain rocks by about 20° with respect to its initial alignment, D157 reorientates by about 10 Å to point towards the opposite face of the membrane. A Na^+ ion can now displace the H^+ from D157 and the assembly returns to its original state where the high concentration of H^+ favours the dissociation of Na^+ with the conformational change once again allowing the binding of H^+.

1.2 The development of synthetic molecular machines

Natural molecular machines assemble by exploiting the principles of molecular self-assembly, and thereby provide lessons for the construction of synthetic molecular machines that imitate the functions of their natural counterparts[1]. Many of the earliest synthetic supramolecular systems with elementary machine-like properties are more accurately described as switches[53]. Leigh et al have thoroughly discussed the distinctions between switches, shuttles and true molecular machines and their underlying principles of operation[53]. Briefly, molecular shuttles flip between two states under thermodynamic control as a result of Brownian motion. The result is a time-averaged Boltzmann distribution between the two states at equilibrium in the bulk, with the position of the equilibrium and hence the meta-state of the population of shuttles in the bulk being governed by the relative free energies of the two states. In contrast, a molecular machine transforms chemical potential or electromagnetic energy to cycle through different conformational states giving rise to coordinated directional mechanical motion which can be used to perform work.

A. Nanomechanical rotaxane shuttles

The first synthetic mechanical shuttles were based around interlocked molecules known as rotaxanes. The rotaxane depicted in Figure 1.7 contains a green station that is slightly bulkier than the red station, while changing the pH changes the protonation state of both the macrocycle and the red station. This change in protonation state changes the relative depths of the potential wells associated with the residence of the macrocycle at each station (Figure 1.7b). At neutral pH only the red station is protonated and the macrocycle has equal affinity for each station, and at low pH both the macrocycle and the red station are protonated and the macrocycle associates preferentially with the green station. Conversely, at high pH none of the moieties are protonated and the macrocycle associates preferentially with the red station. At a given pH under equilibrium conditions, the distribution remains constant in the bulk even though on the single-molecule level there is rapid exchange between the red and the green stations. Such systems, which include most of the synthetic molecular elevators, shuttles and muscles reported to date, do not constitute true molecular machines or even motors as they do not operate in a cyclic fashion to do mechanical work by consuming fuel in the form of chemical bonds or chemical potentials.

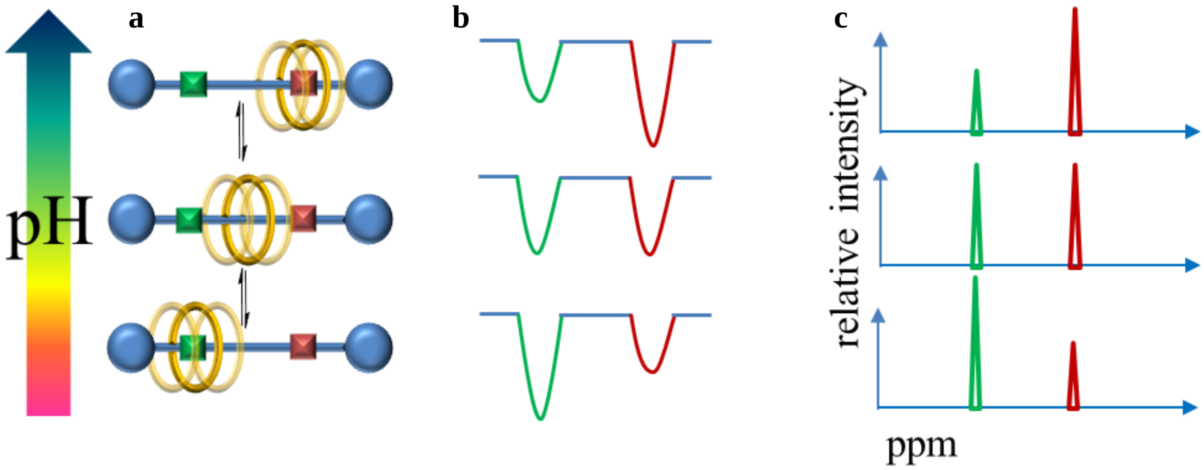

Figure 1.7 Relationship between the position of mechanical equilibrium and potential energy in a population of two-state molecular assemblies. **a** Hypothetical rotaxane bearing two ‘stations’ green and red. **b** The relative depths of potential wells corresponding to association of the macrocycle at each station at varying pH. **c** Cartoon of the NMR distributions of macrocycle locations for the population at varying pH.

A so called synthetic molecular machine recently created by Lewandowski et al[54] mimics the function of the ribosome to a limited degree. The system shown in Figure 1.8 is based on a rotaxane, with a linear ‘track’ molecule threaded through a macrocyclic host molecule. The assembled system undergoes a cascade of cyclisations and rearrangements in which the peptidyl moieties bound to the thread are successively transferred to the tip of the pendant peptide chain on the macrocycle by a series of nucleophilic substitution reactions. The macrocycle dethreads from the track component after the final peptidyl group is transferred, and the resulting peptide product is then cleaved from the macrocycle. As the authors point out, S-N acyl transfer is a key feature of non-ribosomal peptide synthesis and thus, the system more closely resembles this process than that of the ribosomal peptide synthesis as outlined earlier in Section 1.1B. Although the molecular assembly performs its synthesis in a seemingly repetitious manner, the system’s machine-like properties are fairly limited. Unlike ribosomal peptide synthesis, the underlying mechano-chemistry of the internal cycles are rather different to each other. Thus, overall the system undergoes what is perhaps better described as a staggered structural isomerisation or a linear degradation composed of homologous but chemically distinct transition states to a thermodynamically inevitable minimum final energy state. Compared with enzymes, this system has severe limitations; it does not perform multiple cycles (turnover number less than one) and requires much harsher conditions to operate.

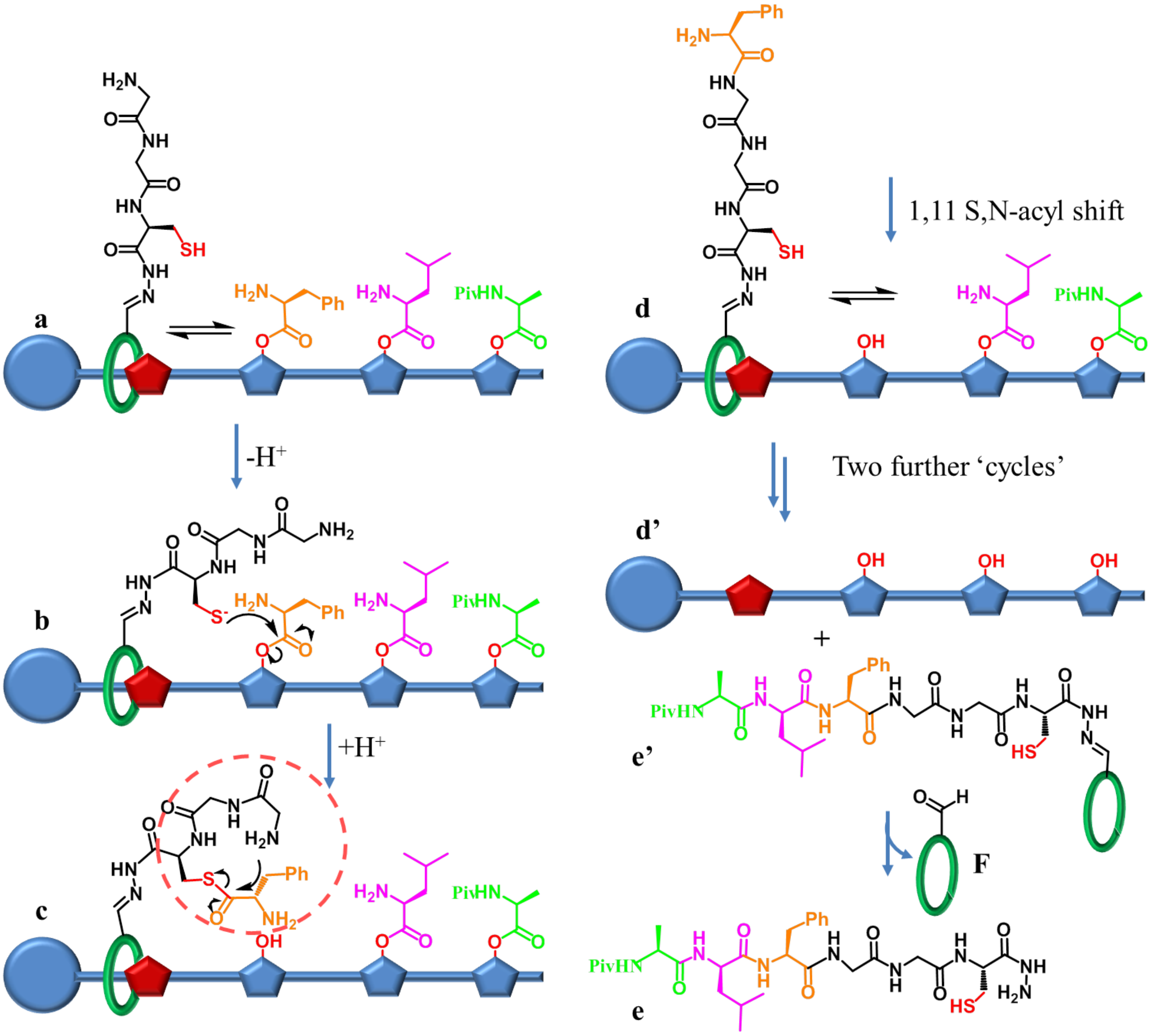

Figure 1.8 Operation of the peptide synthesising molecular "machine" developed by Lewandowski et al[54]. **a** The macrocycle shuttles back and forth at random between the stoppered end of the track and the site of the first pendant peptidyl group (orange). The macrocycle bears a peptide chain the first residue of which is a trityl protected (not shown) cysteine (red). **b** After deprotection the thiolate group of the cysteine residue is free to undergo transacylation with the amino acid phenolic ester of the first peptidyl blocking group, removing it from the track. **c** This then undergoes a further reaction with the terminal amine of the peptide chain on the macrocycle, resulting in **d**, the extension of the terminal end of the peptide chain and the regeneration of the thiolate group ready for reaction with the next blocking amino acid phenolic ester on the track. **d'** this cycle is repeated until the final blocking amino acid phenolic ester is liberated from the track and the macrocycle is free to dissociate from the track giving **e'** at which point it is cleaved to yield the complete oligopeptide **e** and the macrocycle **f**.

The system also requires a great deal of work to create in the first place and is then used only once. On the other hand, the ribosome constructs itself, has a high turnover number, and responds to the presence of an external fuel, catalytically producing varied and long polymers by cycles of operation with identically sized transition states – it is a true machine. The synthetic and natural system also differ at a topological level, since the components of natural peptide synthesis are only transiently associated with each other allowing it to perform cycles of association → synthesis → disassociation. Whereas, the synthetic system has no way of regenerating either its mechanically interlocked assembly or the covalently modified thread of its initial condition after operation. In light of this group's other work a system can be envisioned by extrapolation that would be able to accomplish catalytic repeated syntheses undergoing a chemically cyclic process using a catenated circular track, rather than a linear rotaxanated system. Clearly, there are huge challenges remaining to be overcome on this branch of the evolution of synthetic molecular machines.

B. Synthetic rotary motors

In contrast to switches, rotary motors operate by cycling through a number of distinct states in response to energetic stimulation or the availability of a suitable fuel [55]. If only two states are available to the system then the process by which the system goes from A→B must depend on a different stimulus or fuel than the process through which the system goes from B→A and, in other words, these processes must not simply be the reverse of each other (as they are in a switch). In the case of a system with three or more states, interconversion between the states is only possible in the order A→B→C→A. Conversions from A→C, C→B or B→A are disallowed, either due to asymmetry in kinetic barrier heights between states, large differences in the timescale of the conversion in each direction or the conversion having no physical basis. In one example of this type of behaviour in a synthetic system, a catenated system comprising two macrocycles threaded on a third in which the smaller macrocycles undergo cycles of circumrotation around the third in a stepwise manner in response to structural isomerisations induced by cycles of UV irradiation and chemical potential[56].

Another type of system that exhibits cyclical behaviour is a class of small molecular rotary motors created by Feringa[57]. These systems, such as the recently reported example shown in Figure 1.9[3], operate by repeated cycles of photoirradiated *cis/trans* isomerization of the central double bond and subsequent helicity inversion by thermal relaxation to convert between their accessible states A→B→C→D→A. The unidirectional rotation can be explained by referring to the potential energy surface shown in Figure 1.9b, which shows the barrier heights and the well depths associated with each state. Under constant irradiation each molecule is driven through the available states and hence exhibits unidirectional motion.

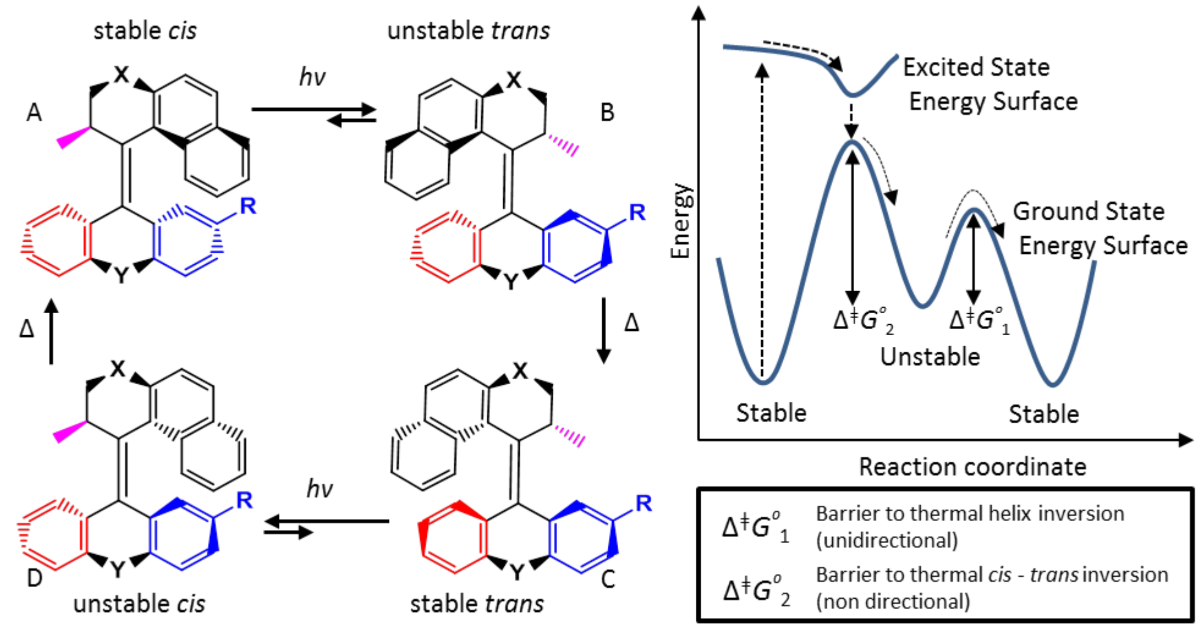

Figure 1.9 Light-driven unidirectional molecular rotors[3]. **a** The operational cycle of photoisomerisation and thermally induced helicity inversion of a synthetic molecular rotary motor. Motors are photoexcited by irradiation at 355 nm which converts the central double bond the stable *cis* conformer **A** to the unstable *trans* conformer **B**. B then undergoes a favourable helicity inversion due to thermal interaction with the bath to give the stable *trans* conformer **C**. C is then photoexcited once more to give the unstable *cis* conformer **D** which again undergoes thermal helicity inversion returning the system to the initial conformational state **A**. At any given time during operation the relative occupations of the four states will remain constant, though each molecule cycles through the conformations independently of the others. The potential energy surface corresponding to the interconversion of conformational states available to the motor **E** shows the asymmetry between the barrier heights to helicity inversion and *cis*/*trans* isomerisation due to thermal relaxation from the photoexcited states. This results in net unidirectional rotation as the favoured relaxation pathway is always the helicity inversion, which owing to the diastereomeric nature of the conformers, is unidirectional. **b** Potential energy surface for the operation of the molecular motor

Retrograde motion does not occur because of the lower barrier height for helix inversion (which is unidirectional due to the diastereomeric character of the molecule) with respect to reisomerisation from the unstable state. While this is a clever system that achieves unidirectional rotation at MHz frequency, it is not inherently capable of doing mechanical work under Brownian conditions. This is because the ensemble average of the torques generated by each motor cancel out when summed over all the randomly tumbling motors in solution.

C. Collective properties emerge from molecular motor arrays on surfaces

Key to the extraction of work from some classes of molecular machines is the attachment of molecules to surfaces. This restricts the degrees of freedom available to the system thereby allowing the effects of thermal motion to be overcome, allowing transduction of molecular motions into net directional motion. *Anabaena* sensory rhodopsin (ASR) provides an example from nature where anchoring of molecular machines to a surface allows work to be performed (Figure 1.10). Theoretical work by Strambi et al[58] on the mechanism of *Anabaena* sensory rhodopsin operation chimes with the cyclic operation of the Feringa rotary motor described above (Figure 1.9). Since the rhodopsin is engaged at a membrane surface and the rotation is coupled to an electron-transfer process, this means that work is done by the system and it can therefore be classified as a true molecular machine.

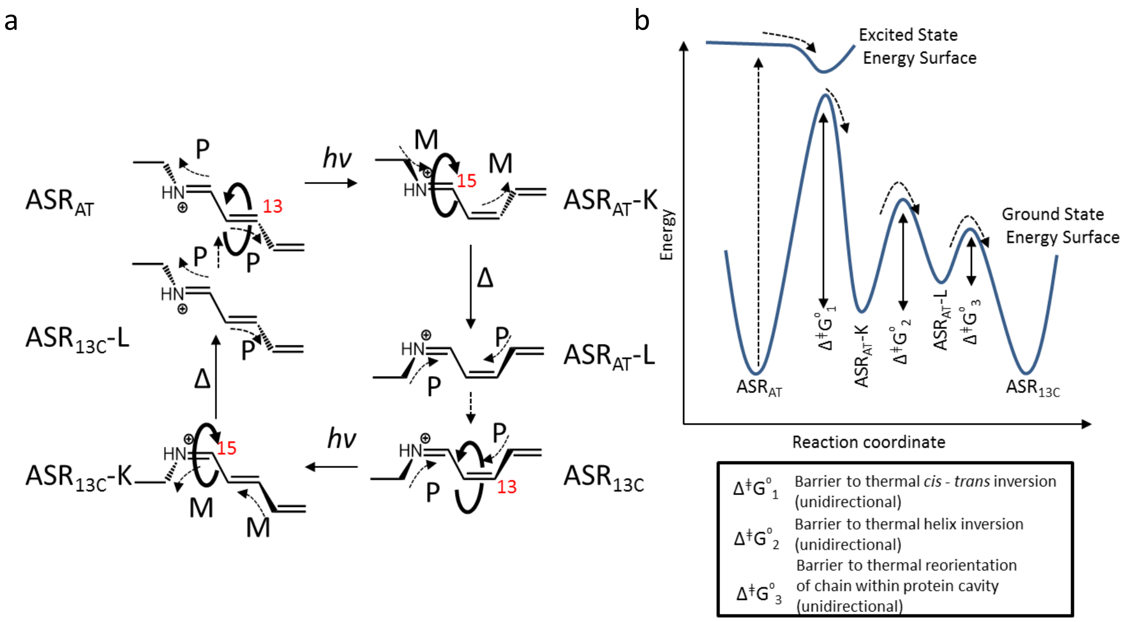

Figure 1.10 The photochromic moiety of *Anabaena* Sensory Rhodopsin (ASR)[58]. **a** The putative conformational rearrangements made by the photochromic chain which is thought to undergo a cycle of conformational changes elicited by exposure to light. First the double bond at 13 in ASR$_{AT}$ photoisomerises from *trans* to *cis* giving ASR$_{AT}$-K where –K indicates the orientation of the chain with respect to the surrounding protein barrel. Steric constraints imposed by the chirality of the protein barrel induce a thermally activated second unidirectional *trans–cis* isomerisation of the double bond at 15 giving ASR$_{AT}$-L. This is an unfavourable orientation for the chain with respect to protein and thus it undergoes a thermally activated unidirectional bodily rotation within the protein barrel completing the half cycle of operation to give ASR$_{13c}$ before a second photon inititates the second half cycle. **b** Proposed potential energy surface of the operation of ASR.

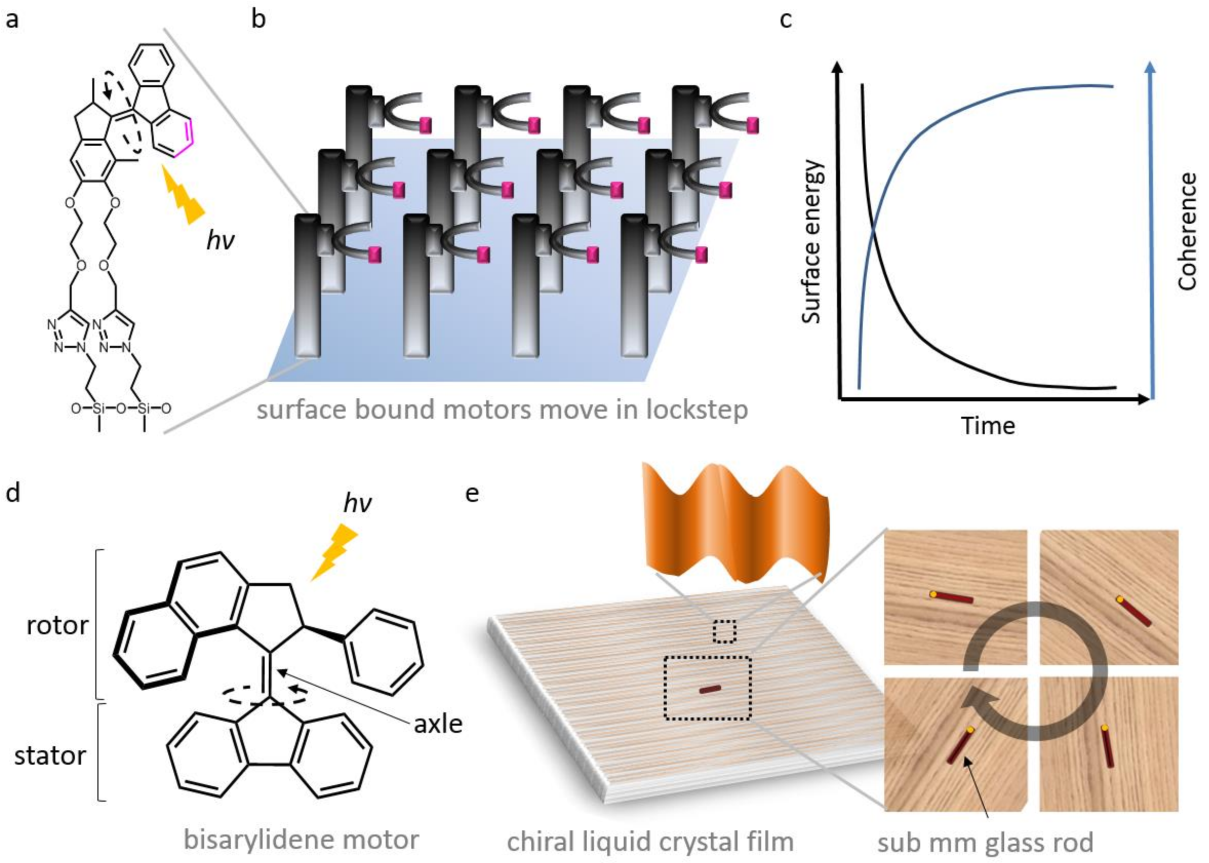

Figure 1.11 Bisarylidene molecular motors arrayed on a surface operate in an increasingly synchronised fashion because of the interactions between neighbouring motors[5]. **a** Structure of an individual motor. **b** Motors arrayed on a surface. There is a greater mutual effect at higher surface coverage. This can be rationalised by considering the depth of the potential well concomitant with the modes of molecular motion available to the system, which is greatest for collective modes in which interactions are minimized and thereby possess a greater degree of order. Thus, Synchronised motion will develop over time in a population of strongly coupled motors to minimise the potential energy associated with the functionalised surface. **c** The potential energy of the surface decreases as the degree of synchronicity between the motors increases over time. This premise was exploited in a related study[59] where a bisarylidene molecular rotor **d** was used as a dopant in a chiral liquid crystal film **e**. Upon photoirradiation the unidirectional rotation of the bisarylidene was dissipated more efficiently in one sense than the other due to diastereomeric interactions between the rotor and the liquid crystal and thus macroscopic surface waves were generated which drove the unidirectional rotation of a sub mm glass rod **f**.

Similarly, attachment of Feringa’s synthetic rotary motor molecules shown in Figure 1.11a to a quartz surface also allows collective modes of molecular motion to emerge (Figure 1.11b)[5]. The behaviour of surface-bound rotors at high coverage density varied from that in solution, which they suggest to be due to intermolecular interactions between the rotors. This affords the potential for extracting work from the operation of the motors on the surface, which cannot be accomplished with the very closely related system in solution. In a surface-bound environment, for a population of closely packed molecular motors rotating unidirectionally due to photoexcitation, the degrees of freedom available to the population are reduced by attachment to the surface and by steric interactions with nearest neighbours. This means that available modes of molecular motion will propagate over the surface to reduce interactions with nearest neighbours thereby increasing the efficiency of energy dissipation and giving an increasing degree of coherence of action between the individual moieties over time (figure 1.11c). This is also seen in natural systems such as in the generation of metachronal waves by populations of beating cilia[60]. In a related study Feringa et al used the motors shown in figure 1.11d as dopants in a chiral liquid crystal film (Figure 1.1e) to cause rotation of microscale objects (Figure 1.11f)[59].

Rotaxanated[61] systems have been used to perform macroscopic work using a surface functionalised with rotaxanated small molecules[6]. Although the individual rotaxanes are molecular shuttles and thus cannot be classified as true machines, when arrayed on a surface they exhibit collective properties that can be exploited to do mechanical work. In the system shown in Figure 1.12 a rotaxanated architecture is arrayed on a surface in a self-assembled monolayer. Each rotaxane is composed of a thread bearing two stations; a tetrafluorosuccinimide moiety (orange), a photoisomerisable fumaramide moiety (green) and a macrocycle (turquoise) which under ambient conditions shuttles between the two stations at random due to Brownian motion. Irradiation of the surface at 240 – 400 nm photoisomerises the *E* alkene of the fumaramide to a *Z* form giving a maleimide, which has a lower affinity for the macrocycle. Constant irradiation drives the equilibrium of *E*/*Z* isomers in favour of the *Z* isomer increasing the time spent by each macrocycle masking the orange station. Because the shuttles are bound to a surface in close proximity, the collective biased Brownian motion of the shuttles induced by photoirradiation gives rise to a region of altered wettability. Thus, photoirradiation increases the polarophilicity with respect to the unilluminated surface. The collective conformational changes of the rotaxanated molecules ahead of a drop of diiodomethane made it possible to transport the drop ~ 2 mm up a surface inclined at 12°. Stoddart et al used redox active rotaxanes anchored to a gold surface to transduce macroscopic deflection of a cantilever in response to cycles of reduction and oxidation[62].

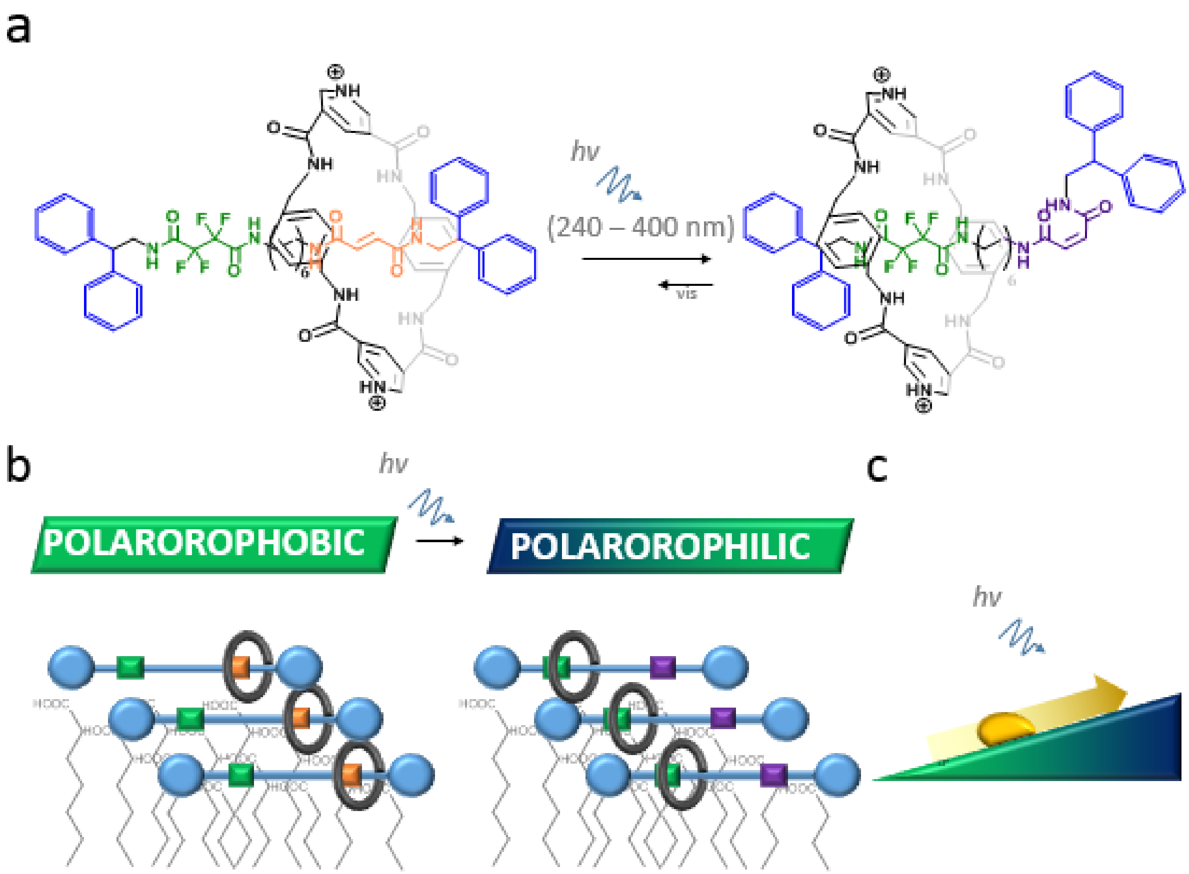

Figure 1.12 A functional 'smart' surface[6]. **a** Structure of the macrocycle and thread components of the rotaxane under visible light and UV irradiation. **b** Bare surface functionalised with a self-assembled monolayer of rotaxanes and its response to UV irradiation. **c** Constant irradiation is used to drive the equilibrium in one direction, inducing macroscopic work by altering the contact angle of the surface ahead of a drop of iodomethane on the surface, thus inducing it to move against gravity by capillary action.

D. DNA-based synthetic molecular machines

Nature's complex molecular machines certainly exceed our own in terms of elegance, modularity and functional efficacy. Bionanotechnological research seeks to exploit the principles of molecular recognition to repurpose biomolecules such as DNA and proteins as machine elements. This is a maturing field and has been well reviewed[13]. Many of the achievements of wholly synthetic molecular machines: switches[63], walkers[55], [64], and even molecular synthesisers[14] have also, sometimes years previously, been accomplished by synthetic molecular machines based on DNA. Such DNA nanomachines exploit the programmable interactions of canonical base pairing[65] and the well-known dimensional

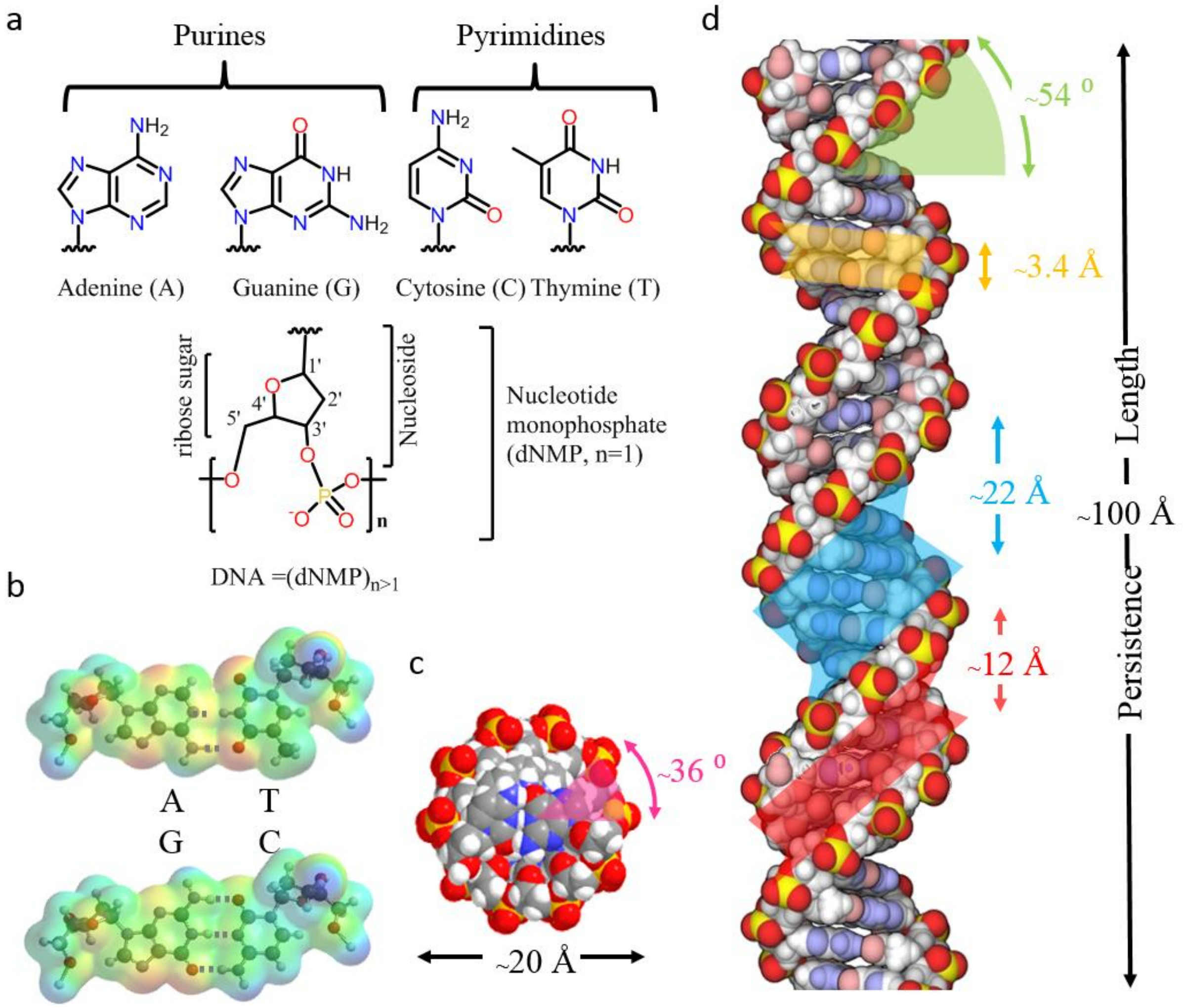

Figure 1.13 Schematic representation of the canonical base pairing and dimensions of B-DNA. **a**. the four nucleobases adenine and guanine (purines), cytosine and thymine (pyrimidines) are linked together in linear polymers by phosphate ester linkages between deoxyribose sugar units. **b.** H-bonded base-pairing interactions arranges the strands anti-parallel to one another i.e. 5’→3’ with 3’→5’ giving rise to the right-handed double helix of B-DNA. **c**. Space-filling model showing the axial view down a B-DNA double helix **d** Lateral view showing the approximate dimensions of the DNA double helix indicated by the shaded areas: minor groove (red), major groove (blue), inter-base pair distance (yellow), helical pitch (green) and degrees per base (violet).

parameters of double stranded DNA (Figure 1.13). One of the most impressive examples of the possibilities afforded by using DNA to build molecular machines is a walker-mediated synthesiser from He et al[14] (Figure 1.14). This machine operates in a similar, stepwise fashion to the naturally occurring ribosome[33] and to the synthetic peptide synthesiser made by Lewandowski et al[54] (Figure 1.8). The track (**T**) and monomer bearing DNAs **S1, S2, S3** are combined in solution and self-assemble. Walker **W** and initiator **SO** are combined separately and then added to the assembled track to give **a**. **D1’** can now hybridise to **D1** which brings the free amine on **W** and the succinyl ester of **S1**

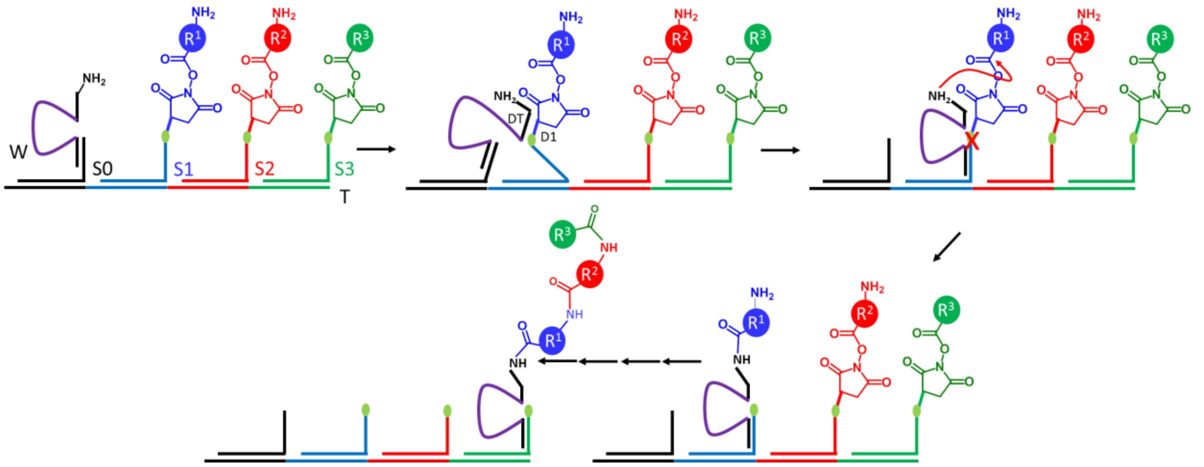

Figure 1.14 A DNA walker-mediated peptide synthesiser[14].

into close enough proximity that they undergo an acylation reaction. At the same time, **D2'** migrates from **D2 SO** to **D2 S1** (to the next monomer) by strand displacement to reduce strain in the system. The DNAzyme region (purple) can now catalytically cleave the RNA linker sequence (green dot). Although **W** has moved in space the system is restored to the initial position in the operational cycle of base pair association. The system continues to operate in almost identical fashion for the remaining two steps. It compares favourably to the synthetic rotaxanated peptide synthesiser in many ways: it is easier to construct (standard DNA synthesis followed by self-assembly), and operates under milder isothermal conditions and most importantly exhibits turnover; the melting temperatures of the various duplexes being low enough to allow the exchange of spent and unreacted S groups. However, it suffers from the same mechanical limitations as reference[54] - effective molarity of the amine and succinimidyl-ester reactive sites decreases with each amino-acid addition step, limiting the machine-like behaviour of the system. Furthermore, the increased flexibility of longer chains would potentially allow monomers to be added in an unintended order as in the case of reference[54].

1.3 Compartmentalised systems & transmembrane channels

One key feature of the mechanisms of some natural molecular machines is the exploitation of localised or partitioned environments that have different properties to bulk solution. Biopolymers and charged species have limited permeability through lipid membranes (Figure 1.15). Thus, the incorporation of molecular machines into membranes allows transmembrane

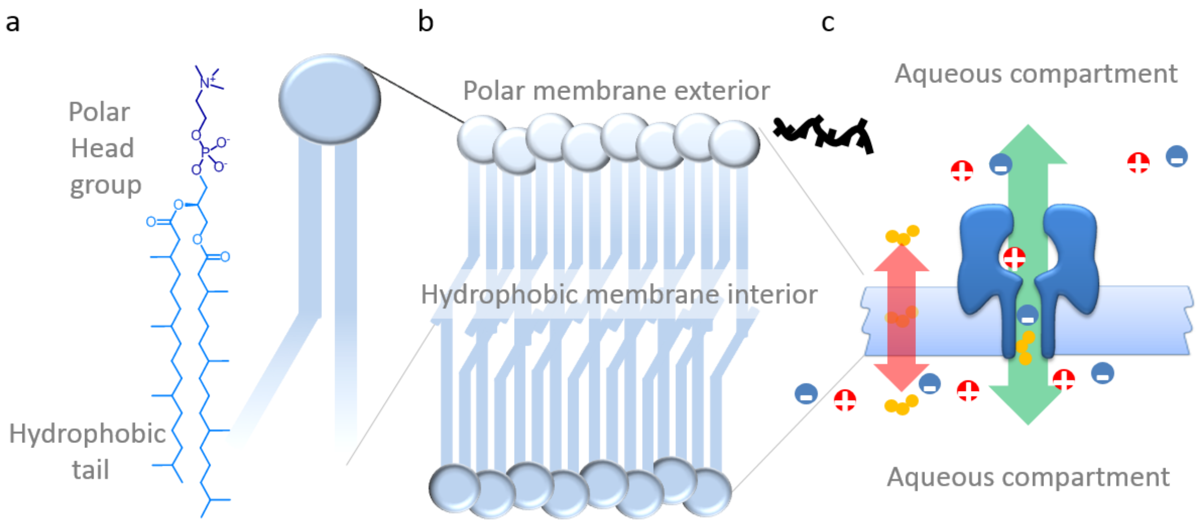

Figure 1.15 Membrane architecture. **a** A single phospholipid molecule comprises a polar amino phosphoglycol head group and a hydrophobic bifurcated hydrocarbon tail. **b** In aqueous solution the hydrophobic effect causes the phospholipids to self-assemble as bilayers with hydrophobic interiors which separates aqueous compartments. **c** The bilayer is almost impermeable to ions, small organic molecules can diffuse across slowly depending on their lipophilicity, while biopolymers are prevented from crossing the bilayer (red double arrow). However, when a channel protein is inserted in the membrane the activation barrier to the transmembrane transport of otherwise excluded solutes is greatly reduced (green double arrow).

chemical or electrical (ionic) potential gradients either to be established, or to be utilised in their work cycles. Indeed nature is replete with membrane associated molecular machines[66]. Cellular homeostasis is maintained by membrane-integrated proteins that couple conformational changes to the transmembrane transport of specific chemical species[67] either passively along or actively against concentration gradients. Similarly, in the case of F_1F_0 ATP (synth)ase, transport of cations across a bilayer is coupled to conformational change and the reversible synthesis/hydrolysis of ATP. Indeed, in the case of the flagellar motor, transmembrane translocation of protons is coupled to rotary motion which causes cellular locomotion[21,68]. Similarly, transfer of DNA[37] and proteins[19,69] across membranes is performed by protein machines that undergo NTP-hydrolysis-coupled cycles of conformational change to ratchet these polymers through transmembrane pores.

A. Transmembrane protein pores

Not all transmembrane proteins can be classified as molecular machines, even though they may have important biological roles. For example, many natural transmembrane protein channels undergo “gating” events, in which the channel opens and closes.

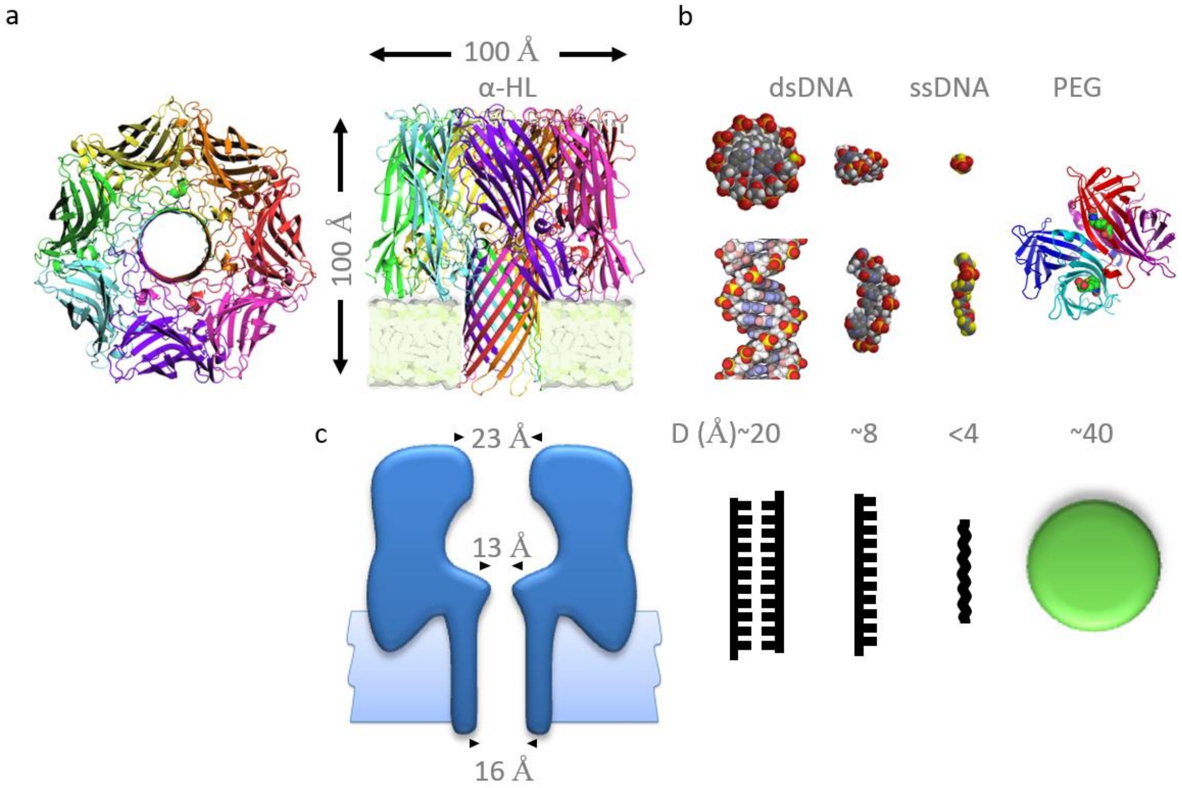

Figure 1.16 α-Haemolysin (α-HL) [71] and other macromolecules of similar dimensions. **a** Crystal structure of α-HL top and side elevations **b** DNA, PEG and streptavidin. **c** Cartoon representations used henceforth in the present work.

Gating may occur stochastically, but is often involved in cellular regulation in response to external stimuli such as mechanical tension[70] or fluctuations in transmembrane potential. These gating events may be due to transient conformational changes in which loosely bound peptide chains encroach the channel, or in some cases due to larger-scale conformational transitions. They do not however involve repeated cycles of coordinated directional movement of one part of the assembly with respect to another that accomplish active transport against a gradient.

α-Haemolysin (α-HL) is an archetypal biological pore-forming protein that is often used as a building block and a source of inspiration in the construction of transmembrane molecular devices[71] (Figure 1.16). α-HL is a toxin produced by *Staphylococcus aureus* that penetrates the lipid membranes of red blood cells causing the cells to leak or even burst (lyse, hence the name, haemolysin), thereby increasing the nutrients available to the bacteria. Owing to its ability to readily form stable and reproducible transmembrane pores it has been used extensively for single-molecule investigations of the biophysics of DNA and proteins[72, 73]. In this capacity, α-HL it is not being used as a molecular machine element per se but as an element for the detection of macromolecules as they are driven through the pore by an electric field (or electro-osmotic flow). The translocation of a particular macromolecule through a transmembrane channel is hindered to a varying degree depending on its steric bulk and interactions with the pore interior. This gives rise to current blockades of magnitude, duration and frequency that are diagnostic of the translocating macromolecule.

B. Membrane-adapted silicon nitride channels

Biological transmembrane nanopores have inspired the development of engineered compartmentalised systems. For example, some of the simplest artificially compartmentalised systems employ switchable, stimuli-responsive molecules that are anchored to the internal surface of small 10^{-6} – 10^{-9} m apertures in thin wafers (made of materials such as silicon nitride) that form a partition between two fluid-filled compartments. Such devices have been made that effect the transport of an analyte[74,75] *via* interactions with both synthetic and biological molecules. Tuneable systems that respond to stimuli such as an applied voltage[76], pH[77,78], temperature[79,80], light[81], or to specific ions[82] and enantiomers[83,84] have also been developed. While such systems are not molecular machines capable of performing work to establish chemical gradients (they are merely gates or switches), they can mimic cellular function by allowing the selective passage of specific analytes. The most sophisticated systems of this type allow the transmembrane movement of macromolecules such as specific proteins and have been studied on a single-channel level[85].

A system developed by Meyer et al[85] mimics the olfactory system of a fly using a silicon nitride wafer that is augmented with two functionally modified layers (Figure 1.17a). The first modification step paints a phospholipid bilayer over the silicon nitride surface and the internal surface of a nanoscale channel that passes through the wafer. This is followed by the addition of molecules comprising an affinity probe head (e.g. biotin) that is bound to a lipid tail that anchors the molecular conjugate within the lipid bilayer coating. These molecules are able to freely diffuse within the plane of the bilayer coating. The affinity probe head binds specifically to the protein of interest facilitating and slowing its movement through the pore allowing detection by monitoring blockages in the ion current flowing through the pore (Figure 1.17b). The system shows an increase in the movement of streptavidin (SA) through the silicon nitride pore, allowing detection at very low concentration (5 pM) compared to other proteins that do not exhibit a strong specific interaction with the modified lipid groups (Figure 1.17c). However, this and other similar

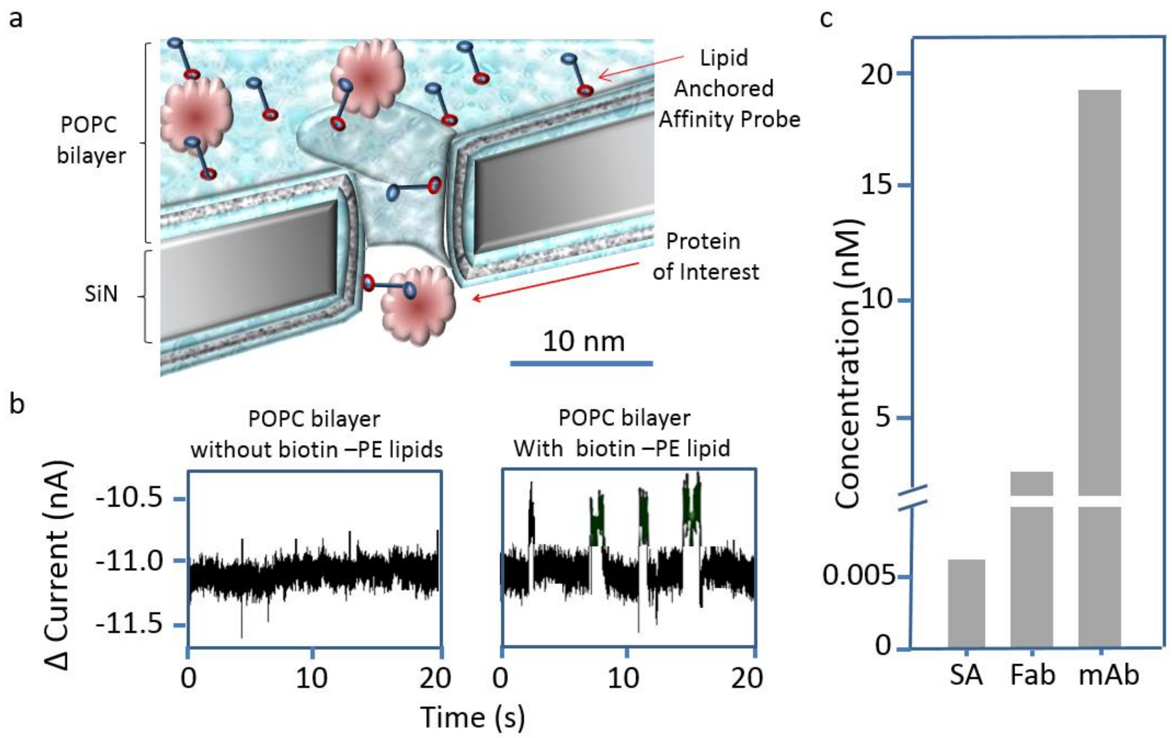

Figure 1.17 Nanopore system designed to mimic the olfactory sense of a fly[85]. **a** Lipid-modified nanopore in a silicon nitride wafer. **b** Ion current traces generated by the spontaneous transmembrane translocation of the target protein. **c** Comparison of the improvement in detection limit afforded by complementarity of the target protein to the modified lipids.

systems only involve spontaneous processes and are not capable of doing mechanical work to actively transport proteins across the membrane. In comparison to natural transmembrane systems one obvious difference of many silicon nitride-based nanopore approaches is the diameter of the channels involved. This is due to the inherent difficulty in reproducibly obtaining nanometre-scale features using top-down engineering techniques. This is important because interactions between an aperture and an analyte become more pronounced when they have similar dimensions. Hence, recent efforts to address this issue of reproducibility have borrowed from biology by creating hybrid systems in which a biological protein pore is embedded within a lipid bilayer contained within an engineered silicon nitride channel[86].

C. Self-assembled synthetic transmembrane nanopores

Other artificial compartmentalised systems dispense entirely with the stability of inorganic partitions such as silicon nitride in favour of lipid bilayers due to the ease of bilayer preparation. Furthermore, the structural precision afforded by well-designed, self-assembling supramolecular structures can result in accurate reproducibility on the molecular level. For example, peptides[87] and other synthetic molecules[88] have been used to form stable artificial nanopores across lipid bilayers[89].

The programmable self-assembly of DNA has been utilised to produce well-defined 3-D structural elements. Langecker et al used DNA origami to design and reproducibly construct biomimetic nanochannels that spontaneously self-assemble in lipid bilayers with dimensions close to those of natural protein channels[90] (Figure 1.18). They also investigated the capacity of these channels to gate in response to external bias by preparing channel variants with differing internal cavities. A variant bearing a strand that could readily adopt a channel-blocking conformation in response to high transmembrane potentials was observed to gate more than the original channel. Given the range of stimuli-responsive and molecular-machine architectures that have been developed using DNA nanostructures, it is easy to envisage that such a strategy might move beyond simple gating (switching) systems to yield true transmembrane molecular machines that are capable of active transmembrane transport.

Another example of an artificial transmembrane channel is provided in the work of Guo[91](Figure 1.19) These researchers modified the connector protein of the phi 29 dsDNA packaging motor to include hydrophilic regions that allowed it to be inserted into planar lipid bilayers.. The natural system includes an ATPase unit similar to the F1 motor of rotary ATP (synth)ase which ratchets dsDNA into the viral capsid against a concentration gradient and packaging it to almost crystalline densities[92]. The mechanism has been hotly debated for years and was recently elucidated by Zhao et al[93] as involving revolution of the dsDNA around the interior wall of the channel but not involving rotation of the DNA about its own axis. The ATPase required for active DNA transport was not incorporated into this artificial membrane adapted system. Nonetheless dsDNA translocation was accomplished by electrophoetically driving the DNA using an applied potential. The loop regions have been shown to be essential for maintaining the one-way transport of the DNA[93] acting in a similar way to the teeth on a cable-tie.

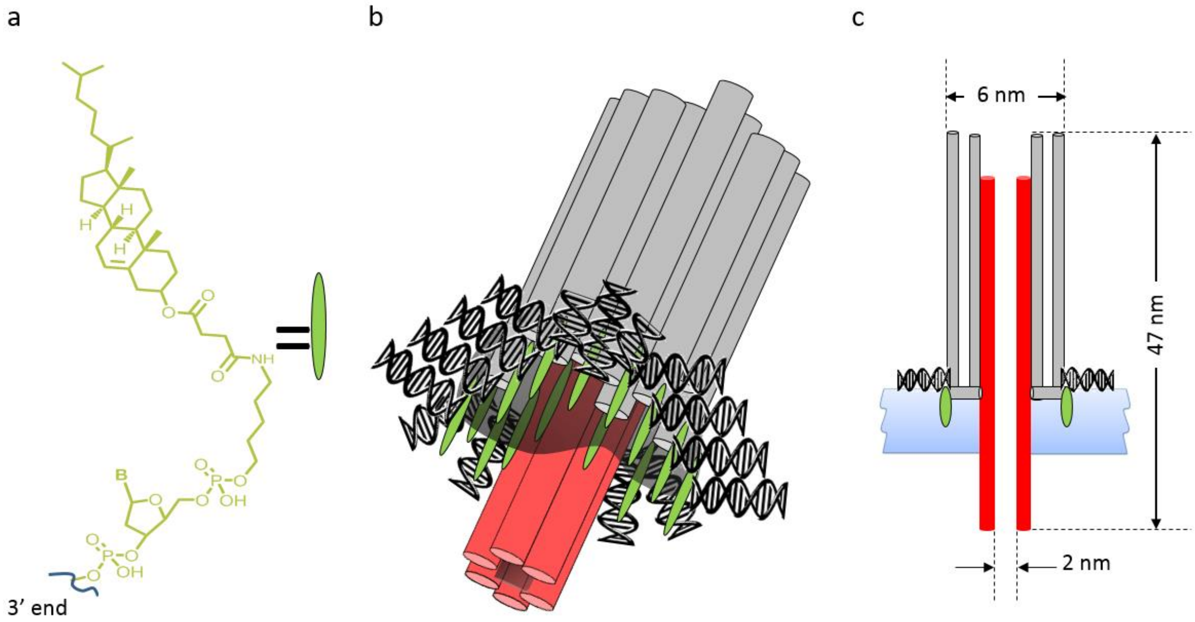

Figure 1.18 An artificial nanopore made using DNA origami[90]. **a** Structure of the cholesterol-modified DNA membrane anchor. **b** The assembled nanopore, the red and grey cylinders represent DNA helix bundles. The cholesterol-modified DNA (black helices with green ellipses) is synthesised with specific sequences such that it self-assembles to give the three-dimensional pore. **c** Orientation of the channel with respect to a lipid bilayer.

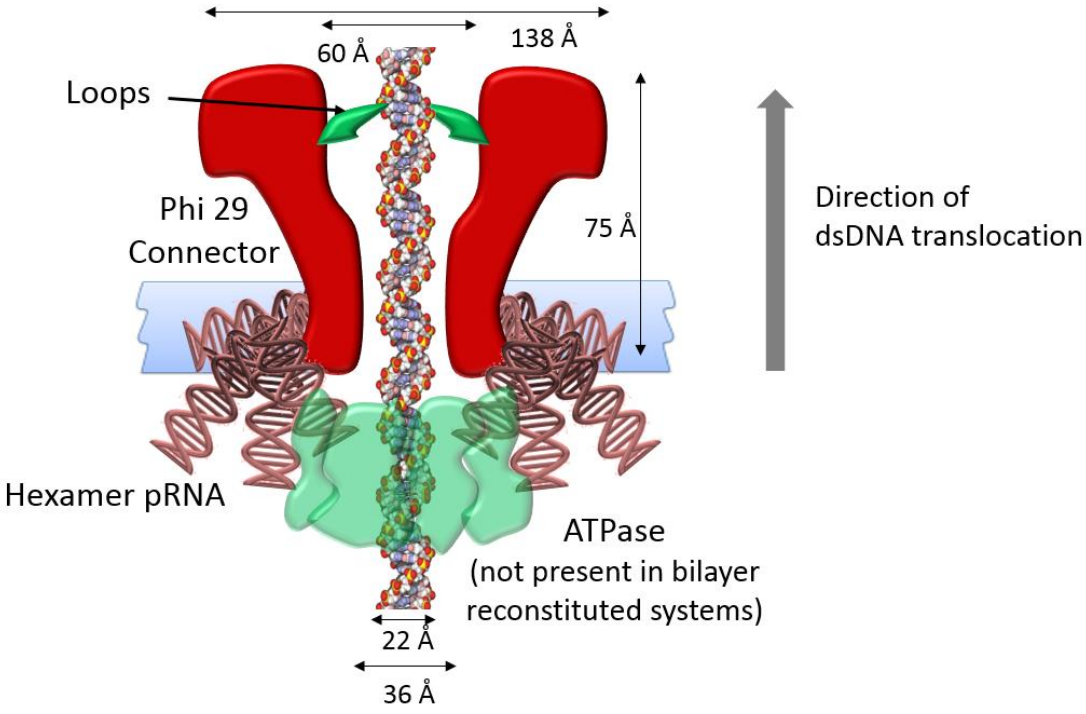

Figure 1.19 Modified phi 29 connector protein reconstituted in a lipid bilayer[91]. ATPase is indicated for illustrative purposes only, since in the realised system an applied potential was used to drive the dsDNA through the channel. The loops permit DNA transport in one direction only.

1.4 Light-driven transmembrane devices

Lipid bilayers provide a shortcut to achieving device complexity, since self-assembly facilitates the spatial organisation of discrete entities with specific orientations within a membrane. The repurposing of membrane-integrated protein molecular machines by combination with non-biological components to create biohybrid devices that possess novel functions is a growing branch in the evolution of synthetic molecular machines. In this regard, a number of devices that use light as an external stimuli or an energy source to drive transmembrane process away from equilibrium have been developed.

A. Light-switchable gated channels

Photoresponsive molecules have previously been used as “molecular glue” to modify the permeability of lipid bilayers to ions[94]. Similarly, synthetic moieties that develop a charge-separated state in response to photoirradiation have been appended to channel proteins causing them to undergo reversible conformational change, resulting in a gate. Synthetic light-responsive functionalities that undergo conformational change under photoirradiation (such as the *cis/trans* isomerisation) have been used in conjunction with biological channel proteins to allow optical control over membrane transport with extremely fine spatiotemporal resolution[95,96]. One example of this approach is provided by the work of Feringa at al[97], who reengineered the mechanosensitive channel of large conduction (MscL) from *E.coli*[70]. The protein was modified to have one cysteine residue per monomer which allowed the site-selective incorporation of light-responsive moieties (Figure 1.20). The addition of a photoresponsive cyanine group which could be reversibly switched between a neutral spiropyran state and a cationic merocyanine state allows the opening and closing of the channel by cycles of irradiation with 366 nm UV and relaxation under ambient visible light > 460 nm.

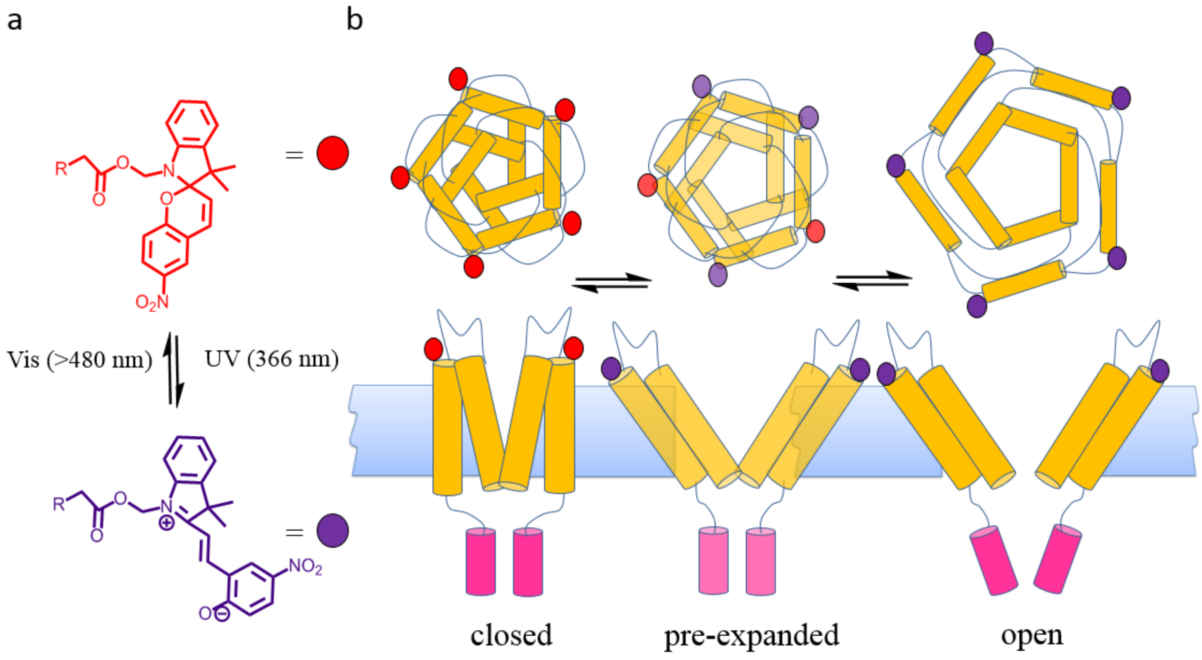

Figure 1.20 Synthetic light-gated ion channel prepared from mechanosensitive channel protein covalently modified with a photoactive spiropyran[97]. **a** Structure and UV-induced structural transition of the spiropyran moiety into the merocyanine moiety. **b** Conformational change associated with UV response of spiropyran.

B. Cyclic operation of light-driven transmembrane devices

The systems described in section 1.4 operate by simple switching mechanisms, and are therefore not capable of performing work such as the active transport of ions or molecules against a concentration gradient by turnover of a chemical fuel. Nevertheless, the self-organisation of molecular devices in lipid membranes provides the potential for coherent behaviour and the coupling of individual functions leading to the emergence of cyclic behaviour in the whole system. True transmembrane molecular machines operate *via* a series of cyclically repeating conformational changes that occur in response to orthogonal processes such as the consumption of a fuel and response to a transmembrane gradient as in the case of F_1F_0 ATP (synth)ase (see Section 1.1D).

The ATP synthase transmembrane protein assembly has been used as a component in a variety of artificially assembled devices. One very early example of a synthetic molecular machine that was incorporated into a membrane and exploited the gradient across it was reported by Gust et al[98] in 1998 (Figure 1.21). The key to achieving non-equilibrium

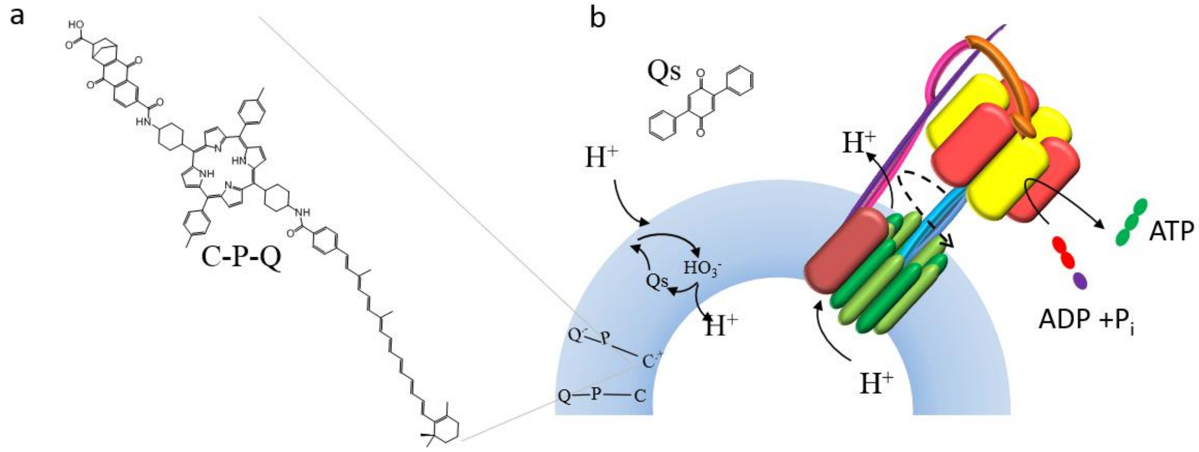

Figure 1.21 An artificial photosynthetic membrane[98]. **a** Structure of the C-P-Q energy-transfer triad. **b** Schematic operation of the assembled functional membrane.

properties was the addition of a membrane-soluble, synthetic, photoactive molecule known as C-P-Q. Although the energy transfer molecule C-P-Q has no inherent machine-like function, when multiple copies are embedded in the membrane with appropriate orientation they generate a transmembrane proton gradient electrogenically in response to excitation with visible light. The proton gradient attempts to return to an equilibrium state by spontaneously diffusing through the channel of the F_0 motor, driving rotation of the ATP synthase spindle along with the non-spontaneous synthesis of ATP from ADP and P_i.

Working towards mimicking the replenishing ability of living systems, Strano et al[99] developed a photoelectrochemical cell using a repurposed phospholipid, a membrane scaffold protein, and a photosynthetic reaction centre protein combined with synthetic carbon nanotubes. The system shown in Figure 1.22 was prepared from its constituents by dialysis of sodium cholate out of a reservoir containing all of the components. Since cholate inhibits the self-assembly process its removal by dialysis leads to the assembly of the desired arrangement of components. The novel architecture of the lipid bilayer nanodiscs and their association with carbon nanotubes permits a measurable voltage in an electrical circuit to be generated by the injection of photo-excited electrons from the photosynthetic reaction centre. The reaction centres are degraded during the commutation of photonic energy into electrical energy due to oxidative and free-radical damage. However, the system mimics the ability of corresponding natural systems to negate the effects of photodegradation *via* regenerative

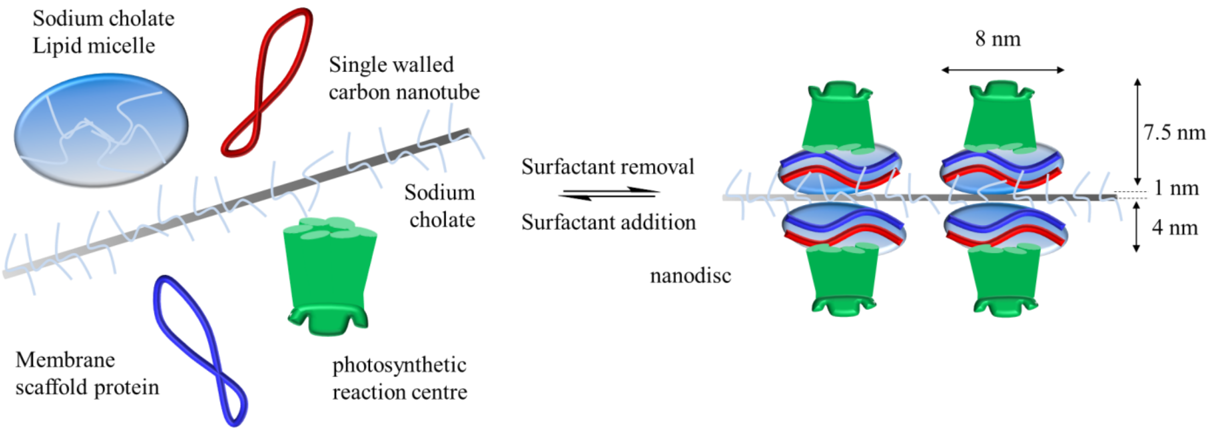

Figure 1.22 A self-assembled biohybrid photoelectrochemical cell[99]. **a** Components involved in the self-assembly of the device. **b** Dialysis of cholate from an aqueous solution containing the component proteins, lipids and carbon nanotubes affords the functioning photoelectrochemical cell.

self-assembly. Cycles of reverse and forward dialysis exchange the damaged components for native ones extending the lifetime of the system, thereby maintaining its efficiency.

Another strategy to obtain transmembrane nanostructures with novel functions was to combine multiple structurally unrelated membrane proteins[100]. Moreau et al used genetic engineering to modify an existing biological receptor/ion channel couple with a G-protein coupled receptor (Figure 1.23). The G-protein coupled receptor binds an analyte on one side of the membrane that drives a conformational change on the opposite side of the membrane. As the receptor is mechanically linked to the ion channel in the fusion protein, the ion channel opens in response to the binding of the analyte by the G-protein on the exterior of the bilayer. This leads to a change in the conductivity of the bilayer in which the protein resides, thereby transducing an electrical response from a chemical signal.

A wholly synthetic system that mimics some aspects of transmembrane photosynthetic proteins and ligand receptor gating was developed by Matile et al[101]. The system shown in Figure 1.24 is comprised of four *p*-octiphenyl chains each bearing eight core-substituted naphthalene-diimides. The complex self-assembles in a lipid bilayer such that the pi-surfaces of the naphthalene-diimides are stacked. In this geometry, irradiation of the complex at 638 nm causes electronic excitation which results in a transmembrane charge-separated state. The charge-separated state is maintained and work continually extracted from the system since the generated electrons and holes are used to drive a redox couple (reduction of quinones and oxidation of EDTA on opposite sides of the bilayer). The incorporation of the system into a bilayer allows the separation of the redox processes and leads to the generation of a proton gradient across the membrane. The addition of an intercalating

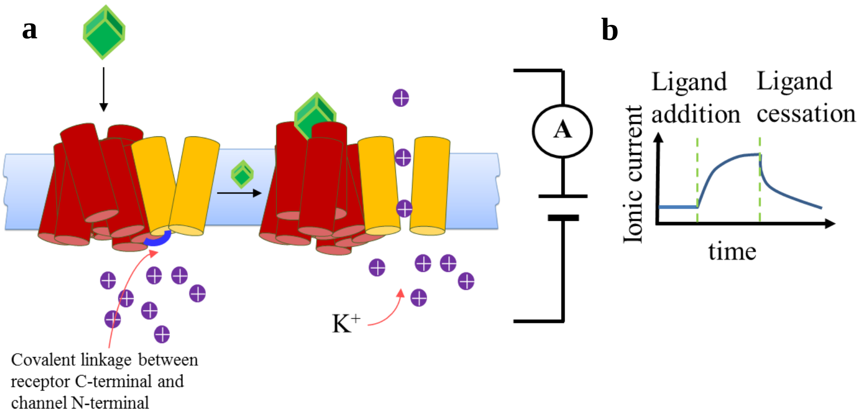

Figure 1.23 A ligand-gated transmembrane ion channel prepared by engineering the gene for one protein to include the gene for the other such that they are expressed as a single chimeric protein[100]. **a** Mechanical response of the system to the presence of the ligand. **b** Current response of the system upon addition and cessation of the ligand.

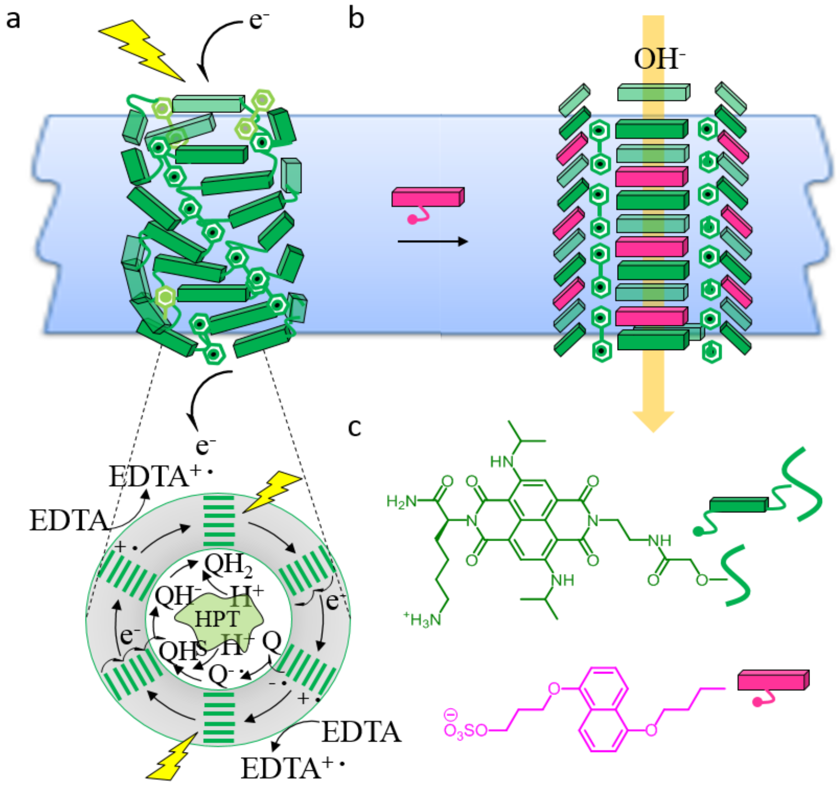

Figure 1.24 A self-assembled synthetic transmembrane ion channel[101]. **a** The rotationally symmetric structure is composed of stacked naphthalene diimides into a canted barrel structure. The structure provides a path for photoexcited electrons to transfer energy from one side of the bilayer to the other resulting in a long-lived charge-separated state and the production of a transmembrane proton gradient. **b** The addition of an intercalating species irreversibly alters the conformation of the barrel such that an ion channel is formed and hydroxide ions can flow through the channel until the charge is rebalanced. **c** Structures of naphthalene diimide and the naphthalene intercalator used in the ion channel assembly.

naphthalene species causes the transition of the canted helical structure of the photoactive complex into an open barrel. This newly generated channel allows the proton gradient to return to equilibrium by transmembrane proton/hydroxide conduction. Although the system does not include a means of utilising the proton gradient to regenerate the initial helical structure leading to an overall cyclically repetitious system, this is nonetheless a step on the way to synthetic transmembrane molecular machines.

1.5 Transmembrane nanomechanical devices

Open protein channels such as α-haemolysin (α-HL) are not molecular machines in their own right, but they have been used in conjunction with enzymes that *are* molecular machines to create transmembrane nanomechanical devices with machine-like properties. Thus far, these novel hybrid devices have found applications in single-molecule biophysics[72], and are developing platforms for nanopore-based DNA sequencing[73].

A. Monitoring sub-nanometre molecular motions within nanopores

As shown in Figure 1.25, Akeson et al used α-HL pores to examine the activity of phi 29 DNA polymerase on the single-molecule level[102]. This molecular assembly couples the turnover of dNTPs to a repetitious conformational change that ratchets the translocation of a macromolecule through the pore. Since the Phi 29 polymerase is particularly tolerant of high salt concentrations, this afforded a good signal-to-noise ratio when using ion current traces to distinguish between the different nanomechanical states observed.

In a subsequent study by Akeson et al[103] the protein AAA+ unfoldase ClpX was used to ratchet an engineered protein through an α-HL nanopore (Figure 1.26). The controlled translocation proceeded at rates that were slow enough to detect sequence specific features of the translocating species. This offers hope that nanopore sequencing of proteins using nanopore-based approaches as well as DNA might be feasible.

Efforts to create synthetic transmembrane molecular machines where the machine-like behaviour resides in the synthetic transmembrane component have thus far not been well developed.

One system that moves towards this goal was developed by Ghadiri et al[104,105] (Figure 1.27). A short biotin/streptavidin-capped DNA-PEG^{phos} (polyethyleneglycol phosphate) co-polymer was captured in the α-HL pore under an applied potential. The threaded strand was then complexed by a DNA primer to give a transmembrane rotaxanated architecture

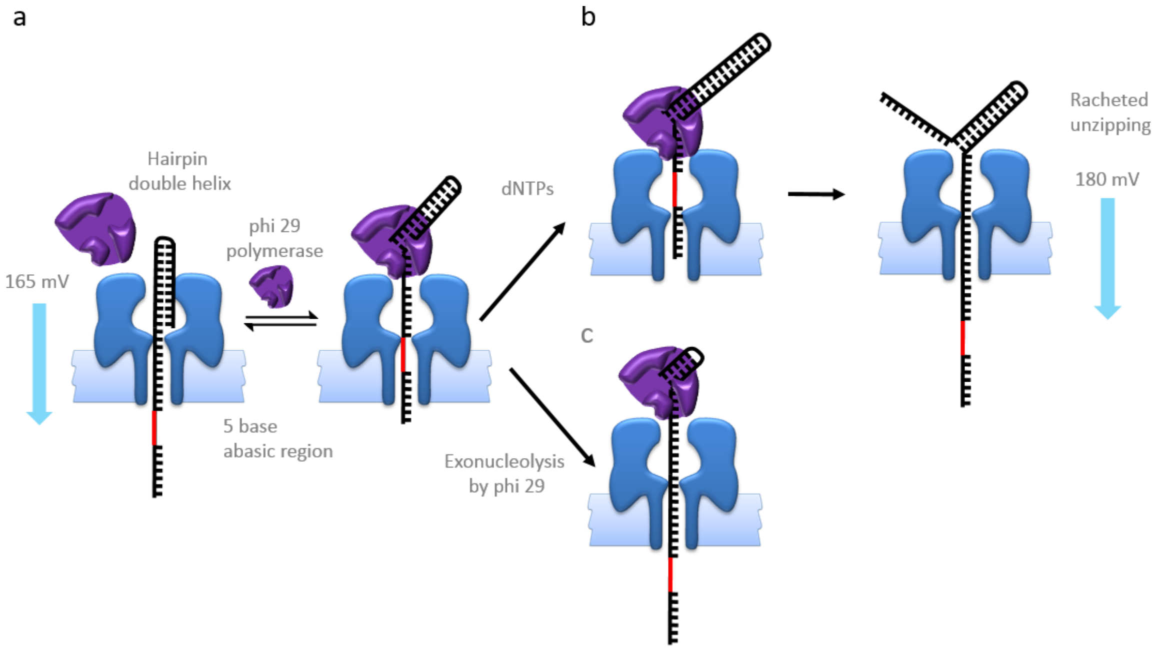

Figure 1.25 Schematic summary of Akeson's work using phi 29 polymerase[102]. **a** DNA-hairpin probe captured in an α-HL channel, the DNA-hairpin probe contains an abasic region shown in red, polymerase ratchets oligonucleotides through an α-HL pore, which in turn allows electronic observation of the enzyme binding. **b** Nucleotide incorporation. **c** Exonucleolysis and enzyme dissociation events as the translational position of the abasic region shifts with respect to the internal constriction of the nanopore, changing the flow of ions through the pore.

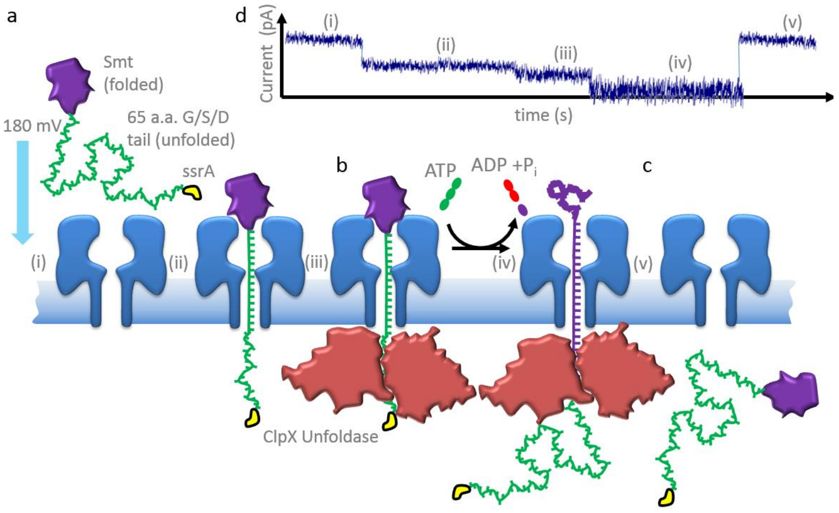

Figure 1.26 ATP-coupled transmembrane protein translocation through α-HL[103]. **a** A protein is captured in the α-HL pore by the electric field associated with an applied transmembrane potential. **b** The captured strand is bound by ClpX unfoldase, which couples cycles of the hydrolysis of ATP→ADP +Pi to conformational changes that ratchet the captured Smt protein through the α-HL while simultaneously unfolding it. **c** The translocated protein is presumed to return to its native conformation once it has been fully translocated. **d** Ion current traces associated with the different states of the capture→translocation/unfolding process.

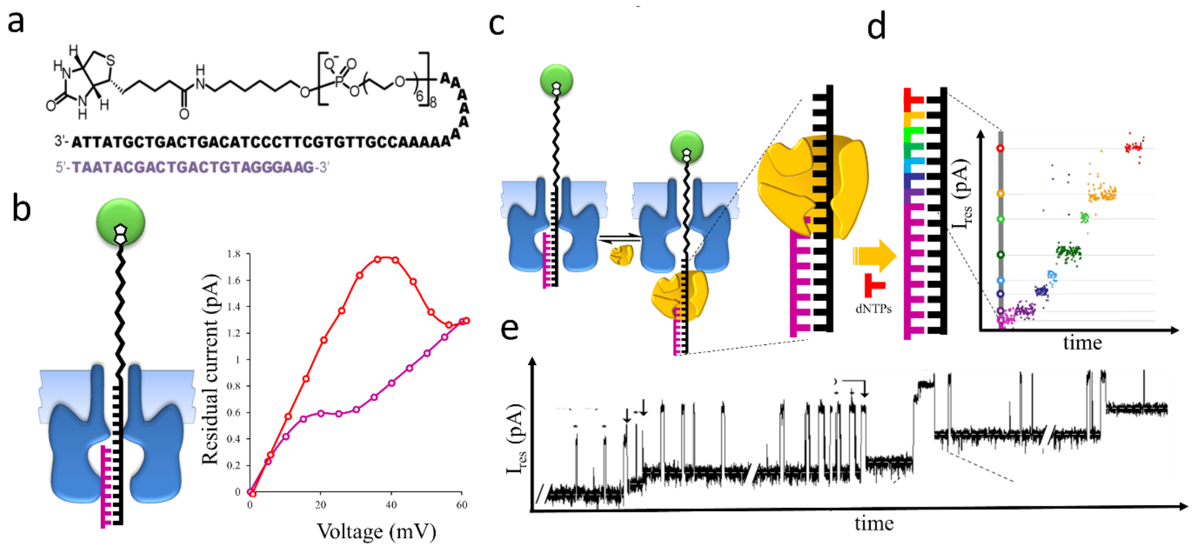

Figure 1.27 A transmembrane rotaxane for monitoring the translational position of the thread strand associated with enzyme catalysed primer extension[104,105]. **a** Sequence of the thread and primer strands used in assembly of the transmembrane rotaxane. **b** Cartoon of the assembled complex and *I/V* curves of rotaxanes constructed with starting primer (violet) and the fully extended primer (+7 bases) (red). The shape of the *I/V* trace varies according to the length of the primer. **c** The assembled rotaxane acts as a detection element for Klenow fragment (exo-) DNA polymerase and permits monitoring of the individual nucleotide incorporations as the primer is extended with the use of a stepped-voltage protocol, and in later work, **e** in real time.

(Figure 1.27b). A plot of the measured current response as the transmembrane voltage was varied gave a characteristic *I/V* trace. This was attributed to changes in the position of the equilibrium of the two extreme conformational states available to the rotaxane (duplex in, and duplex out of the pore) as the voltage was varied. The relative position of the inflection point in the *I/V* trace depended on the length of the DNA primer since this determines the relative proportions of DNA vs. the less bulky PEG threaded through the pore, and hence the magnitude of the ionic current flowing through the pore.

This device is distinct from many other studies that have used α-HL since the DNA polymerase turns over dNTPs and performs mechanical work against an applied potential that pulls the threaded DNA in the opposite direction. The device permits single-molecule observation of the binding and catalytic activity of DNA polymerases with single-nucleotide resolution, but only for a limited number of incorporations. The cyclic machine-like behaviour arises from the polymerase and not the synthetic assembled components. Another key challenge then is to embody cyclic behaviour in the synthetic component.

B. Transmembrane DNA transporters

One cyclic system has been constructed by Maglia et al[106] based on a mutant strain of a different transmembrane pore forming protein, Cytolysin A (ClyA) (Figure 1.28). In this system, the pore has a wider constriction than α-HL and can thus permit the passage of dsDNA. As with α-HL, the probability of the translocation of a charged species increases when larger potential differences are applied across the membrane. Simply increasing the potential however, is an indiscriminate way of increasing the rate of DNA transport. In Maglia's system the pore is modified with ssDNA (i) that recognises a specific sequence (ii) which can then be transported through the pore at potentials that are usually too low to overcome the energy barrier to translocation. The recognised strand is also complementary to a biotin-terminated DNA duplex (iii) such that the recognised strand and the duplex become associated with the recognition strand on the pore. The uncomplexed recognition strand is not restrained in the pore by the electric field at 50 mV, but the recognition complex is as it has a higher number of negative charges associated with it. This complex is therefore restrained and has a high probability of translocating the pore. This translocated complex is then exposed to streptavidin (iv) preventing it from translocating back through the pore. Finally, a displacement strand (v) attacks the toehold region of the recognised strand and dismantles the recognition complex, forming a new duplex and resulting in the dissociation of the components and the diffusion of the recognition strand back through the pore restoring the system to its initial condition.

In some respects this system can be considered a molecular machine - it operates in a cyclic manner and responds to a transmembrane chemical potential operating without external intervention after the addition of all the components. However, the system does not perform work; no covalent bonds are formed or broken by its operation, and the transport mechanism does not operate against the applied potential, but in the same direction as it. The action of the system is therefore best described as a catalytic translocase that lowers the activation barrier of a thermodynamically downhill process (translocation would still occur, albeit at a reduced rate, in the absence of the recognition strands). The capture step can be considered as an 'associative transition state' that accelerates the rate of electrokinetic transmembrane transport. The operation of the device is therefore mechanistically similar to the membrane-adapted silicon nitride channels described in Section 1.3B.

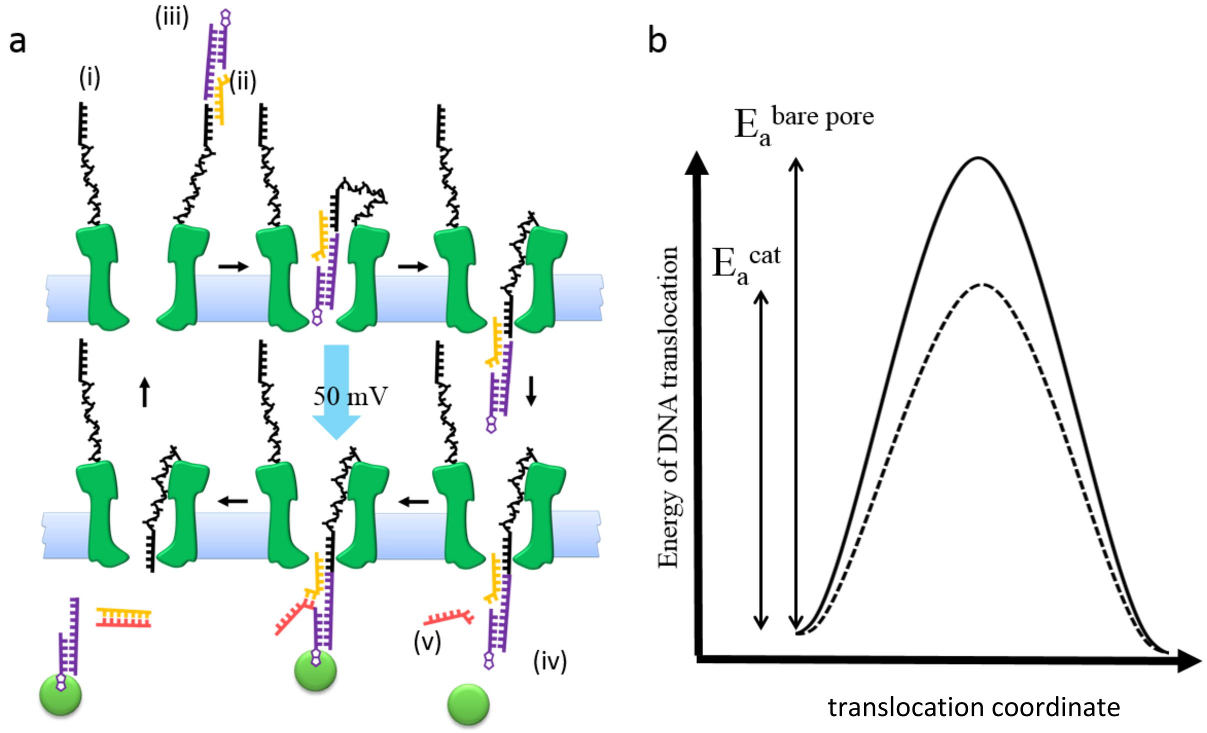

Figure 1.28 DNA transmembrane transporter based on mutant Cytolysin A protein[106]. **a** cycle of operation of the selective DNA transmembrane transporter. **b** Activation energy barrier to ssDNA translocation at 50 mV applied potential through an unmodified ClyA pore (solid line) and reduced activation barrier for the target sequence through the DNA-modified ClyA pore (dashed line).

1.6 Multi-compartment devices

Natural systems are hierarchically organised by partitioning with lipid bilayers into spatially close but chemically distinct nanoenvironments. This allows the generation of transmembrane potentials by molecular machines, which can then be used to do work in different compartments, giving rise to systems with emergent collective properties. Efforts to mimic this feature of natural systems in synthetic transmembrane assemblies have also been developed. Most notably Bayley and co-workers have demonstrated that aqueous droplets bound by lipid monolayers can be arranged in networks connected by bilayers which form at the interfaces between drops - so called droplet interface bilayer (DIB) networks[107] (Figure 1.29). The addition of protein channels that insert into the bilayers connecting drops allows ions and analytes to pass between the compartments in a specifically designed manner.

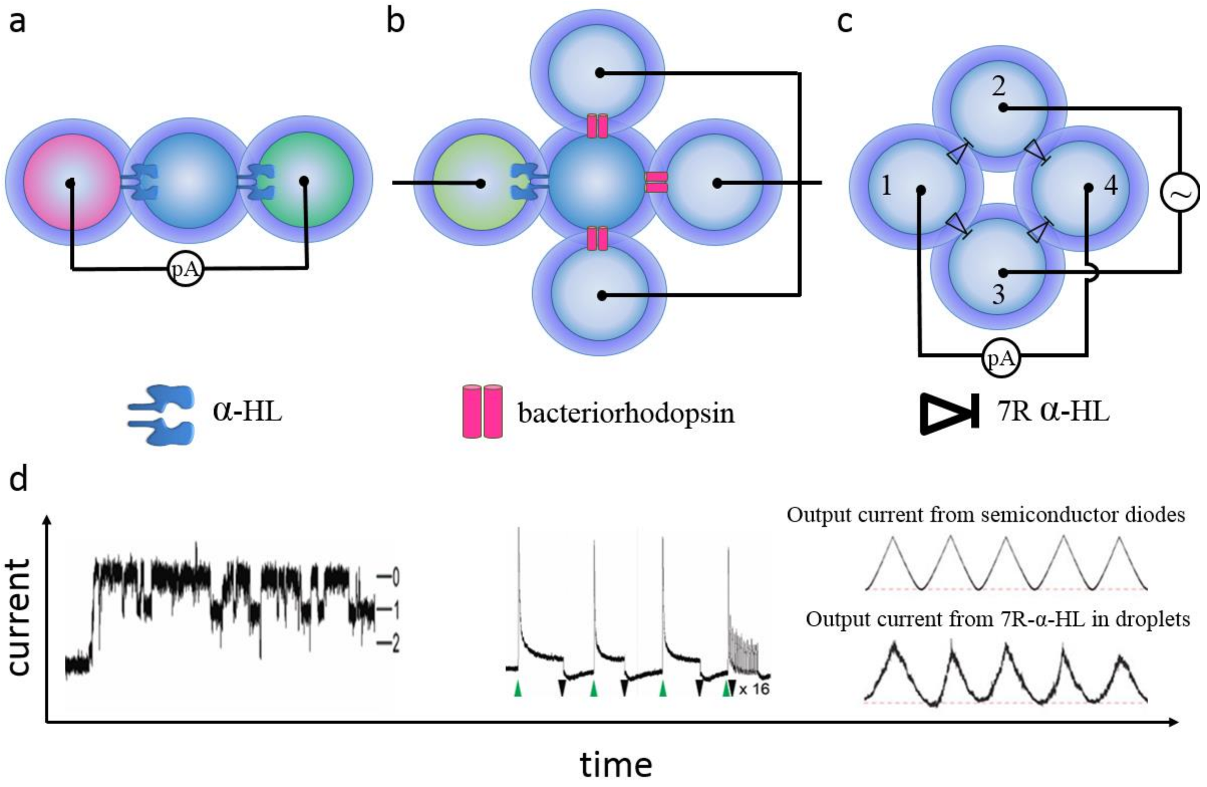

Figure 1.29 Simple circuits constructed from DIB networks connected by α-HL pores. **a** Three droplets containing different concentrations of NaCl form a battery due to the flow of charge carriers between the droplets through the α-HL pores[107]. This network results in a measurable pA-scale current when connected in series. **b** Five droplets are connected, three to a central drop with bacteriorhodopsin and the final one to the central drop with α-HL to form a rudimentary electronic light sensor. **c** Four droplets are connected at their interfaces by a mutant strain of α-HL that conducts ions in one direction only, this gives rise to half wave rectifying behaviour when the whole network is connected in a circuit as indicated[108]. **d** Current response behaviours of each system.

The careful selection of molecules contained in the individual drops and choice of genetically engineered mutants of α-haemolysin allow the assembly of sophisticated devices.In addition, the approach provides a means of monitoring of these processes by electrical and optical methods. Figure 1.29a[95] shows the arrangement of three droplets containing NaCl at different concentrations and different α-haemolysin mutants to form a DBI network that functions as a bio-battery. The red droplet contained 100 mM salt, 10 mM HEPES buffer and an anion-selective mutant haemolysin, the blue droplet contained 10 mM HEPES buffer and 1 M NaCl, while the green droplet contained 10 mM HEPES buffer, 1 M NaCl, a mutant haemolysin which reversibly binds β-cyclodextrin and 10 μM β-cyclodextrin. Insertion of the anion-selective α-haemolysin mutant at the red/blue bilayer interface and two of the β-cyclodextrin affinity mutants at the blue/green bilayer interface resulted in a net directional flow of current as ions flow through the pores down the concentration gradients to equilibrate the system. The binding of the β-cyclodextrin to one, both or neither of the mutant haemolysins at blue/green can be identified by the blockade level of the current response. The system is thus a self-powered chemical → electrical signal transduction mimic. Figure 1.29b[108] shows a DIB network used to create a light sensor that mimics the process of optical → chemical → electrical signal transduction in animal sight. Three buffered droplets containing bacteriorhodopsin (purple) each connected to a common electrode and one containing buffer and wild-type α-haemolysin (green) are arranged around a central drop containing only buffer. The α-haemolysin containing drop is connected to the counter electrode, completing the circuit. The bacteriarhodopsin and the α-haemolysin insert into the bilayer interfaces with the central droplet permitting the passage of ions through the system. Upon photoirradiation, the bacteriorhodopsin electrogenically pumps protons in one direction across the bilayer leading to a measureable net directional current in the circuit. In Figure 1.29c[108] a bridge rectifier is made from a network of four droplets, arranged such that each droplet has a bilayer interface with two others. Droplets 1, 2 and 3 contain a mutant α-haemolysin that has 49 arginine residues in the beta-barrel region (seven in each monomer) these are protonated when the device is in operation and subsequently only allows passage of current in one direction. The collective response of the circuit to an externally applied voltage across droplet 2 and 3 mimics a semiconductor diode bridge rectifier. This approach was recently extended[109] to make use of 3D printing technologies to produce heterogeneous droplet networks that mimic some of the properties of living tissues (Figure 1.30). The 3D printing technique allows the production of droplets of desired uniform volume down to < 100 picolitres and their placement in user-defined positions. The resulting jelly-like material can be prepared from droplets with different internal compositions. A structure printed from droplets of two different osmolarities was shown to undergo gross morphological changes due to the osmotic movement of water between droplets. Although the collective properties of the DBI networks are impressive, none of these systems constitutes a synthetic transmembrane molecular machine in the sense of an individual molecular assembly performing repeated cycles of mechanical work. Nonetheless, these types of interconnected multi-compartment systems may hold great promise as hosts for complicated systems of collectively operating transmembrane molecular machines.

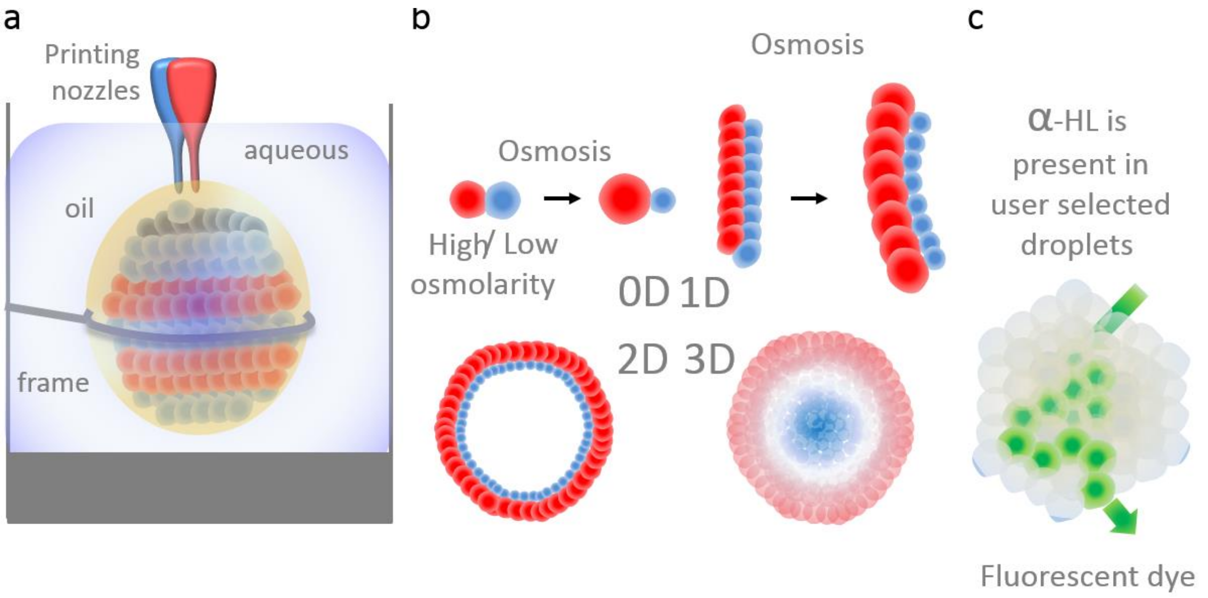

Figure 1.30 3D printed DIB networks[109]. **a** Technique used for the 3D printing of DIBs. **b** Different osmolarities of interfaced droplets leads to the flow of water between droplets causing morphological changes in DIB networks over time. These dynamic structures facilitate the printing of 0-, 1-, 2- and 3-dimensional DIB networks that change morphology after they are printed. **c** Inclusion of α-HL in specific droplets leads to programmability in the path of the flow of ions and dye molecules through a 3D DIB network.

1.7 Conclusions and future directions

Many avenues are being investigated in the development of synthetic molecular machines. In addition to wholly synthetic systems, some of the most effective demonstrations involve the use of repurposed biomolecules, as is particularly well illustrated by progress in the field of DNA nanotechnology. The use of protein scaffolds is also a well-established approach in the emerging field of synthetic transmembrane molecular machines, and impressively complex yet elegant functional architectures have been developed. Nonetheless, there is still scope for incorporating lessons learnt in the development of both DNA and synthetic nanomachines to adorn transmembrane architectures with novel functions. It therefore seems likely that mimicking and borrowing from natural systems will continue to be a guiding principle in the development of transmembrane molecular machines. Specific criteria that need to be attained in this objective are repetitious, cyclical operation, and the coupling of chemical reactions and conformational changes to perform mechanical work and/or to establish transmembrane potentials. However, there is a paucity of rationally designed transmembrane systems that satisfy all of the defining characteristics of transmembrane molecular machines.

1.8 References

1. Goodsell, D. S., *Bionanotechnology lessons from nature*. Wiley-Liss: 2004; p 337.
2. Gomis-Ruth, F. X.; Moncalian, G.; Perez-Luque, R.; Gonzalez, A.; Cabezon, E.; de la Cruz, F.; Coll, M., The bacterial conjugation protein TrwB resembles ring helicases and F1-ATPase. *Nature* **2001,** *409* (6820), 637-641.
3. Klok, M.; Boyle, N.; Pryce, M. T.; Meetsma, A.; Browne, W. R.; Feringa, B. L., MHz unidirectional rotation of molecular rotary motors. *J. Am. Chem. Soc.* **2008,** *130* (32), 10484-10485.
4. Brouwer, A. M.; Frochot, C.; Gatti, F. G.; Leigh, D. A.; Mottier, L. c.; Paolucci, F.; Roffia, S.; Wurpel, G. W. H., Photoinduction of fast, reversible translational motion in a hydrogen-bonded molecular shuttle. *Science* **2001,** *291* (5511), 2124-2128.
5. Carroll, G. T.; London, G.; Landaluce, T. F.; Rudolf, P.; Feringa, B. L., Adhesion of photon-driven molecular motors to surfaces via 1,3-dipolar cycloadditions: effect of interfacial interactions on molecular motion. *ACS Nano* **2011,** *5* (1), 622-630.
6. Berna, J.; Leigh, D. A.; Lubomska, M.; Mendoza, S. M.; Perez, E. M.; Rudolf, P.; Teobaldi, G.; Zerbetto, F., Macroscopic transport by synthetic molecular machines. *Nat. Mater.* **2005,** *4* (9), 704-710.
7. Milano, F.; Tangorra, R. R.; Hassan Omar, O.; Ragni, R.; Operamolla, A.; Agostiano, A.; Farinola, G. M.; Trotta, M., Enhancing the light harvesting capability of a photosynthetic reaction center by a tailored molecular fluorophore. *Angew. Chem. Int. Ed.* **2012,** *51* (44), 11019-11023.
8. Motré, A.; Li, Y.; Kong, H., Enhancing helicase-dependent amplification by fusing the helicase with the DNA polymerase. *Gene* **2008,** *420* (1), 17-22.
9. Lubner, C. E.; Heinnickel, M.; Bryant, D. A.; Golbeck, J. H., Wiring photosystem I for electron transfer to a tethered redox dye. *Ener. Environ. Sci.* **2011,** *4* (7), 2428-2434.
10. van den Heuvel, M. G. L.; Dekker, C., Motor proteins at work for nanotechnology. *Science* **2007,** *317* (5836), 333-336.
11. Michaelis, J.; Muschielok, A.; Andrecka, J.; Kügel, W.; Moffitt, J. R., DNA based molecular motors. *Phys. Life Rev.* **2009,** *6* (4), 250-266.
12. Dietrich-Buchecker, C.; Jimenez-Molero, M. C.; Sartor, V.; Sauvage, J. P., Rotaxanes and catenanes as prototypes of molecular machines and motors. *Pure Appl. Chem.* **2003,** *75* (10), 1383-1393.
13. Bath, J.; Turberfield, A. J., DNA nanomachines. *Nat. Nanotechnol.* **2007,** *2* (5), 275-284.
14. He, Y.; Liu, D. R., Autonomous multistep organic synthesis in a single isothermal solution mediated by a DNA walker. *Nat. Nanotechnol.* **2010,** *5* (11), 778-782.
15. Ishitsuka, Y.; Ha, T., DNA nanotechnology: A nanomachine goes live. *Nat. Nanotechnol.* **2009,** *4* (5), 281-282.
16. You, M.; Chen, Y.; Zhang, X.; Liu, H.; Wang, R.; Wang, K.; Williams, K. R.; Tan, W., An Autonomous and controllable light-driven DNA walking device. *Angew. Chem.* **2012,** *124* (10), 2507-2510.
17. Wilner, O. I.; Weizmann, Y.; Gill, R.; Lioubashevski, O.; Freeman, R.; Willner, I., Enzyme cascades activated on topologically programmed DNA scaffolds. *Nat. Nanotechnol.* **2009,** *4* (4), 249-254.
18. Liu, Y.; Du, J.; Yan, M.; Lau, M. Y.; Hu, J.; Han, H.; Yang, O. O.; Liang, S.; Wei, W.; Wang, H.; Li, J.; Zhu, X.; Shi, L.; Chen, W.; Ji, C.; Lu, Y., Biomimetic enzyme nanocomplexes and their use as antidotes and preventive measures for alcohol intoxication. *Nat. Nanotechnol.* **2013,** *8* (3), 187-192.
19. Dolezal, P.; Likic, V.; Tachezy, J.; Lithgow, T., Evolution of the molecular machines for protein import into mitochondria. *Science* **2006,** *313* (5785), 314-318.
20. Hugel, T.; Michaelis, J.; Hetherington, C. L.; Jardine, P. J.; Grimes, S.; Walter, J. M.; Falk, W.; Anderson, D. L.; Bustamante, C., Experimental Test of connector rotation during DNA packaging into bacteriophage φ29 capsids. *PLoS Biol* **2007,** *5* (3), e59.
21. Erhardt, M.; Namba, K.; Hughes, K. T., Bacterial nanomachines: the flagellum and Type III injectisome. *Cold Spring Harbor Persp. Biol.* **2010,** *2* (11).
22. Noji, H.; Yasuda, R.; Yoshida, M.; Kinosita, K., Direct observation of the rotation of F1-ATPase. *Nature* **1997,** *386* (6622), 299-302.
23. Li, G.-W.; Xie, X. S., Central dogma at the single-molecule level in living cells. *Nature* **2011,** *475* (7356), 308-315.
24. Astumian, R. D., Design principles for Brownian molecular machines: how to swim in molasses and walk in a hurricane. *PhysChemChemPhys* **2007,** *9* (37), 5067.
25. Weber, G., Energetics of ligand binding to protein. In *Adv. Prot. Chem.*, Academic Press: 1975; Vol. 29, pp 1 -83.
26. (a) Závodszky, P.; Hajdú, I., Evolution of the concept of conformational dynamics of enzyme functions over half of a century: A personal view. *Biopolymers* **2013,** *99* (4), 263-269; (b) Alper, K. O.; Singla,

M.; Stone, J. L.; Bagdassarian, C. K., Correlated conformational fluctuations during enzymatic catalysis: Implications for catalytic rate enhancement. *Prot. Sci.* **2001,** *10* (7), 1319-1330.

27. Eisenmesser, E. Z.; Millet, O.; Labeikovsky, W.; Korzhnev, D. M.; Wolf-Watz, M.; Bosco, D. A.; Skalicky, J. J.; Kay, L. E.; Kern, D., Intrinsic dynamics of an enzyme underlies catalysis. *Nature* **2005,** *438* (7064), 117-121.
28. Steitz, T. A., DNA polymerases: structural diversity and common mechanisms. *J. Biol. Chem.* **1999,** *274* (25), 17395-17398.
29. Biertümpfel, C.; Zhao, Y.; Kondo, Y.; Ramón-Maiques, S.; Gregory, M.; Lee, J. Y.; Masutani, C.; Lehmann, A. R.; Hanaoka, F.; Yang, W., Structure and mechanism of human DNA polymerase [eegr]. *Nature* **2010,** *465* (7301), 1044-1048.
30. Barbara Medagli, S. O., Structure and mechanism of hexameric helicases. In *DNA Helicases and DNA Motor Proteins* Spies, M., Ed. Springer Science: 2013.
31. Soengas, M. a. S.; Gutiérrez, C.; Salas, M., Helix-destabilizing activity of φ29 single-stranded DNA binding protein: effect on the elongation Rate during strand displacement DNA replication. *J. Mol. Biol.* **1995,** *253* (4), 517-529.
32. Hashem, Y.; des Georges, A.; Fu, J.; Buss, S. N.; Jossinet, F.; Jobe, A.; Zhang, Q.; Liao, H. Y.; Grassucci, R. A.; Bajaj, C.; Westhof, E.; Madison-Antenucci, S.; Frank, J., High-resolution cryo-electron microscopy structure of the Trypanosoma brucei ribosome. *Nature* **2013,** *494* (7437), 385-389.
33. Schmeing, T. M.; Ramakrishnan, V., What recent ribosome structures have revealed about the mechanism of translation. *Nature* **2009,** *461* (7268), 1234-1242.
34. Sanbonmatsu, K.; Blanchard, S.; Whitford, P., Molecular dynamics simulations of the ribosome. in *Biophysical approaches to translational control of gene expression*, Dinman, J. D., Ed. Springer New York: 2013; Vol. 1, pp 51-68.
35. Zhang, J.; Baker, M. L.; Schroder, G. F.; Douglas, N. R.; Reissmann, S.; Jakana, J.; Dougherty, M.; Fu, C. J.; Levitt, M.; Ludtke, S. J.; Frydman, J.; Chiu, W., Mechanism of folding chamber closure in a group II chaperonin. *Nature* **2010,** *463* (7279), 379-383.
36. Maliga, Z.; Junqueira, M.; Toyoda, Y.; Ettinger, A.; Mora-Bermudez, F.; Klemm, R. W.; Vasilj, A.; Guhr, E.; Ibarlucea-Benitez, I.; Poser, I.; Bonifacio, E.; Huttner, W. B.; Shevchenko, A.; Hyman, A. A., A genomic toolkit to investigate kinesin and myosin motor function in cells. *Nat. Cell Biol.* **2013,** *15, 325-334*
37. Chen, I.; Christie, P. J.; Dubnau, D., The ins and outs of DNA transfer in bacteria. *Science* **2005,** *310* (5753), 1456-1460.
38. Vale, R. D.; Milligan, R. A., The way things move: looking under the hood of molecular motor proteins. *Science* **2000,** *288* (5463), 88-95.
39. Ali, M. Y.; Lu, H.; Bookwalter, C. S.; Warshaw, D. M.; Trybus, K. M., Myosin V and Kinesin act as tethers to enhance each others' processivity. *Proc. Natl. Acad. Sci. USA* **2008,** *105* (12), 4691-4696.
40. Arai, S.; Saijo, S.; Suzuki, K.; Mizutani, K.; Kakinuma, Y.; Ishizuka-Katsura, Y.; Ohsawa, N.; Terada, T.; Shirouzu, M.; Yokoyama, S.; Iwata, S.; Yamato, I.; Murata, T., Rotation mechanism of Enterococcus hirae V1-ATPase based on asymmetric crystal structures. *Nature* **2013,** *493* (7434), 703-707.
41. Weber, J., Structural biology: Toward the ATP synthase mechanism. *Nat. Chem. Biol.* **2010,** *6* (11), 794-795.
42. Symersky, J.; Pagadala, V.; Osowski, D.; Krah, A.; Meier, T.; Faraldo-Gómez, J. D.; Mueller, D. M., Structure of the c10 ring of the yeast mitochondrial ATP synthase in the open conformation. *Nat. Struct. Mol. Biol.* **2012,** *19* (5), 485-491.
43. Priya, R.; Biuković, G.; Manimekalai, M.; Lim, J.; Rao, S. S.; Grüber, G., Solution structure of subunit γ (γ1-204) of the Mycobacterium tuberculosis F-ATP synthase and the unique loop of γ165-178, representing a novel TB drug target. *J. Bioenerg. Biomemb.* **2013,** *45* (1-2), 121-129.
44. Börsch, M., Monitoring subunit rotation in single FRET-labeled FoF1-ATP synthase in an anti-Brownian electrokinetic trap. *Quant. Biol. Biomol.* **2013**.
45. Lau, W. C. Y.; Baker, L. A.; Rubinstein, J. L., Cryo-EM Structure of the Yeast ATP Synthase. *J. Mol. Biol.* **2008,** *382* (5), 1256-1264.
46. Stewart, A. G.; Sobti, M.; Harvey, R. P.; Stock, D., Rotary ATPases: Models, machine elements and technical specifications. *BioArchitecture* **2013,** *3* (1), 0-10.
47. Ryu, W. S.; Berry, R. M.; Berg, H. C., Torque-generating units of the flagellar motor of Escherichia coli have a high duty ratio. *Nature* **2000,** *403* (6768), 444-447.
48. Berg, H. C.; Anderson, R. A., Bacteria swim by rotating their flagellar filaments. *Nature* **1973,** *245* (5425), 380-382.

49. Zhao, X.; Zhang, K.; Boquoi, T.; Hu, B.; Motaleb, M. A.; Miller, K. A.; James, M. E.; Charon, N. W.; Manson, M. D.; Norris, S. J.; Li, C.; Liu, J., Cryoelectron tomography reveals the sequential assembly of bacterial flagella in Borrelia burgdorferi. *Proc. Natl. Acad. Sci. USA* **2013,** *110* (35), 14390-14395.
50. Yonekura, K.; Maki-Yonekura, S.; Namba, K., Complete atomic model of the bacterial flagellar filament by electron cryomicroscopy. *Nature* **2003,** *424* (6949), 643-650.
51. Gadsby, D. C., Ion channels versus ion pumps: the principal difference, in principle. *Nat. Rev. Mol. Cell Biol.* **2009,** *10* (5), 344-352.
52. Lee, C.; Kang, H. J.; von Ballmoos, C.; Newstead, S.; Uzdavinys, P.; Dotson, D. L.; Iwata, S.; Beckstein, O.; Cameron, A. D.; Drew, D., A two-domain elevator mechanism for sodium/proton antiport. *Nature* **2013,** *501* (7468), 573-577.
53. Kay, E. R.; Leigh, D. A.; Zerbetto, F., Synthetic molecular motors and mechanical machines. *Angew. Chem. Int. Ed.* **2007,** *46* (1-2), 72-191.
54. Lewandowski, B.; De Bo, G.; Ward, J. W.; Papmeyer, M.; Kuschel, S.; Aldegunde, M. J.; Gramlich, P. M. E.; Heckmann, D.; Goldup, S. M.; D'Souza, D. M.; Fernandes, A. E.; Leigh, D. A., Sequence-specific peptide synthesis by an artificial small-molecule machine. *Science* **2013,** *339* (6116), 189-193.
55. Green, S.; Bath, J.; Turberfield, A., Coordinated chemomechanical cycles: A mechanism for autonomous molecular motion. *Phys. Rev. Lett.* **2008,** *101* (23).
56. Leigh, D. A.; Wong, J. K. Y.; Dehez, F.; Zerbetto, F., Unidirectional rotation in a mechanically interlocked molecular rotor. *Nature* **2003,** *424* (6945), 174-179.
57. Koumura, N.; Zijlstra, R. W. J.; van Delden, R. A.; Harada, N.; Feringa, B. L., Light-driven monodirectional molecular rotor. *Nature* **1999,** *401* (6749), 152-155.
58. Strambi, A.; Durbeej, B.; Ferré, N.; Olivucci, M., Anabaena sensory rhodopsin is a light-driven unidirectional rotor. *Proc. Natl. Acad. Sci.* **2010,** *107* (50), 21322-21326.
59. Eelkema, R.; Pollard, M. M.; Vicario, J.; Katsonis, N.; Ramon, B. S.; Bastiaansen, C. W. M.; Broer, D. J.; Feringa, B. L., Molecular machines: Nanomotor rotates microscale objects. *Nature* **2006,** *440* (7081), 163-163.
60. Astumian, R. D., Thermodynamics and kinetics of molecular motors. *Biophys. J.* **2010,** *98* (11), 2401-2409.
61. von Delius, M.; Geertsema, E. M.; Leigh, D. A., A synthetic small molecule that can walk down a track. *Nat. Chem.* **2010,** *2* (2), 96-101.
62. Huang, T. J.; Brough, B.; Ho, C.-M.; Liu, Y.; Flood, A. H.; Bonvallet, P. A.; Tseng, H.-R.; Stoddart, J. F.; Baller, M.; Magonov, S., A nanomechanical device based on linear molecular motors. *App. Phys. Lett.* **2004,** *85* (22), 5391-5393.
63. Modi, S.; Swetha, M. G.; Goswami, D.; Gupta, G. D.; Mayor, S.; Krishnan, Y., A DNA nanomachine that maps spatial and temporal pH changes inside living cells. *Nat. Nanotechnol.* **2009,** *4* (5), 325-330.
64. Wickham, S. F. J.; Endo, M.; Katsuda, Y.; Hidaka, K.; Bath, J.; Sugiyama, H.; Turberfield, A. J., Direct observation of stepwise movement of a synthetic molecular transporter. *Nat. Nanotechnol.* **2011,** *6* (3), 166-169.
65. Sessler, J. L.; Lawrence, C. M.; Jayawickramarajah, J., Molecular recognition via base-pairing. *Chem. Soc. Rev.* **2007,** *36* (2), 314-325.
66. Cabezon, E.; Lanza, V. F.; Arechaga, I., Membrane-associated nanomotors for macromolecular transport. *Curr. Op. Biotechnol.* **2012,** *23* (4), 537-544.
67. Davies, J. P.; Chen, F. W.; Ioannou, Y. A., Transmembrane molecular pump activity of Niemann-Pick C1 protein. *Science* **2000,** *290* (5500), 2295-2298.
68. Nan, B.; Bandaria, J. N.; Moghtaderi, A.; Sun, I.-H.; Yildiz, A.; Zusman, D. R., Flagella stator homologs function as motors for myxobacterial gliding motility by moving in helical trajectories. *Proc. Natl. Acad. Sci. USA* **2013**.
69. Papanikou, E.; Karamanou, S.; Economou, A., Bacterial protein secretion through the translocase nanomachine. *Nat. Rev. Microbiol.* **2007,** *5* (11), 839-851.
70. Vasquez, V.; Perozo, E., Structural biology: A channel with a twist. *Nature* **2009,** *461* (7260), 47-49.
71. Song, L.; Hobaugh, M. R.; Shustak, C.; Cheley, S.; Bayley, H.; Gouaux, J. E., Structure of Staphylococcal α-hemolysin, a heptameric transmembrane pore. *Science* **1996,** *274* (5294), 1859-1865.
72. Ma, L.; Cockroft, S. L., Biological nanopores for single-molecule biophysics. *ChemBioChem* **2010,** *11* (1), 25-34.
73. Wanunu, M., Nanopores: A journey towards DNA sequencing. *Phys. Life Rev.* **2012,** *9* (2), 125-158.
74. Wen, L.; Hou, X.; Tian, Y.; Nie, F.-Q.; Song, Y.; Zhai, J.; Jiang, L., Bioinspired smart gating of nanochannels toward photoelectric-conversion systems. *Adv. Mater.* **2010,** *22* (9), 1021-1024.
75. Hou, X.; Guo, W.; Jiang, L., Biomimetic smart nanopores and nanochannels. *Chem. Soc. Rev.* **2011,** *40* (5), 2385-2401.

76. Harrell, C. C.; Kohli, P.; Siwy, Z.; Martin, C. R., DNA−nanotube artificial ion channels. *J. Am. Chem. Soc.* **2004,** *126* (48), 15646-15647.

77. Xia, F.; Guo, W.; Mao, Y.; Hou, X.; Xue, J.; Xia, H.; Wang, L.; Song, Y.; Ji, H.; Ouyang, Q.; Wang, Y.; Jiang, L., Gating of single synthetic nanopores by proton-driven DNA molecular motors. *J. Am. Chem. Soc.* **2008,** *130* (26), 8345-8350.

78. Hou, X.; Yang, F.; Li, L.; Song, Y.; Jiang, L.; Zhu, D., A biomimetic asymmetric responsive single nanochannel. *J. Am. Chem. Soc.* **2010,** *132* (33), 11736-11742.

79. Yameen, B.; Ali, M.; Neumann, R.; Ensinger, W.; Knoll, W.; Azzaroni, O., Ionic transport through single solid-state nanopores controlled with thermally nanoactuated macromolecular gates. *Small* **2009,** *5* (11), 1287-1291.

80. Guo, W.; Xia, H.; Xia, F.; Hou, X.; Cao, L.; Wang, L.; Xue, J.; Zhang, G.; Song, Y.; Zhu, D.; Wang, Y.; Jiang, L., Current rectification in temperature-responsive single nanopores. *ChemPhysChem* **2010,** *11* (4), 859-864.

81. Wang, G.; Bohaty, A. K.; Zharov, I.; White, H. S., Photon gated transport at the glass nanopore electrode. *J. Am. Chem. Soc.* **2006,** *128* (41), 13553-13558.

82. Tian, Y.; Hou, X.; Wen, L.; Guo, W.; Song, Y.; Sun, H.; Wang, Y.; Jiang, L.; Zhu, D., A biomimetic zinc activated ion channel. *Chem. Commun.* **2010,** *46* (10), 1682-1684.

83. Han, C.; Hou, X.; Zhang, H.; Guo, W.; Li, H.; Jiang, L., Enantioselective recognition in biomimetic single artificial nanochannels. *J. Am. Chem. Soc.* **2011,** *133* (20), 7644-7647.

84. Lee, S. B.; Mitchell, D. T.; Trofin, L.; Nevanen, T. K.; Söderlund, H.; Martin, C. R., Antibody-based bio-nanotube membranes for enantiomeric drug separations. *Science* **2002,** *296* (5576), 2198-2200.

85. Yusko, E. C.; Johnson, J. M.; Majd, S.; Prangkio, P.; Rollings, R. C.; Li, J.; Yang, J.; Mayer, M., Controlling protein translocation through nanopores with bio-inspired fluid walls. *Nat. Nanotechnol.* **2011,** *6* (4), 253-260.

86. Hall, A. R.; Scott, A.; Rotem, D.; Mehta, K. K.; Bayley, H.; Dekker, C., Hybrid pore formation by directed insertion of [alpha]-haemolysin into solid-state nanopores. *Nat. Nanotechnol.* **2010,** *5* (12), 874-877.

87. Ghadiri, M. R.; Granja, J. R.; Buehler, L. K., Artificial transmembrane ion channels from self-assembling peptide nanotubes. *Nature* **1994,** *369* (6478), 301-304.

88. Hu, X.-B.; Chen, Z.; Tang, G.; Hou, J.-L.; Li, Z.-T., Single-molecular artificial transmembrane water channels. *J. Am. Chem. Soc.* **2012,** *134* (20), 8384-8387.

89. Matile, S.; Vargas Jentzsch, A.; Montenegro, J.; Fin, A., Recent synthetic transport systems. *Chem. Soc. Rev.* **2011,** *40* (5), 2453-2474.

90. Langecker, M.; Arnaut, V.; Martin, T. G.; List, J.; Renner, S.; Mayer, M.; Dietz, H.; Simmel, F. C., Synthetic lipid membrane channels formed by designed DNA nanostructures. *Science* **2012,** *338* (6109), 932-936.

91. Wendell, D.; Jing, P.; Geng, J.; Subramaniam, V.; Lee, T. J.; Montemagno, C.; Guo, P., Translocation of double-stranded DNA through membrane-adapted phi29 motor protein nanopores. *Nat. Nanotechnol.* **2009,** *4* (11), 765-772.

92. Guo, P., Structure and function of φ29 hexameric RNA that drives the viral DNA packaging motor: Review. In *Progress in Nucleic Acid Research and Molecular Biology*, Academic Press: 2002; Vol. Volume 72, pp 415-472.

93. Zhao, Z.; Khisamutdinov, E.; Schwartz, C.; Guo, P., Mechanism of one-way traffic of hexameric Phi29 DNA packaging motor with four electropositive relaying layers facilitating antiparallel revolution. *ACS Nano* **2013,** *7* (5), 4082-4092.

94. Suzuki, Y.; Okuro, K.; Takeuchi, T.; Aida, T., Friction-mediated dynamic disordering of phospholipid membrane by mechanical motions of photoresponsive molecular glue: Activation of ion permeation. *J. Am. Chem. Soc.* **2012,** *134* (37), 15273-15276.

95. Gorostiza, P.; Isacoff, E. Y., Optical switches for remote and noninvasive control of cell signaling. *Science* **2008,** *322* (5900), 395-399.

96. Gorostiza, P.; Isacoff, E. Y., Nanoengineering ion channels for optical control. *Physiology* **2008,** *23* (5), 238-247.

97. Koçer, A.; Walko, M.; Meijberg, W.; Feringa, B. L., A Light-actuated nanovalve derived from a channel protein. *Science* **2005,** *309* (5735), 755-758.

98. Steinberg-Yfrach, G.; Rigaud, J.-L.; Durantini, E. N.; Moore, A. L.; Gust, D.; Moore, T. A., Light-driven production of ATP catalysed by F0F1-ATP synthase in an artificial photosynthetic membrane. *Nature* **1998,** *392* (6675), 479-482.

99. Ham, M.-H.; Choi, J. H.; Boghossian, A. A.; Jeng, E. S.; Graff, R. A.; Heller, D. A.; Chang, A. C.; Mattis, A.; Bayburt, T. H.; Grinkova, Y. V.; Zeiger, A. S.; Van Vliet, K. J.; Hobbie, E. K.; Sligar, S.

G.; Wraight, C. A.; Strano, M. S., Photoelectrochemical complexes for solar energy conversion that chemically and autonomously regenerate. *Nat. Chem.* **2010,** *2* (11), 929-936.

100. Moreau, C. J.; Dupuis, J. P.; Revilloud, J.; Arumugam, K.; Vivaudou, M., Coupling ion channels to receptors for biomolecule sensing. *Nat. Nanotechnol.* **2008,** *3* (10), 620-625.
101. Bhosale, S.; Sisson, A. L.; Talukdar, P.; Fürstenberg, A.; Banerji, N.; Vauthey, E.; Bollot, G.; Mareda, J.; Röger, C.; Würthner, F.; Sakai, N.; Matile, S., Photoproduction of proton gradients with π-stacked fluorophore scaffolds in lipid bilayers. *Science* **2006,** *313* (5783), 84-86.
102. Lieberman, K. R.; Cherf, G. M.; Doody, M. J.; Olasagasti, F.; Kolodji, Y.; Akeson, M., Processive replication of single DNA molecules in a nanopore catalyzed by phi29 DNA polymerase. *J. Am. Chem. Soc.* **2010,** *132* (50), 17961-17972.
103. Nivala, J.; Marks, D. B.; Akeson, M., Unfoldase-mediated protein translocation through an [alpha]-hemolysin nanopore. *Nat. Biotechnol.* **2013,** 31, 247-250.
104. Cockroft, S. L.; Chu, J.; Amorin, M.; Ghadiri, M. R., A single-molecule nanopore device detects DNA polymerase activity with single-nucleotide resolution. *J. Am. Chem. Soc.* **2008,** *130* (3), 818-820.
105. Chu, J.; González-López, M.; Cockroft, S. L.; Amorin, M.; Ghadiri, M. R., Real-time monitoring of DNA polymerase function and stepwise single-nucleotide DNA strand translocation through a protein nanopore. *Angew. Chem. Int. Ed.* **2010,** *49* (52), 10106-10109.
106. Franceschini, L.; Soskine, M.; Biesemans, A.; Maglia, G., A nanopore machine promotes the vectorial transport of DNA across membranes. *Nat. Commun.* **2013,** *4*.
107. Holden, M. A.; Needham, D.; Bayley, H., Functional bionetworks from nanoliter water droplets. *J. Am. Chem. Soc.* **2007,** *129* (27), 8650-8655.
108. Maglia, G.; Heron, A. J.; Hwang, W. L.; Holden, M. A.; Mikhailova, E.; Li, Q.; Cheley, S.; Bayley, H., Droplet networks with incorporated protein diodes show collective properties. *Nat. Nanotechnol.* **2009,** *4* (7), 437-440.
109. Villar, G.; Graham, A. D.; Bayley, H., A tissue-like printed material. *Science* **2013,** *340* (6128), 48-52.

Chapter Two

Solvent isotope effects on the nanoscale transport of DNA and ions

Abstract

Dynamic behaviour in solution at the length scale of molecular machines is dominated by Brownian motion and solvent viscosity. In the case of natural molecular machines, the solvent is ostensibly water, which is integral to the function of proteins; it solvates polar moieties and ions, and drives their self-assembly through the hydrophobic effect. Although translation of the macroscopic concept of viscosity to the molecular level is obscure, the effects of solvent dynamics on non-equilibrium molecular-level processes can be examined by the substitution of water (H_2O) with heavy water (D_2O), which has a higher viscosity than 'light water'. We have used transmembrane α-haemolysin pores as a model system to compare the effect of D_2O and H_2O on the translocation of single-stranded poly-dT DNA oligonucleotides 30, 60 and 90 bases long through nanoscale pores. The free channel ionic current through individual α-HL pores in H_2O was found to be ~21 % higher than in D_2O, while the rate of ssDNA translocation was found to be reduced in D_2O, which is suggested to result from the increased viscosity of D_2O and also differences in the extent of DNA interaction with the pore interior in D_2O.

The work in this chapter is being prepared for submission as a peer-reviewed article.

2.1 Introduction

Alpha-haemolysin (α-HL)[1] is a pore-forming toxin produced by *Staphylococcus aureus*. In biology the bacteria secretes the toxin in a monomeric form which self-assembles into a heptameric pore in the lipid bilayer surrounding target cells. This causes haemorrhaging of the cell's contents, irreversibly damaging the cell. In man-made systems α-HL nanopores have been used to investigate a wide range of processes at the single-molecule level including chemical reactions,[2]enzyme activity,[3] the analysis of nucleic acids,[4] kinetic isotope effects in reactions[5] and differences in protonation dynamics in D_2O versus H_2O.[6] In this chapter, α-HL (Figure 2.1) is used to investigate nanoscale modulation of solvent isotope effects on the non-equilibrium mechanical processes of electrokinetic ion and DNA transport. In subsequent chapters the protein will be used as a membrane spanning chassis in which to construct transmembrane molecular machines from synthetic DNA-PEG copolymers[7]

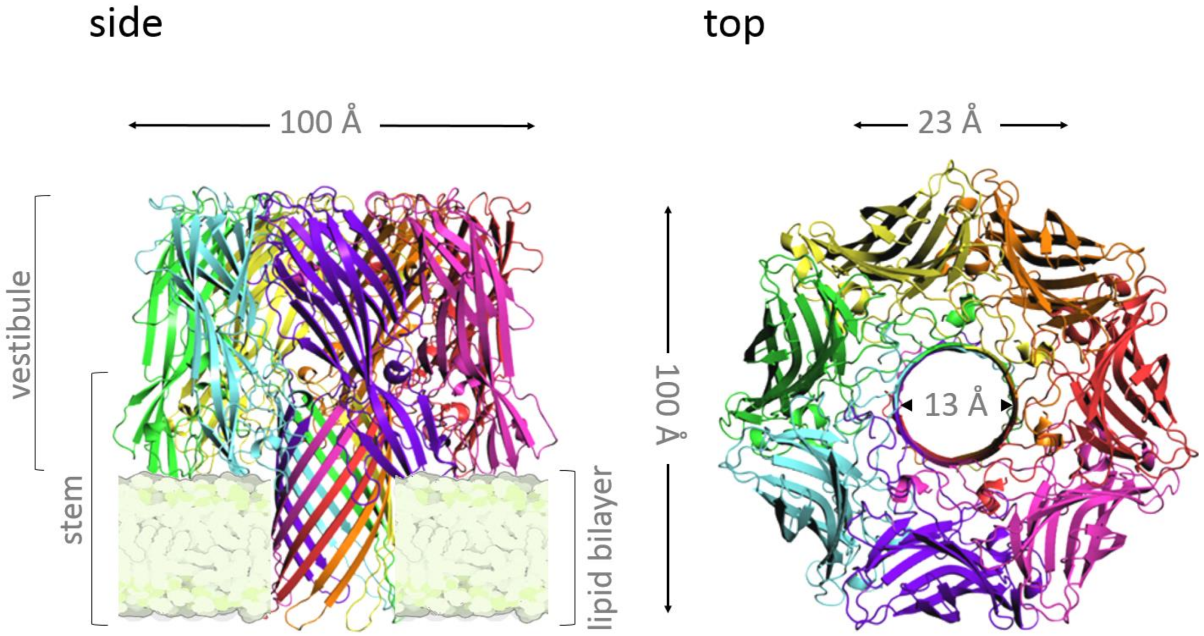

Figure 2.1 The alpha-haemolysin nanopore, the critical limiting aperture of the pore is large enough to permit the translocation of single-stranded DNA but not double-stranded DNA although the vestibule diameter can accommodate double-stranded DNA[1].

2.2 Isotope Effects

Elemental isotopes vary only in the number of neutrons contained within their nuclei. The existence of isotopes of hydrogen was implied by Bohr's theoretical description of the hydrogen atom[8] and later by studies of the band spectra of simple molecules in 1920 before the first isotopes were isolated and characterised by Urey et al[9,10]. Elemental hydrogen exists in three isotopic forms which have zero, one and two neutrons in their nuclei, respectively (protium, deuterium and tritium) (Figure 2.1a). The ratio of isotopes of an element is termed the relative abundance[11], and in the case of the isotopes of hydrogen, protium is by far the most abundant with a protium:deuterium ratio of ~5000:1. Isotopes have different nuclear properties, notably mass, and spin. Accordingly, different isotopes interact differently with electromagnetic fields, and this is the basis of their identification by spectroscopic techniques (and allows for example, the characterization of organic compounds by nuclear magnetic resonance (NMR) and the determination of the isotopic composition of stars). Many elements have now been shown to have multiple isotopes with different stabilities. The nuclei of certain isotopes are kinetically unstable and decay by radioactive emission in a first order process. Situations where these types of isotope effects are exploited include nuclear fusion with deuterium and tritium gas (D_2 and T_2 respectively) and radiocarbon dating using ^{14}carbon [12]. In molecules, bonds to heavier isotopes display different vibrational characteristics than their lighter analogues leading for example to increased fluorescence due to triplet extinction in pure ^{13}C-enriched fullerenes[13], another type of isotope effect.

Of most importance in biological and organic chemistry are deuterium substitution experiments to reveal kinetic details of enzymatic and chemical reactions[14,15]. Such kinetic isotope effects (KIEs) involve a change in the rate (k) of the determining step (R.D.S.) of a reaction such as R–H + X → R + H–X due to the isotopic substitution of an H atom for a D atom. The isotope effect is calculated from the ratio of the two rates (k_H/k_D)[16]. They are usually classified as either primary or secondary effects. A primary KIE (Figure 2.2) is observed when the bond broken or formed in the R.D.S. is to the substituted atom, whereas the KIE observed is secondary if the bond broken or formed does not involve the substituted atom but occurs at one or two bonds away. This difference in rate depends on the bond strength due to the rate of vibration of the bond. As deuterium has a larger rest mass than hydrogen the rate of vibration of the R–D bond is slower than in R–H and hence the amount of energy required to excite the vibration enough to break the bond is greater, this difference in energy is referred to as the difference in zero point energy (ΔZPE) and leads to $k_H > k_D$. However, the

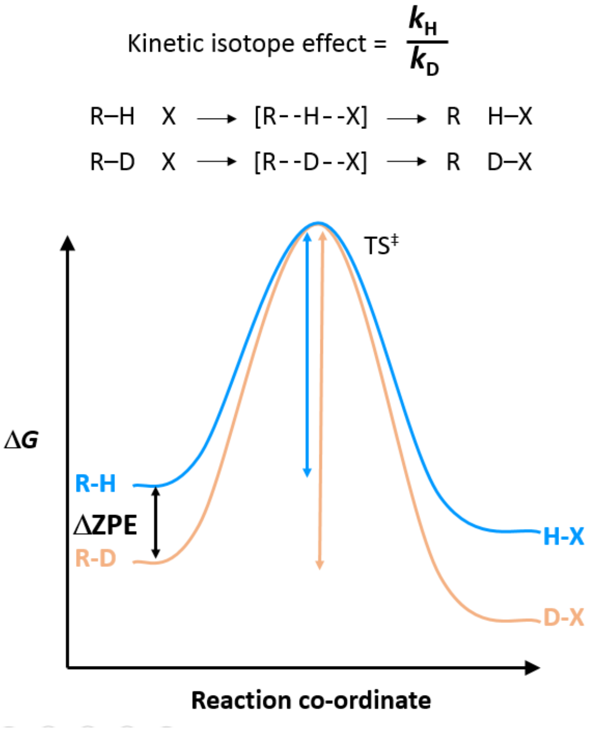

Figure 2.2 Basis of the primary kinetic isotope effect in an archetypal organic reaction

energy of the transition state is not tightly coupled to the ZPE as the partial bonds between the R, H/D and X groups are weak so $\Delta G^‡$ can be very small. In addition when kD > kH the value of k_H/k_D is smaller than one, this is referred to as an inverse KIE.

2.3 Deuterium solvent isotope effects in water

Solvent isotope effects are also sometimes observed in deuterated *vs*. non-deuterated solvents due to the large relative difference in mass of deuterium versus hydrogen (2:1). This is most evident in polar solvents where the intermolecular solvent-solvent interactions are most strongly affected by the substitution. Particularly pronounced isotope effects are observed in the case of D_2O vs. H_2O owing to the 100% difference in mass between D and H atoms and the significant proportion of the molecular volume occupied by the D or H atoms. Many investigations of the differences in the fundamental properties of the bonds have been carried out[17]. Some of the most pronounced differences in properties and behaviour are associated with the shorter length of the O-D bond as compared to the O-H bond and the corresponding greater length of the intermolecular ‘deuterium bond’ versus the hydrogen bond[18]. This leads to a greater degree of order in the bulk, hence D_2O is more ice-like than H_2O at higher temperatures due to it exhibiting a more ideally tetrahedral ‘deuterium bond’ network[18]. This difference in energy of the intermolecular bond network, which we shall call Δ_{network} has concomitant effects on the viscosity[19,20], D_2O is around 23 % more viscous than H_2O i.e. $k_H/k_D = 1.23$. The amount of free space in the bulk solvent and the polarity of the solvent and hence the ability to solubilise hydrophobic species[21] and ions[22] also differ for H_2O and D_2O. Nature’s molecular machines operate almost exclusively in water and it has been demonstrated that while enzymes function in heavy water there are notable isotope effects on their operation[23]. In the context of synthetic molecular machines based on protein and DNA, the solvent parameters that ought to have the largest effect on operation are the solubility of hydrophobic and polar groups[24], viscosity and hence the rates of transport through the fluid[25] thus isotopic effects relating to these parameters are of great interest. In addition, as it is known that interesting properties emerge at the nanoscale, it is not unreasonable to suggest that solvent isotope effects might be modulated in the confined nanoscale environment provided by the interior of the α-HL nanopore (Figure 2.3, right).

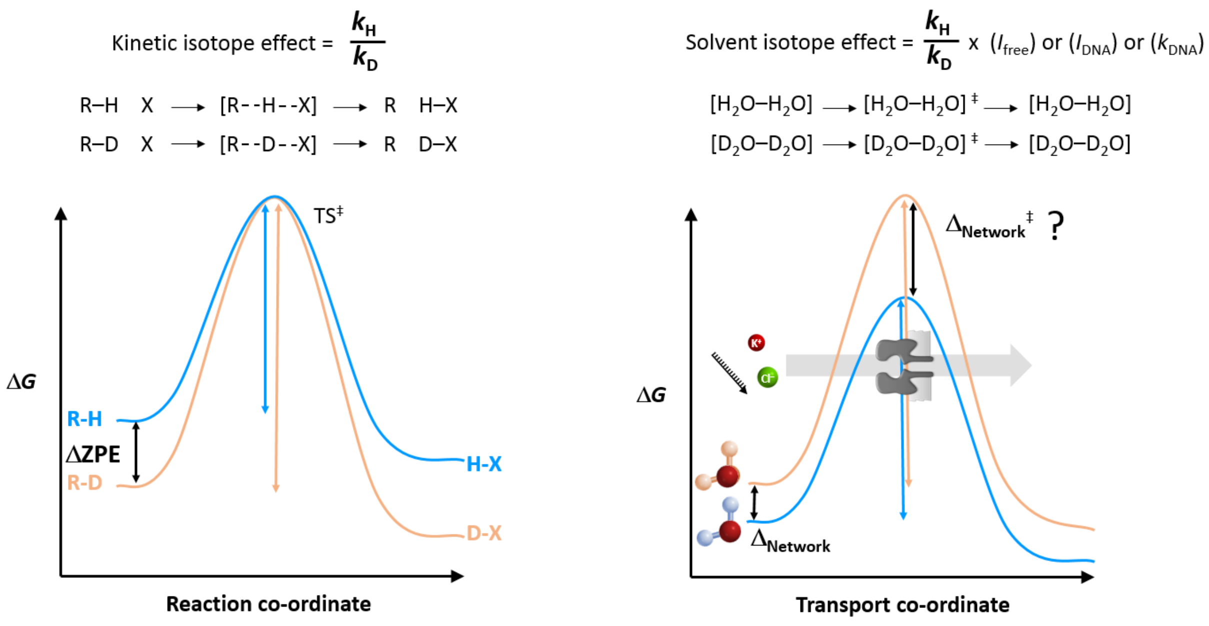

Figure 2.3 Comparison of the basis of the kinetic isotope effect on the rate of product formation of an archetypal organic reaction and the proposed origin of solvent isotope effects on the rates of transport through α-HL for monovalent ions or polyanionic DNA resulting from possible nanoscale modulation of Δ_{network}.

2.4 Solvent isotope effects in α-HL- insertion into lipid bilayers

As described in section 2.1 α-haemolysin (α-HL) has arisen as a popular protein scaffold for use as a detection element in single molecule biophysics[26]. The main reason for this is the ease with which it reproducibly forms transmembrane pores in lipid bilayers which are then stable enough to allow electronic diagnostic readout of processes affecting the flow of ions through them. The process of channel formation is believed to occur as a result of hydrophobic effects whereby monomers of the toxin diffuse in aqueous solution and then partition into the membrane in a manner which causes a conformational change, with the helix moving to penetrate the bilayer in a concerted manner as a result of interactions with other monomers, evidence for this concerted screw-like penetration coupled to oligomerisation comes from a study on the related aerolysin protein[27]. Usually seven monomers form each α-HL pore and the pore is oriented *cis*/*trans* with respect to the side of the bilayer from which the monomers arrived and the barrel of the pore is unobstructed.

However sometimes a channel will misfold for one reason or another, possibly due to a kinetic trap in an alternative folding pathway higher but similar in energy to the normal for the oligomerisation involving only six monomers[28], or a similar but higher energy oligomerization process might cause the channel to be inserted *trans*/*cis* or to be noisy with respect to current flow. The correct folding, partitioning, oligomerisation and penetration behaviour required to form a stable channel could result from the interplay of many factors such as the solubilities of the different parts of the protein in water versus lipid. D_2O has a different p*K*a from H_2O and can solubilise hydrophobic groups differently [29], indeed the behaviour of various proteins[30], [31], [32] and lipid vesicles[33] has been shown to be different in D_2O as compared to H_2O. Therefore, it was reasoned that there may be differences in the channel insertion behaviour in D_2O versus H_2O. Although a full investigative dissection of these differences is beyond the scope of the present work, a simple experiment was carried out to compare the ease of correct channel insertion in each solvent. All nanopore experiments I nthe present chapter were set up using 25 mM Tris HCl buffered 1 M KCl solution in either H_2O or D_2O and adjusted to pH 8 and pD 7.49 respectively to account for the different specific activity of H^+ and D^+[34], detailed experimental procedure for obtaining a lipid bilayer and an individual channel is provided in the materials and methods section at the end of the chapter. In this experiment the object was to observe multiple sequential insertions of α-HL. Thus, the protein was added to the ground well to a high final concentration of ~700 nM and a potential of +100 mV was applied with respect to the grounded electrode. A correctly formed lipid bilayer acts as a capacitor and does not allow the passage of ions The number of channels observed to insert over a brief period was then monitored by stepped increases in the transmembrane ion current (Figure 2.4). Generally the rate of correct insertion is higher in H_2O than in D_2O, seven out of seven insertions were correct in H_2O and only one out of four in D_2O, the remaining three insertion in D_2O are believed to be wrongly oriented. It should be noted that this may be a reflection of the differences in diffusion rate through the solvent rather than an indication of a higher barrier to insertion in D_2O than H_2O. However, while this was an isolated experiment, this behaviour was borne out in further experiments where the aim was to obtain a single channel; channels were more often wrongly oriented, very small or noisy in D_2O buffer than H_2O

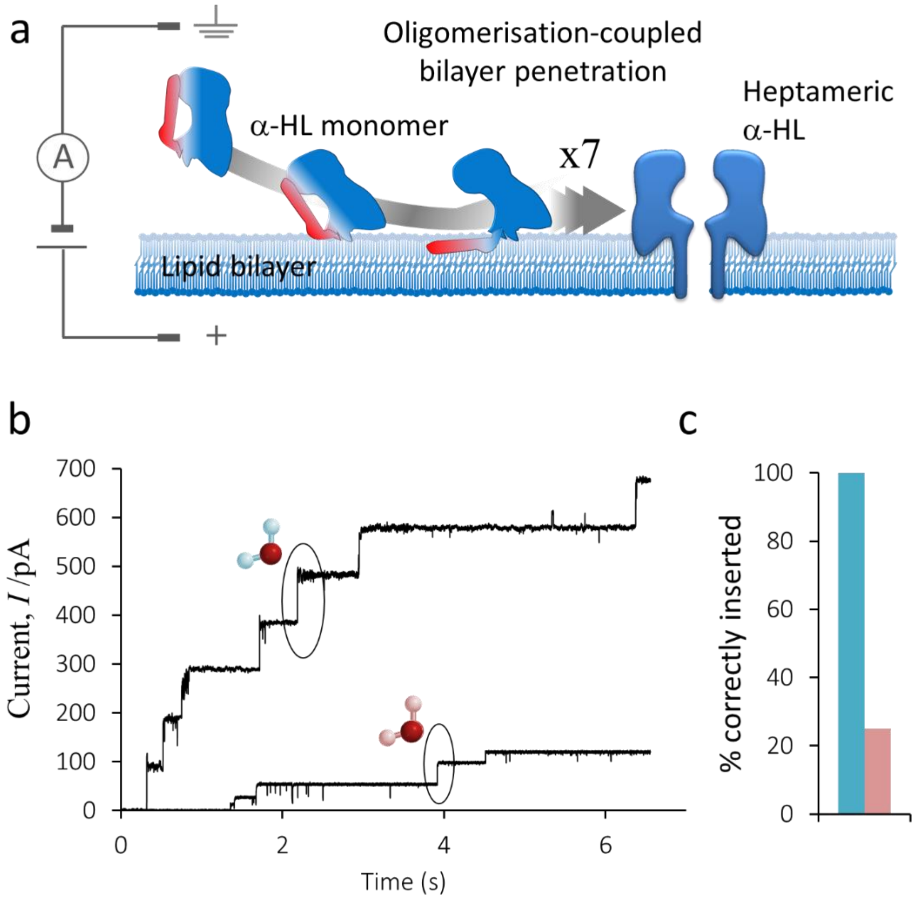

Figure 2.4 proposed mechanism of insertion of α-HL into lipid bilayers and the effect of D_2O on this process. **a** commonly presumed model of channel insertion to a lipid bilayer, individual monomers diffuse to and oligomerise in the bilayer, the 7 β-sheet parts (indicated in red) co-penetrate the bilayer perhaps as a result of co-operative transannulations between the β-sheets of each monomer. **b** real-time current changes corresponding to insertions of α-HL in H_2O and D_2O buffers, the circled steps indicate correctly oriented and sized channels.
c percentage of channels correctly inserted,

2.5 Electrokinetic transport of ions through single α-HL pores

Kasianowicz[35] et al have previously examined the effect of H_2O versus D_2O on the protonation of the α-HL pore, while Bayley et al have investigated a primary kinetic isotope effect in Michael addition reactions occurring on single molecules tethered inside mutant α-HL channels[36] and strategies such as changing solvent viscosity[37] to modulate the translocation of DNA through nanopores have been examined for potential applications in nanopore-based DNA sequencing.. However, to date no-one has examined the effects of isotopic substitution of the solvent on the translocation of analytes through the pore channel.

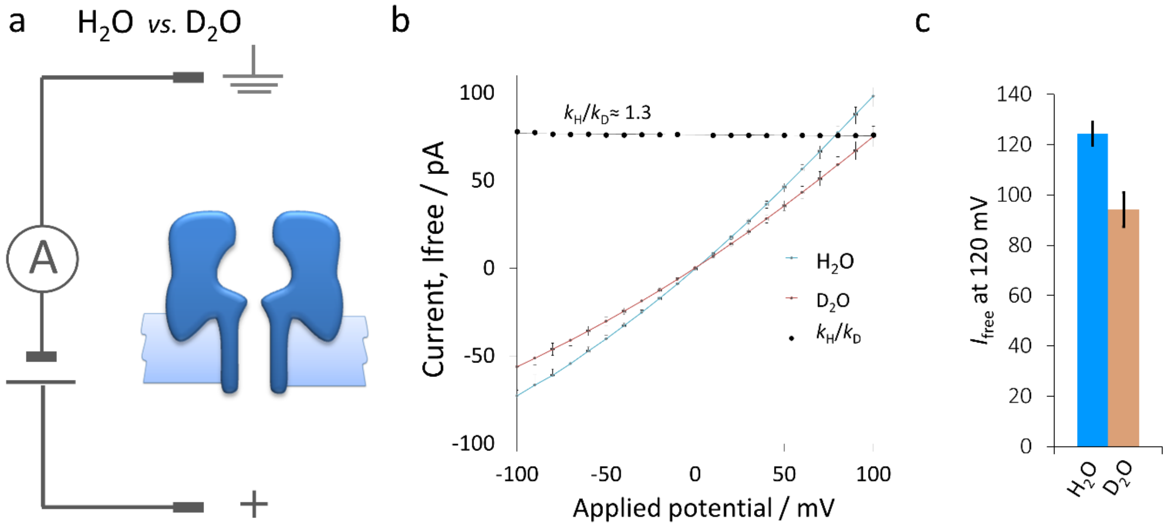

Figure 2.5 Current response of α-HL channels in H_2O and D_2O. **a** Individual α-HL inserted in a lipid bilayer. **b** Average *I*/*V* sweeps of individual channels in H_2O and D_2O at 1 M KCl. **b** average current response was calculated from 1.5 seconds of real time current recordings measured at 10 mV intervals across an applied potential range of 100 to –100 mV for 10 individual correctly folded channels in H_2O or D_2O buffer. The solid lines represent the average current at each potential in each condition, error bars represent the standard deviation. **c** Average free channel current response at 120 mV for the 38 channels used in the main study (16 in H_2O and 22 in D_2O) error bars represent the standard deviations of the mean in each case.

Here, individual α-haemolysin (α-HL) channels inserted in bilayer membranes (BLM) were used as a simple platform to compare the translocation of ions in H_2O versus D_2O under a range of experimental conditions. The differences in electrokinetic ion transport through individual correctly inserted pores was characterised using the set up in Figure 2.5. A stepped voltage protocol was used to determine the characteristics of ion transport through individual α-HL pores in 25 mM Tris HCl buffered 1 M KCl solution in either H_2O or D_2O and adjusted to pH 8 and pD 7.49 respectively as before. Transmembrane potentials were applied in two second sweeps in increments of 10 mV from –100 to +100 mV. Ten *I*/*V* sweeps were carried out and averaged for each of six and seven individual correctly oriented and folded channels in H_2O and D_2O respectively (Figure 2.5).

The total average current response is shown by the solid coloured lines, error bars represent the standard deviation of the sample. The shallow deviation of the *I/V* trace from linearity, particularly at negative potentials is due to the slight rectification behaviour of the channels. The average conductance of a single α-HL (I_{free}) in H_2O buffer across the entire 200 mV applied potential range was found to be ~30 % higher than in D_2O buffer i.e. $k_H/k_D = 1.3 \pm 0.1$. Within the nanopore, the solvent isotope effect is enhanced with respect to the bulk conductance of K^+ and Cl^- in bulk solutions of H_2O *vs*. D_2O[25] ($k_H/k_D = 1.21$). The general observed reduction in ionic flux is likely due to the different viscosity of H_2O and D_2O which is then further modulated by confinement within the pore.

2.6 Translocation of homopolymeric ssDNA oligonucleotides

Many studies have sought to develop α-HL platforms for use as a next generation DNA sequencing technology. The original proposal of single-molecule nanopore sequencing was that each of the four bases might impede the flow of current through the pore by a characteristic amount as a single strand of DNA is driven through the pore by an applied electric field[38]. The potential advantages of this approach are low cost, ease of use and the prospect of effectively infinite read lengths.

However, the rate of translocation of DNA through the wild-type pore is too rapid to obtain a high enough signal-to-noise-ratio (SNR) to achieve a sequencing device of sufficient accuracy. Some attempts to overcome this limitation have involved slowing the translocation of the DNA through the pore, notably by the use of molecular brakes[39], the use of DNA processing enzyme to ratchet the bases of the strand through the pore individually[40], or more simply by changing the properties of the solvent such as pH[41] or viscosity via the addition of glycerol[37] or organic salts[42]. In the case of the glycerol study, the increase in viscosity was shown to slow translocation of ssDNA but the ionic conductance was also greatly reduced giving a poor signal to noise ratio.

Given the known increased viscosity of D_2O *cf.* H_2O, it was decided to investigate the extent of any solvent isotope effects on the translocation of single-stranded DNA (ssDNA)

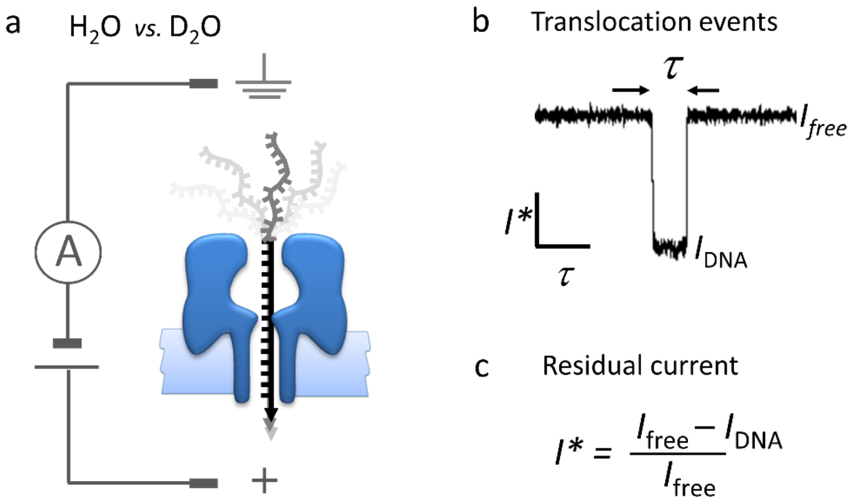

Figure 2.6 Cartoon and typical raw data of ssDNA translocating α-HL. **a** ssDNA being driven through an α-HL channel by an applied potential of +120 mV. **b** Representative current data generated from the translocation of ssDNA **c** calculated residual current, I^*

through α-HL pores. Thereby, it would also be possible to assess the potential of D_2O as a relatively low cost additive to reduce translocation rates while retaining conductivity and hence signal-to-noise ratio.

After obtaining a correctly inserted channel in either H_2O or D_2O, homopolymeric polyT DNA with a length of either 30, 60 or 90 nucleotides, was added to the grounded well of the experimental cell (Figure 2.6a). A potential of +120 mV was applied and the current recorded. DNA events were revealed as transient blocks in the current (Figure 2.6b). In total 16 channels were investigated in H_2O and 22 in D_2O. As the DNA enters the pore it blocks the flow of small ions through the pore, the duration of the blocked state τ and the magnitude of the blockade current I^* are then recorded (Figure 2.6c). When analysed in a scatterplot (Figure 2.7) the events fall into clusters (circled) suggesting three types of event. The event types are attributed to vestibule events in which DNA enters the pore but then escapes without translocating ($I^* \sim 0.65$) or to translocation events in which either the 5' or 3' end enters the pore first. During translocation a strand must pass through the narrowest constriction of the pore and hence occlude the current to a large extent ($I^* < 0.5$) of the value for a free channel. Two main clusters of event are clearly visible within that range, which have been attributed to the strand entering by their 5' or 3' ends and fully translocating the pore. This was demonstrated to be true by Mathé et al who compared the distribution of current blockades for simple homopolymer translocation events to those of simple DNA hairpins with leading 3' or 5' ends respectively[43].

In the present work, in order to build up a statistically significant dataset, recordings came from at least five channels (n 5) for each oligonucleotide length in each buffer and further analyses were performed on the summed total number of events in each experimental condition as shown in Figure 2.7, the scatterplots obtained from each individual experiment are given in the materials and methods section. In the case of 90mer polyT in D_2O buffer the number of events recorded for a given channel was not always high before the insertion of a second or of multiple channels, hence more single channel experiments were performed until the total number of events recorded for each oligo length, were about the same (N>5000). Visual comparison of the scatterplots suggests differences in the relative populations of each class of event across channels in the same buffer this may suggest that subtle differences exist in conformations of the channels in both H_2O and D_2O and reflects the stochastic nature of the technique.

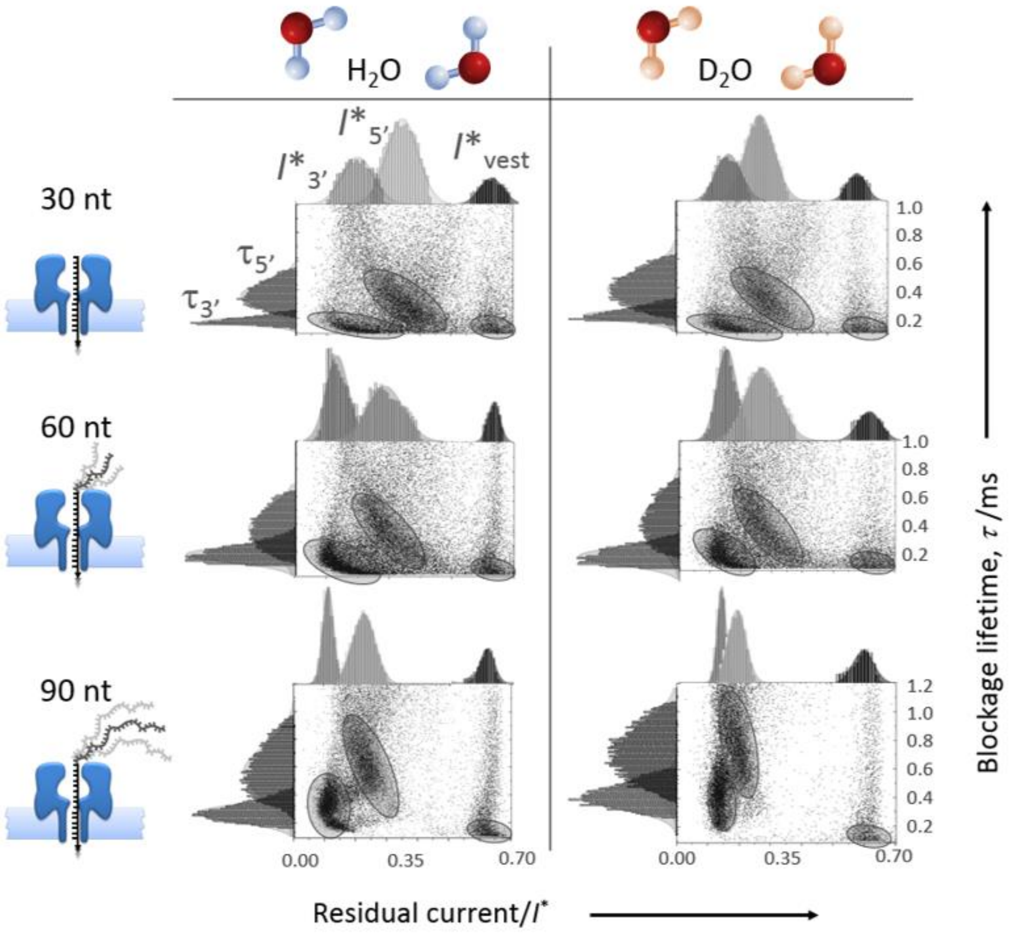

Figure 2.7 Raw data for DNA – α-HL interaction events. Event scatter plots for each oligo length in each buffer. The highlighted elliptical regions of interest from the composite scatterplot of all the channels for each condition investigated correspond to translocation events only.

The shortest oligonucleotide scatterplots exhibit a smear of I^* values from the vestibule events to translocations, but as the length of the oligonucleotides increase, the vestibule and translocation events become more clearly defined. This could be explained by the greater effect of the electric field on longer oligos than shorter ones, meaning that the extent to which a short oligo can enter the pore and occlude ion flow but still escape is greater than for longer strands which will be irreversibly captured more readily if they enter the vestibule and hence translocate.

It is clear from visual inspection that both the magnitude and range of event durations increase proportionally with oligo length. In contrast, increasing the length of the oligonucleotides decreases the value, and decreases the range of current blockage events.

Translocation events in which the 3’ end threads through the pore first usually take longer in all cases than 5’ first translocations, presumably due to the polarity of the strand - one orientation providing more resistance than the other. The 5’ translocations also obstruct the current more than the 3’ events. The I^* discrimination between 5’ and 3’ translocations is poorer in D_2O than H_2O, which may be due to differences in solvation of both the DNA bases and internal residues of the pore. The translocation duration increases with strand length in both H_2O and D_2O, as would be expected. To determine the magnitude of any solvent isotope effects on translocation in D_2O versus H_2O, the extracted durations were rendered as histograms and fitted to single Gaussian distributions (Figure 2.7). The peaks of the fitted data were then taken as the representative values of event duration for each oligo length in each buffer. The rate of translocation was then calculated for translocations (k_{DNA}). The translocation rate per second is dependent on a number of factors and explanations for this have been provided elsewhere[44]. Briefly, this occurs as a result of the different environmental regimes to which the strand is exposed, that is, in the pore and in the bulk, while it interacts with the potential gradient. Below a certain length the ends of the strand have decreased degrees of freedom, they are not interacting with the bulk solvent while the strand is in the pore and are simultaneously able to interact with the sides of the pore increasing the variability in the exact route of the strand through the pore and hence the average translocation rate per base is low, but as the total number of bases is also low the total translocation duration is low. As the length increases the ends of the strand’s degrees of freedom increase and during translocation they are not both able to interact with the pore at the same time so the exact route of the strand through the pore is less variable and hence the average translocation rate increases, also the strand is almost completely isolated from the bulk solvent during translocation so the effect of the solvent is still minimal. As the length

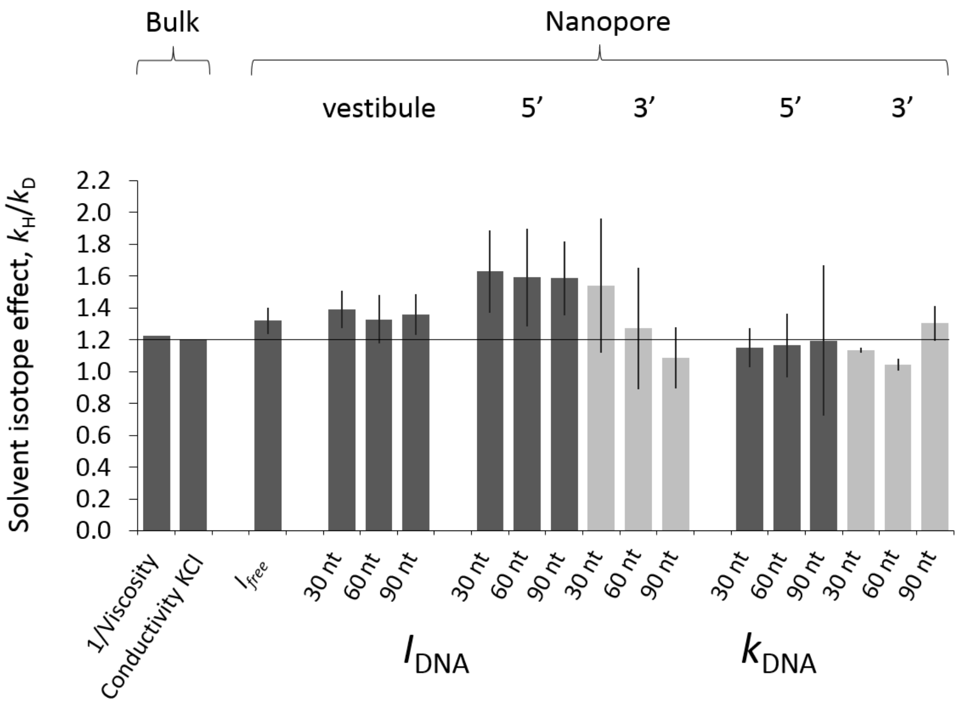

Figure 2.8 Solvent isotope effects k_H/k_D in the nanopore and equivalent properties in bulk solution. Error bars are derived from the distributions of the single molecule values of I^* and τ.

further increases the strand's ends are both exposed to the bulk solvent during translocation and there is a relatively very narrow distribution of routes through the pore experienced by each base. Thus, the bulk-exposed regime dominates and as there is an energy penalty for desolvation as the strand enters the pore the rate of translocation per base becomes inversely proportional to oligo length (although a plateau is likely reached at some point). This behaviour appears to remain true in D_2O, with the translocation duration initially decreasing then increasing with oligo length while the solvent isotope effect is smallest for the intermediate strand length which is also in agreement with theory. The length dependence of k_H/k_D values for k_{DNA} was not immediately easy to explain.

Ionic current can be defined as charge per second. Hence, the currents through the pore calculated from the product of I_{free} and I^* for each condition are also rates (I_{DNA}) which can be compared to give values of k_H/k_D. The isotope effect data gathered in the present work and in previous literature across a range of parameters each have different units and to permit intuitive comparison over all the parameters k_H/k_D is a convenient normalisation. This yields values that can then be plotted as a bar chart which expresses the relative solvent isotope effects on each parameter. The large solvent isotope effect on ion transport through α-HL can be related to the difference in ionic conductance in bulk D_2O and H_2O[25] and different nanoscale modulation of the ion current arising from blockage by strands of different lengths while the differences in translocation duration for single-stranded polyT DNA can be related to the differences in the bulk viscosity.

2.7 Conclusions and future work

The modulation of solvent isotope effects on the nanoscale was investigated using individual α-HL nanopores as a first step in investigating factors that may affect the operational behaviour of putative synthetic transmembrane machines. The approach complements existing solution-phase measurements of the differences in both the fundamental behaviour of bulk H_2O and D_2O and species solvated in them. The electrokinetic transport of both monovalent ions and ssDNA were found to exhibit solvent isotope effects in response to substitution of hydrogen with deuterium in water. Subtle differences in the ability of the pore to discriminate the orientation of translocating strands were observed between D_2O and H_2O which may suggest that there is a greater degree of non-specific interaction between DNA and the interior of the pore when reconstituted with D_2O than H_2O. The potential for using D_2O in place of H_2O in order to slow the rate of strand translocation and hence facilitate next-generation DNA sequencing was also considered, although the range of strand lengths investigated was too narrow to establish the potential impact of this substitution. This approach could be developed to examine different bases also longer and heteropolymeric strands could be tested to better explore the trends suggested by the present work. In addition, the complexity of the systems being investigated could be greatly increased, in particular molecular machines based on α-HL and DNA in which the DNA is constantly engaged at the pore (rotaxanated) could be constructed to allow finer dissection of the solvent parameters impingent within the pore and to determine the solvent isotope effects on such molecular machine assemblies. Such studies are currently planned in our lab using some of the transmembrane molecular machine architectures developed in the subsequent chapters of the present work.

2.8 Materials and Methods

M2.1 Patch Clamp Experiments

Nanopore experiments were performed in a custom built cell, composed of two teflon blocks each with a machine-drilled well ~1 mL in volume which were bolted together (Figure M1). Each well contained a side opening such that when the blocks are clamped together the wells are connected through their side openings. A 25 µm thick Teflon sheet (Goodfellow) was clamped between the two blocks, separating the side openings and fixed in place with silicone glue (3140 RTV coating, Dow Corning). A Teflon sheet containing an aperture of ~100 µm diameter (produced with a 30 kV spark gap generator) was positioned such that the aperture was in the centre of the lower half of the inter-well channel. The cell was placed on a Nano 20/30 anti-vibration platform (Halcyonics) within a custom built faraday cage with acoustic damping to isolate the experiment from external electrical and mechanical noise. A small hanging drop (~5 µL) of 10% solution of hexadecane in *n*-pentane was touched on each side of the Teflon sheet. 600 µL of a solution containing KCl (Sigma) (1 M) and Tris –HCl or DCl (25 mM) buffered to pH 8.0 or pD 7.6 in H_2O (Greiner Bio) or D_2O (Sigma) respectively was added to the well on each side of the Teflon sheet. 6 µL of 10 mg/mL solution of 1,2-diphytanoyl-*sn*-glycero-3-phosphocholine (Avanti Polar Lipids) in *n*-pentane (Sigma) was dispensed using a syringe on each side of the Teflon sheet. The buffer solution was then aspirated and dispensed into each well multiple times using a Hamilton syringe to paint a phospholipid bilyer across the aperture. Ag/AgCl electrodes (Warner) connected to a patch clamp amplifier (Axopatch 200B, Molecular Devices) were placed on either side of the Teflon sheet and a ±1 mV pulse applied at 1333 Hz to determine when a bilayer was obtained (capacitance of 60-80 pF). A gel loading tip fitted to a 20 µL Gilson type pipettor was introduced into an aqueous solution of α-haemolysin (Sigma Aldrich, ~250 µM), without aspirating, such that a tiny amount << 1 µL of the solution remained on the tip. The pipette tip was then submerged ~5 mm from the aperture in the Teflon sheet and repeatedly aspirated. The process was repeated until a small current corresponding to a single channel arose.

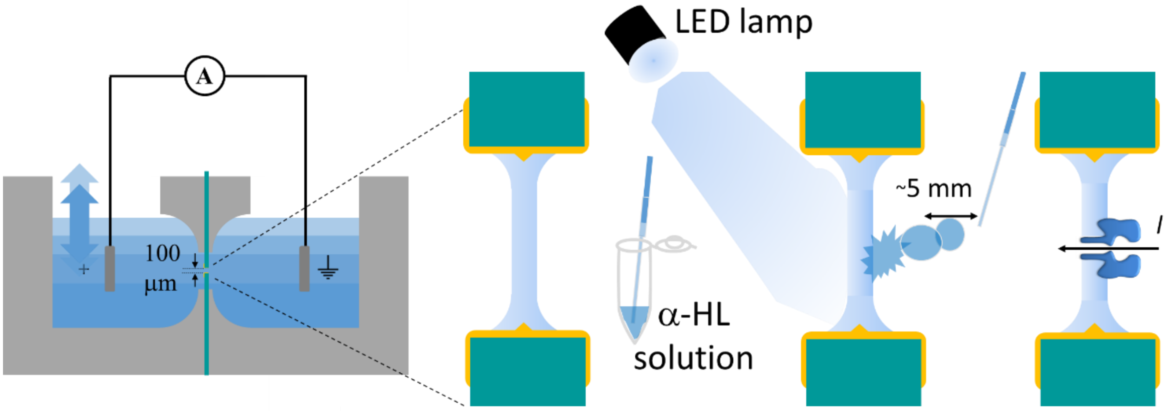

Figure M2.1. Experimental set-up used for single-channel recordings.

M2.2 DNA Experiments

DNA experiments were performed at 21 ±2 °C. DNA (5 µL, 300 µM) was added to the ground well of the experimental cell shown in Figure S1 (and described above). A 120 mV transmembrane voltage was applied, and data were recorded using an Axon Axopatch 200B (Molecular Devices) equipped with a CV203BU headstage (Molecular Devices), and digitized using an Axon Instruments Digidata 1332A at a sample rate of 50 kHz. Single-channel ion current recordings were processed with Clampex 10.2 and Clampfit 10.2 software. Examples of characteristic DNA events are shown in Figure M2.2. Ion current traces were digitally filtered at 10 kHz. Events were extracted using the threshold search function in Clampfit 10.2 and then processed using Origin 9 Pro and Microsoft Excel 2010. The events analysed for each channel are shown in figure M2.3. Events longer than 1.5 ms were excluded from the analysis as these types of events are attributed to gating events.

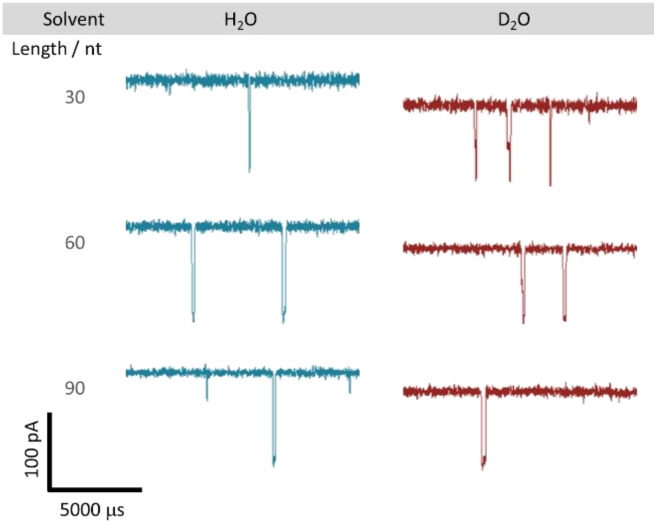

Figure M2.2 Representative real-time DNA event data in D_2O and H_2O buffers.

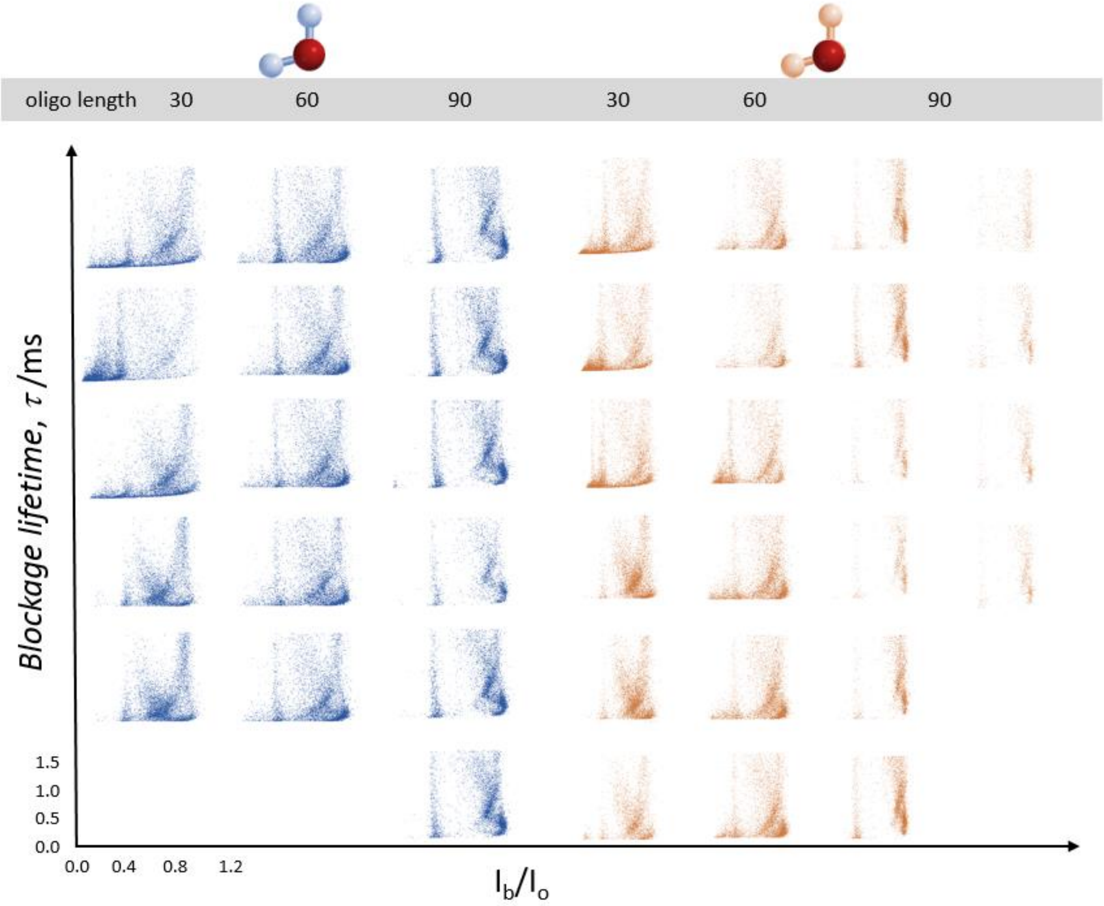

Figure M2.3 Scatterplots obtained from individual single channels

M2.3 DNA Synthesis, Purification and Storage

Poly dT 30, 60 and 90mers were synthesized on a MerMade 4 solid-phase DNA synthesizer (Bioautomation) using phosphoramidites and coupling reagents (Link Technologies) for standard 3’ to 5’ DNA synthesis according to the manufacturer’s instructions and purified by two-stage (DMT-on and DMT-off) reverse-phase HPLC using a C-18 semi-preparative column (Supelco) with an acetonitrile (mobile phase B) / 100 mM triethylammonium acetate in 5:95, acetonitrile : water pH 7 (Mobile phase A) gradient buffer system at a flow rate of 7 mL/min. A column temperature of 65 °C was used to minimize secondary structure (which could complicate retention behaviour) and elution of DNA fractions was monitored by an integrated UV/vis spectrometer at 260 nm on a Dionex ultimate 3000 series HPLC running Chromeleon software. DMT-on oligos were purified using a gradient of acetonitrile (mobile phase B), 13 to 25 % over 15 minutes. UV absorbance traces were monitored at 260 nm and the oligonucleotide-containing fractions were collected manually. In each case. the desired fraction was combined detritylated with 20% AcOH (v/v) at room temp for one hour before being HPLC purified a second time using a shallower gradient of mobile phase B (0 to 12 % over 15 minutes). The final DMT-off HPLC chromatograms for the synthesised strands are shown in Figure M4. Fractions were collected manually to ensure the avoidance of shoulder peaks. The DNA was concentrated at reduced pressure to ~300 µM and stored in aliquots of 5 µL in PCR tubes in press-sealed plastic bags at –20 °C.

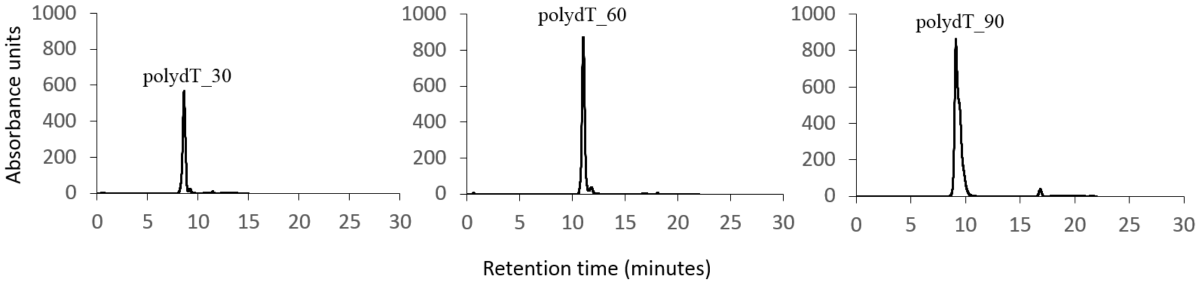

Figure M2.4 HPLC chromatograms (absorbance at 260 nm) obtained for synthesized and purified DNA.

2.9 References

1. Song, L.; Hobaugh, M. R.; Shustak, C.; Cheley, S.; Bayley, H.; Gouaux, J. E., Structure of staphylococcal α-hemolysin, a heptameric transmembrane pore. *Science* **1996,** *274* (5294), 1859-1865.
2. Wu, H.-C.; Bayley, H., Single-molecule detection of nitrogen mustards by covalent reaction within a protein nanopore. *J. Am. Chem. Soc.* **2008,** *130* (21), 6813-6819.
3. Cockroft, S. L.; Chu, J.; Amorin, M.; Ghadiri, M. R., A single-molecule nanopore device detects DNA polymerase activity with single-nucleotide resolution. *J. Am. Chem. Soc.* **2008,** *130* (3), 818-820.
4. Wanunu, M., Nanopores: A journey towards DNA sequencing. *Phys. Life Rev.* **2012,** *9* (2), 125-158.
5. Shin, S.-H.; Luchian, T.; Cheley, S.; Braha, O.; Bayley, H., Kinetics of a reversible covalent-bond-forming reaction observed at the single-molecule level. *Angew. Chem.* **2002,** *114* (19), 3859-3861.
6. Kasianowicz, J. J.; Bezrukov, S. M., Protonation dynamics of the alpha-toxin ion channel from spectral analysis of pH-dependent current fluctuations. *Biophys. J.* **1995,** *69* (1), 94-105.
7. Chu, J.; González-López, M.; Cockroft, S. L.; Amorin, M.; Ghadiri, M. R., Real-time monitoring of DNA polymerase function and stepwise single-nucleotide DNA strand translocation through a protein nanopore. *Angew. Chem. Int. Ed.* **2010,** *49* (52), 10106-10109.
8. Bohr, N., On the constitution of atoms and molecules. *Philosoph. Mag.* **1913,** *Series 6 volume 26,* 1-25.
9. Urey, H. C.; Bradley, C. A., Jr., On the relative abundances of isotopes. *Phys. Rev.* **1931,** *38* (4), 718-724.
10. Urey, H. C.; Brickwedde, F. G.; Murphy, G. M., A hydrogen isotope of mass 2 and its concentration. *Phys. Rev.* **1932,** *40* (1), 1-15.
11. Bleakney, W.; Gould, A. J., The relative abundance of hydrogen isotopes. *Phys. Rev.* **1933,** *44* (4), 265-268.
12. W.F., L., The physical science of radiocarbon dating. In *Sci. meth. mediev. arch.*, 1870; pp 17-21.
13. Baleizão, C.; Berberan-Santos, M. N., The brightest fullerene: a new isotope effect in molecular fluorescence and phosphorescence. *ChemPhysChem* **2011,** *12* (7), 1247-1250.
14. (a) Kohen, A.; Roston, D.; Stojković, V.; Wang, Z., Kinetic isotope effects in enzymes. In *"Kinetic Isotope Effects in Enzymes" in Encyclopedia of Analytical Chemistry*, John Wiley & Sons, Ltd: 2006; (b) Dahlquist, F. W.; Rand-Meir, T.; Raftery, M. A., Application of secondary .alpha.-deuterium kinetic isotope effects to studies of enzyme catalysis. Glycoside hydrolysis by lysozyme and .beta.-glucosidase. *Biochemistry* **1969,** *8* (10), 4214-4221.
15. Lisal, J.; Lam, T. T.; Kainov, D. E.; Emmett, M. R.; Marshall, A. G.; Tuma, R., Functional visualization of viral molecular motor by hydrogen-deuterium exchange reveals transient states. *Nat. Struct. Mol. Biol.* **2005,** *12* (5), 460-466.
16. Westheimer, F. H., The magnitude of the primary kinetic isotope effect for compounds of hydrogen and deuterium. *Chem. Rev.* **1961,** *61* (3), 265-273.
17. Scheiner, S.; Čuma, M., Relative stability of hydrogen and deuterium bonds. *J. Am. Chem. Soc.* **1996,** *118* (6), 1511-1521.
18. Soper, A. K.; Benmore, C. J., Quantum differences between heavy and light water. *Phys. Rev. Lett.* **2008,** *101* (6), 065502.
19. Harris, K. R.; Woolf, L. A., Temperature and volume dependence of the viscosity of water and heavy water at low temperatures. *J. Chem. Eng. Dat.* **2004,** *49* (4), 1064-1069.
20. Cho, C. H.; Urquidi, J.; Singh, S.; Robinson, G. W., Thermal offset viscosities of liquid H_2O, D_2O, and T2O. *J. Phys. Chem. B* **1999,** *103* (11), 1991-1994.
21. Kresheck, G. C.; Schneider, H.; Scheraga, H. A., The effect of D_2O on the thermal stability of proteins. thermodynamic parameters for the transfer of model compounds from H_2O to D_2O 1,2. *J. Phys. Chem.* **1965,** *69* (9), 3132-3144.
22. Krishnan, C. V.; Friedman, H. L., Solvation enthalpies of various ions in water and heavy water. *J. Phys. Chem.* **1970,** *74* (11), 2356-2362.
23. Panda, D.; Chakrabarti, G.; Hudson, J.; Pigg, K.; Miller, H. P.; Wilson, L.; Himes, R. H., Suppression of microtubule dynamic instability and treadmilling by deuterium oxide†. *Biochemistry* **2000,** *39* (17), 5075-5081.
24. Parker, M. J.; Clarke, A. R., Amide backbone and water-related H/D isotope effects on the dynamics of a protein folding reaction. *Biochemistry* **1997,** *36* (19), 5786-5794.
25. Swain, C. G.; Evans, D. F., Conductance of ions in light and heavy water at 25°. *J. Am. Chem. Soc.* **1966,** *88* (3), 383-390.
26. Ma, L.; Cockroft, S. L., Biological nanopores for single-molecule biophysics. *ChemBioChem* **2010,** *11* (1), 25-34.

27. Degiacomi, M. T.; Iacovache, I.; Pernot, L.; Chami, M.; Kudryashev, M.; Stahlberg, H.; van der Goot, F. G.; Dal Peraro, M., Molecular assembly of the aerolysin pore reveals a swirling membrane-insertion mechanism. *Nat. Chem. Biol.* **2013,** *9* (10), 623-629.
28. Czajkowsky, D. M.; Sheng, S.; Shao, Z., Staphylococcal α-hemolysin can form hexamers in phospholipid bilayers. *J. Mol. Biol.* **1998,** *276* (2), 325-330.
29. Graziano, G., Relationship between cohesive energy density and hydrophobicity. *The Journal of Chemical Physics* **2004,** *121* (4), 1878-1882.
30. Cioni, P.; Strambini, G. B., Effect of heavy water on protein flexibility. *Biophys. J.* **2002,** *82* (6), 3246-3253.
31. Makhatadze, G. I.; Clore, G. M.; Gronenborn, A. M., Solvent isotope effect and protein stability. *Nat. Struct. Mol. Biol.* **1995,** *2* (10), 852-855.
32. Connelly, P. R.; Thomson, J. A.; Fitzgibbon, M. J.; Bruzzese, F. J., Probing hydration contributions to the thermodynamics of ligand binding by proteins. Enthalpy and heat capacity changes of tacrolimus and rapamycin binding to FK506 binding protein in deuterium oxide and water. *Biochemistry* **1993,** *32* (21), 5583-5590.
33. Viitanen, P.; Garcia, M. L.; Foster, D. L.; Kaczorowski, G. J.; Kaback, H. R., Mechanism of lactose translocation in proteoliposomes reconstituted with lac carrier protein purified from Escherichia coli. II. deuterium solvent isotope effects. *Biochemistry* **1983,** *22* (10), 2531-2536.
34. Covington, A. K.; Paabo, M.; Robinson, R. A.; Bates, R. G., Use of the glass electrode in deuterium oxide and the relation between the standardized pD (paD) scale and the operational pH in heavy water. *Anal. Chem.* **1968,** *40* (4), 700-706.
35. Kasianowicz, J. J.; Bezrukov, S. M., Protonation dynamics of the alpha-toxin ion channel from spectral analysis of pH-dependent current fluctuations. *Biophysical Journal* **1995,** *69* (1), 94-105.
36. Lu, S.; Li, W.-W.; Rotem, D.; Mikhailova, E.; Bayley, H., A primary hydrogen–deuterium isotope effect observed at the single-molecule level. *Nat. Chem.* **2010,** *2* (11), 921-928.
37. Kawano, R.; Schibel, A. E. P.; Cauley, C.; White, H. S., Controlling the translocation of single-stranded DNA through α-hemolysin ion channels using viscosity. *Langmuir* **2009,** *25* (2), 1233-1237.
38. Kasianowicz, J. J.; Brandin, E.; Branton, D.; Deamer, D. W., Characterization of individual polynucleotide molecules using a membrane channel. *Proc. Natl. Acad. Sci. USA* **1996,** *93* (24), 13770-13773.
39. Rincon-Restrepo, M.; Mikhailova, E.; Bayley, H.; Maglia, G., Controlled translocation of individual DNA molecules through protein nanopores with engineered molecular brakes. *Nano Lett.* **2011,** *11* (2), 746-750.
40. Cherf, G. M.; Lieberman, K. R.; Rashid, H.; Lam, C. E.; Karplus, K.; Akeson, M., Automated forward and reverse ratcheting of DNA in a nanopore at 5-A precision. *Nat. Biotechnol.* **2012,** *30* (4), 344-348.
41. de Zoysa, R. S. S.; Krishantha, D. M. M.; Zhao, Q.; Gupta, J.; Guan, X., Translocation of single-stranded DNA through the α-hemolysin protein nanopore in acidic solutions. *Electrophoresis* **2011,** *32* (21), 3034-3041.
42. de Zoysa, R. S. S.; Jayawardhana, D. A.; Zhao, Q.; Wang, D.; Armstrong, D. W.; Guan, X., Slowing DNA Translocation through nanopores using a solution containing organic salts. *J. Phys. Chem. B,* **2009,** *113* (40), 13332-13336.
43. Mathé, J.; Aksimentiev, A.; Nelson, D. R.; Schulten, K.; Meller, A., Orientation discrimination of single-stranded DNA inside the α-hemolysin membrane channel. *Proc. Natl. Acad. Sci. USA* **2005,** *102* (35), 12377-12382.
44. Amit, M., Dynamics of polynucleotide transport through nanometre-scale pores. *J. Phys. Cond. Matt.* **2003,** *15* (17), R581.

Chapter Three

Monitoring DNA pyrophosphorolysis at single-nucleotide resolution using a nanopore-based device

Abstract

Chapter Three builds on previous work carried out by Cockroft et al[1],[2] in the Ghadiri group at The Scripps Research Institute, California. A transmembrane, rotaxanated architecture was assembled from a DNA/PEG hybrid oligonucleotide in an alpha-haemolysin (α-HL) protein nanopore. This transmembrane rotaxanated architecture is composed of distinct but mechanically associated protein and synthetic oligonucleotide components, is transiently associated with specific molecular species (dNTPs and proteins) and its dynamic behaviour can be precisely monitored temporally and spatially at the level of an individual molecular assembly using patchclamp electrophysiological apparatus, permitting monitoring of the translational motion of the thread strand in both directions. By using this approach, we have been able to observe both nucleotide incorporation (polymerisation) and removal (pyrophosphorolysis) by the 5'-3' exonuclease deficient Klenow Fragment of DNA polymerase 1 (KF exo^{-}) DNA polymerase with single-nucleotide resolution. The sensitivity of the approach even made it possible to resolve dNTP binding and dissociation within an enzymatic binding event, providing unique views of DNA pyrophophorolysis and DNA polymerisation.

This chapter is currently being drafted as a paper for submission, and will complement other single molecule studies of DNA polymerase function[3].

3.1 Introduction

An archetypal DNA polymerase will bind to double stranded DNA and translocate along it in a random Brownian fashion until it reaches a recessed 3' end. The process involves so-called kinetic checkpoints[3] in the reaction mechanism that correspond to the formation of the non-covalent complex between the enzyme and the recessed 3'-end of the DNA. Here, the enzyme provides a privileged environment with restricted solvent access in which the reacting species are held in position by non-covalent interactions. Catalytic nucleotide incorporation involves controlling the relative orientations of the OH group on the 3' end of the recessed DNA strand, an incoming deoxynucleotide triphosphate (dNTP) and two Mg^{2+} ions. In addition to catalysing the primer extension reaction, DNA polymerases can also catalyse the more unusual reverse reaction, which is known as pyrophosphorolysis[4].

The mechanism of pyrophosphorolysis involves the attack of a pyrophosphate oxygen atom on the phosphodiester bond of the terminal base at the 3'-end of a DNA primer (Figure 3.1). The coordination of the Mg^{2+} lowers the electron density of the phosphate backbone atom such that it behaves as an electrophile that can be attacked by the oxygen atom on an incoming pyrophosphate ion. The subsequent breaking of the terminal phosphodiester bond and the formation of a new phosphatyl ester bond to give the corresponding deoxynucleotide triphosphate (dNTP) thereby shortens the length of the primer by one nucleotide.

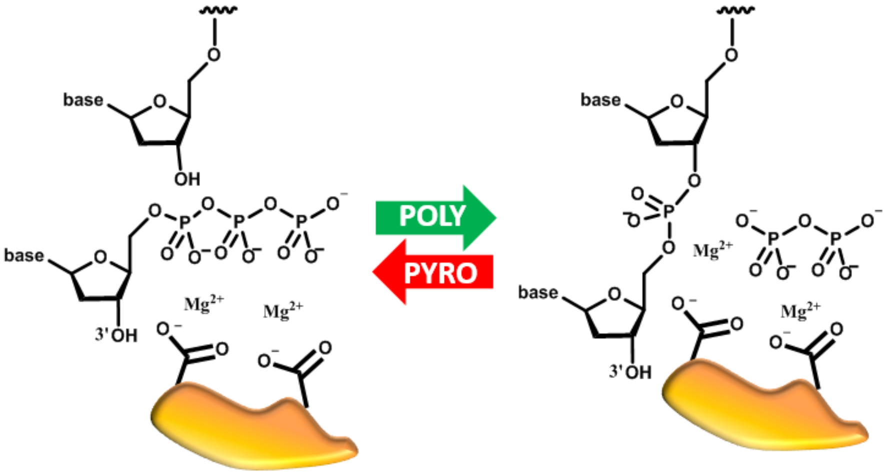

Figure 3.1 schematic representation of polymerase-mediated phosphate transfer. DNA polymerase (orange) mediated polymerisation (green arrow) involves condensation of the 3' OH of a primer strand with the alpha phosphate group of a deoxynucleotide triphosphate, producing pyrophosphate ($P_2O_7^{4-}$) and extending the length of the primer by one base. The reverse pyrophophorolysis reaction (red arrow) is the microscopic reverse of the forward reaction and involves the attack of the terminal 3' phosphate group of the primer by pyrophosphate, reducing the length of the primer by one base and producing a deoxynucleotide triphosphate.

The ability of polymerases to catalyse this less energetically favourable reverse reaction has been proposed to be part of the natural mechanism of proof reading, since misincorporated, non-complementary bases are more easily excised from a growing DNA strand[5]. Indeed, the rate limiting step has been shown to be different for a matched and a mismatched 3' base in the primer strand[6]. This difference in stability compared to a correctly matched base pair is likely to be due to differences in the conformational preferences of a mismatched terminal base pair (arising from discrepancies in steric, hydrogen-bonding, and subsequent base stacking factors[7,8]). Pyrophosphorolysis can also occur on matched duplexes under driving conditions that reverse the equilibrium position of the reaction (i.e. low concentration of dNTPs and high pyrophosphate concentration).

Pyrophosphorolysis has been exploited previously through application of pyrophosphorolysis-activated polymerisation (PAP) for ultra-sensitive detection of various genetically indicated diseases[9,10]. In PAP, a primer complementary to a known mutant form of a gene bears a non-extendable nucleotide analogue i.e. a dideoxynucleotide monophosphate (ddNMP) which must be removed by pyrophosphorolysis before a PCR-type reaction can occur. This allows the amplification and detection of the mutant DNA against of background of predominantly native DNA.

Potential substitutes for pyrophosphate that are tolerated as nucleophiles by the polymerase in the nucleotide removal reaction have also been investigated[11]. One such study investigated a related pyrovanadolysis reaction catalysed by KF exo^{-}.[12] Pyrophosphorolysis was observed at the single-molecule level using optical tweezers, although the system was only capable of observing a change in primer length equivalent to many bases over a long period of time.

Other single-molecule approaches are capable of monitoring DNA polymerase activity with single-nucleotide resolution, but to date, no observation of pyrophosphorolysis at this level of detail has yet been reported. While, for example current changes arising from conformational changes of the polymerase during forward catalysis have been determined by covalently linking KF exo^{-} to carbon nanotubes[13], no observation of pyrophosphorolysis was reported.

3.2 Design and assembly of a DNA/nanopore-based device for the detection of pyrophosphorolysis

Here we have used α-HL nanopores as a membrane spanning chassis in which to construct transmembrane rotaxanes from a streptavidin capped DNA-PEG copolymer and a short complementary DNA primer. The design of a DNA/nanopore-based device for the detection of pyrophosphorolysis was based on previous single-molecule studies by Cockroft et al[2]. It was hoped that a slightly modified system design (Figure 3.2) would enable the detection of both DNA-polymerase catalysed nucleotide incorporation and pyrophosphorolytic base removal with single-nucleotide resolution. Single channels were obtained and rotaxanes constructed according to the general procedure outlined in the materials and methods section at the end of this chapter.

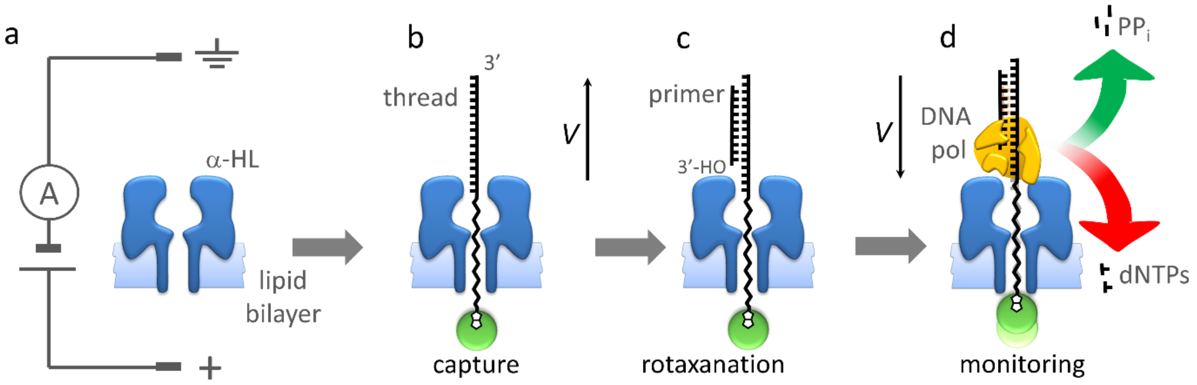

Figure 3.2 Assembly of the DNA-PEG/α-HL transmembrane rotaxane and the principle of monitoring incorporation/pyrophosphorolysis events. Negative potentials are defined as those under which negative ions flow through the pore from the narrow stem to wider vestibule sides of the pore.**a** A single α-HL nanopore is inserted in a planar lipid bilayer, transmembrane potentials were applied and the ion current through the pore monitored using patch clamp apparatus. **b**, a DNA-PEG copolymer thread strand (thread) present in the live well was captured in the pore by application of a –140 mV potential which resulted in a reduction in the ion current from around –18 pA to –5 pA. **c**, the potential was reduced to -28 mV to allow a complementary primer strand (primer) present in the grounded well to hybridise to the 5’ end of the thread protruding from the vestibule of the pore. The hybridisation of the primer to the thread left a four base 3’ overhang of the thread ensuring that the only substrate position for polymerase is the recessed 3’ end of the primer **d**, At positive applied potentials the enzyme-mediated phosphate exchange reaction taking place at the 3’ end of the primer can be followed by monitoring stepped changes in the ion current corresponding to the primer length.

3.3 Real-time nanopore observation of consecutive incorporations and pyrophosphorolyses

After characterisation of the rotaxanes using the stepped-voltage protocol (see materials and methods), timecourse experiments were conducted in the presence of the DNA polymerase KF exo^{-}, Na_4PP_i and dNTPs. A constant transmembrane potential of +25 mV was applied and current changes monitored to observe consecutive pyrophosphorolysis and nucleotide incorporation events. Certain features are immediately apparent by visual inspection of the ion current traces.

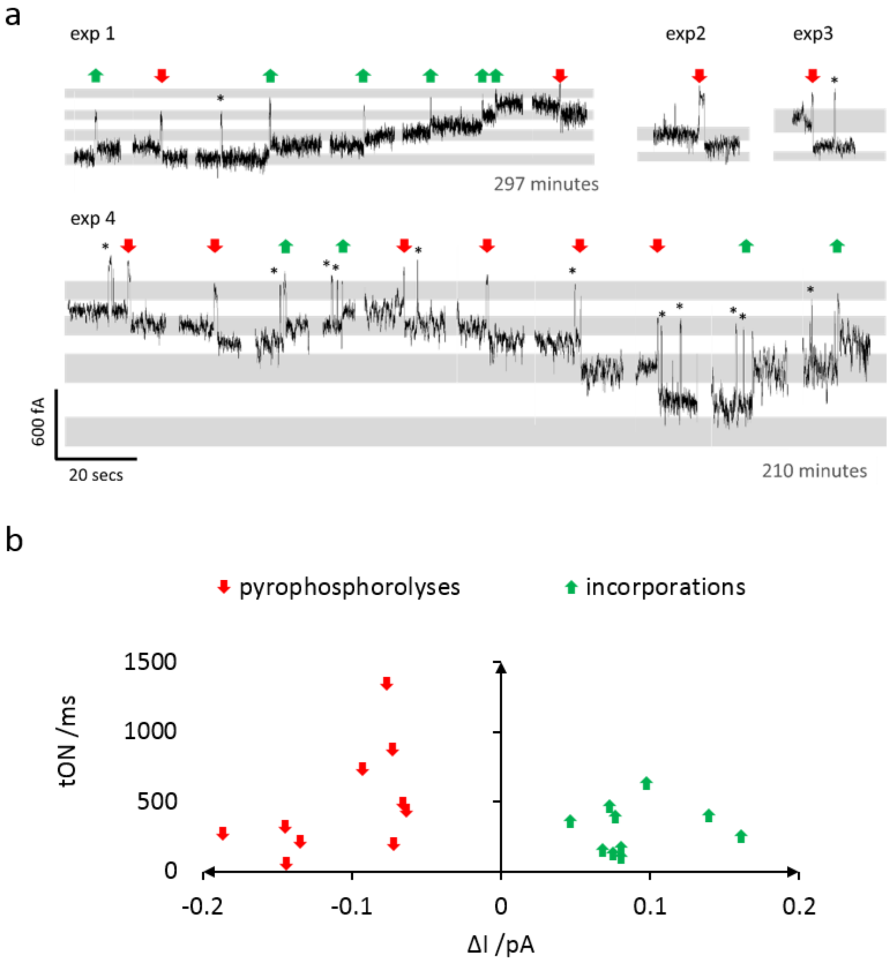

Figure 3.3 **a**, single-molecule observation of pyrophosphorolysis (red downward arrows) and nucleotide incorporation events (green upward arrows). Four individual experiments were performed (exp.1-4). The grond well contained KF exo^{-} polymerase [~7 nM], deoxynucleotide triphosphates [~12 mM] each and Na_4PP_i [~4 mM] Data were low-pass Bessel filtered at 10 Hz and aligned such that electrode drift (due to electrochemical decomposition of the electrodes over the course of these long-duration experiments) was compensated for, the gaps represent contractions of the elapsed time in which no reactions occured. The *s represent enzyme binding events in which no reaction occurred **b**, enzyme-mediated phosphate exchange events from all four experiments.

Step changes in the observed current corresponding to changes in the length of the primer strand always occur concurrently with enzyme binding events (Figure 3.3a). The qualitative similarities between each of the pyrophosphorolysis and incorporation events, and between the current steps observed in the presence of one and two or three rotaxanes are clearly visible. Experiment one shows an experiment involving a single rotaxane, which shows the low noise characteristic of a single channel. However, in this and successive experiments (experiments two and three) pyrophosphorolysis events were rare. In order to record more events, an experiment where two rotaxanes were present and during in which a third was assembled, was performed (experiment four). While this meant that there was greater noise in the system it still allowed more events to be observed in a reasonable timeframe (see materials and methods).

In total, ten incorporation and ten pyrophosphorolysis events were observed across four experiments. A comparison of all the events was carried out using the single channel search feature in the Clampfit software to quantify the duration and current changes associated with each type of event. A scatterplot of all the events (Figure 3.3b) by total duration (τ) *vs.* ΔI shows the reciprocal similarity between pyrophosphorolysis and nucleotide incorporations, that is the microscopic reversibility of the enzyme-mediated phosphate-transfer reaction. From visual inspection it is clear that while similar, there is a range of duration and ΔI values for the events (Figure 3.3b). Pyrophosphorolysis steps were found to take on average around 25% longer with respect to incorporation under the conditions used despite using a final concentration of 4 mM PP_i *versus* 12 µM dNTPs. However, these values were the same within error and most likely a greater number of events would reveal that pyrophosphorolysis and polymerisation take the same time on average.

Sub-levels can also be seen in the ion current traces shown in Figure 3.3a. Particularly interesting are the stepped changes that were sometimes observed during the polymerase binding events. In general, incorporation steps had positive internal current changes (ΔI_{int}) during polymerase binding, while those during pyrophosphorolysis events are negative. The limited number of incorporation and pyrophosphorolysis events observed, and the stochastic, highly variable nature of single-molecule recordings precludes a more detailed analysis. Nonetheless, it is interesting to speculatively map these finer details in the ion current traces

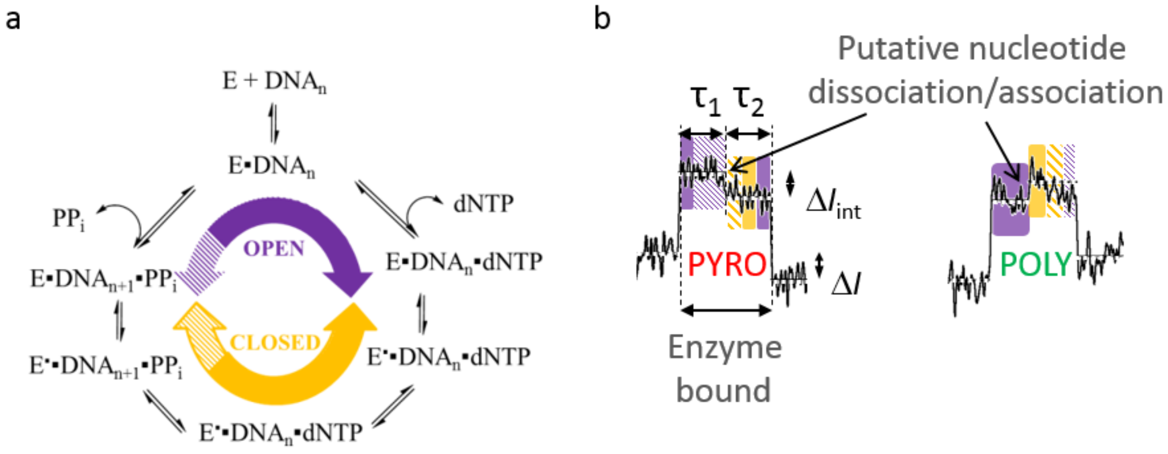

Figure 3.4 Speculative mapping of the mechanistic cycle of polymerase activity onto ion current traces observed using the nanopore-based approach. **a** Cycle of open and closed conformational change adapted from[13] showing the sequence of events of pyrophosphorolysis and incorporation. **b** Mapping of the sequence of states from the cycle on to pyrophosphorolysis and incorporation events observed during the present work. The relative durations of the solid and hashed regions of the overlay are speculative and do not reflect any measurements.

onto suggested mechanistic cycles of nucleotide incorporation and pyrophosphorolysis (Figure 3.4). Conformational changes of the DNA polymerase have also been shown to be important in the catalytic cycle[14]. The structures of DNA polymerases resemble a hand-shape, and are commonly referred to as containing a ‘fingers’, a ‘thumb’ and ‘palm’ sub-domains. The polymerase transitions between so-called ‘open’ and ‘closed’ conformations relating to the relative positions of the finger, thumb and palm regions during its catalytic cycle. The open state occurs after binding of the enzyme to DNA upon which PP_i or dNTP associate with the complex forming the closed ternary complex, bond rearrangement then occurs during the lifetime of the closed state followed by dissociation of the PP_i or dNTP, returning the enzyme to the open state at which point it may dissociate or translocate to the next nucleotide position.

Further experiments would be needed to confidently relate variables such as the durations (τ_1 and τ_2) and the current changes between the internal component states (ΔI_{int}) to the mechanistic aspects of the catalytic process such as conformational changes and binding events.

3.4 Conclusions & future work

The previously devised nanopore transmembrane rotaxane approach was successfully extended to monitor pyrophosphorolysis as well as nucleotide incorporation events under driving conditions. Events were monitored in real time and multiple successive events corresponding to translational mechanical motion of the thread strand in both directions were observed. This work thereby represents an important early step in the demonstration of rationally designed transmembrane molecular machines. In addition, events were monitored on as many as three concurrently assembled transmembrane rotaxanes and the utility of such low copy number molecular assembly systems was thereby established.

In future work, a greater number of events could be observed and analysed which would allow the construction of histograms and the calculation of the relative lifetimes for the open and closed complexes of each type of event and hence the energies of each. A follow-up study could investigate the effect of mismatched terminal bases in rotaxanes and use the approach to compare the rates of matched and mismatched pyrophosporolysis. In order to potentially extract work from similar systems, a large number of nanopore devices would need to be concurrently assembled in a single bilayer membrane. Thus, future work might also aim to determine inherent limits on the number and density of rotaxane-based devices that can be assembled in a membrane.

3.5 Materials and Methods

M3.1 DNA used to construct rotaxanes

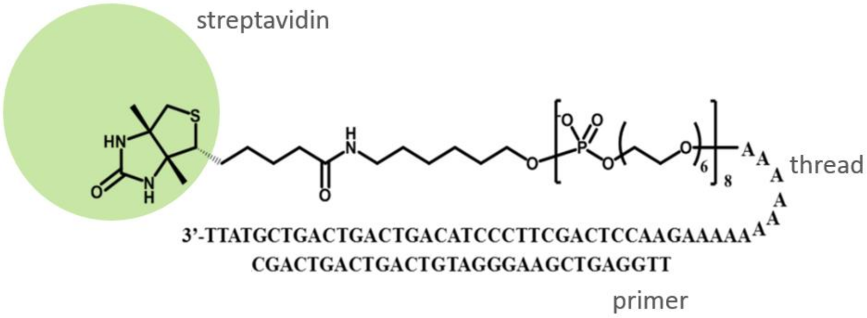

Figure M3.1 The structure and sequence of the thread and primer strands used to construct transmembrane rotaxanes used to monitor enzyme-mediated phosphate exchange. The sequences were designed for a different initial project described in Chapter Four of the present work and hence full synthesis and characterisation details are given in Chapter Four section M4.3.

M3.2 Patch Clamp Experiments

Nanopore experiments were performed at 21 ±2 ^{o}C in the custom built cell, stable lipid bilayers and single channels were obtained as described in Chapter Two of the present work. In the experiments in Chapter Three, the aqueous buffer used contained KCl [150 mM], Tris –HCl pH 8 [25 mM] and $MgCl_2$ [10 mM]. The live well contained streptavidin capped thread [~100 nM] prepared from a 4.1:1 molar ratio of the thread strand to streptavidin in order to avoid complications to the signal that may arise form differently substituted streptavidin. Primer DNA (5 μL, 300 μM) was added to the ground well. A −140 mV transmembrane voltage was applied until capture of a thread strand. The potential was reduced to −28 mV for ten minutes to allow the primer to hybridise to the 5' end of the thread protruding into the ground well.

M3.3 Characterisation of DNA-PEG/α-HL rotaxanes

Once formed, the rotaxanated thread is susceptible to the applied electric field as it is constructed from polyanionic DNA and PEG. This susceptibility is different for PEG and DNA as they have a different charge density. DNA contains between three and four charges

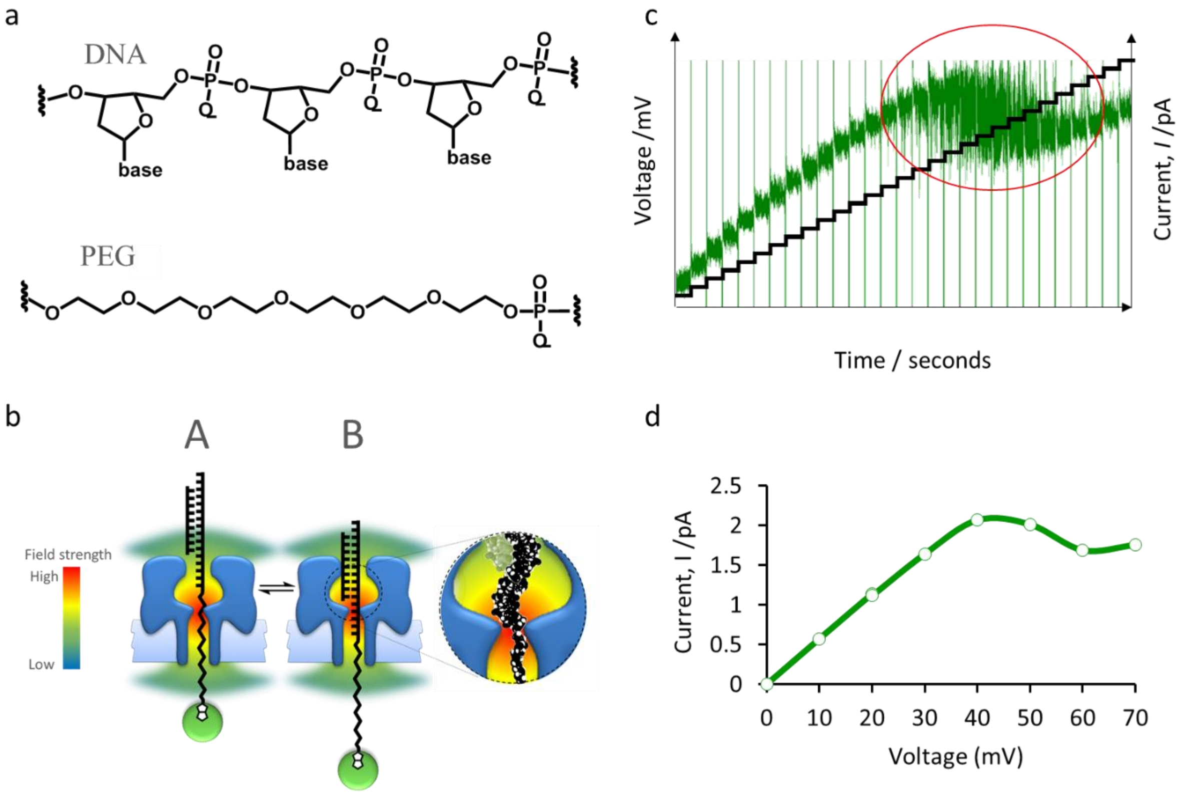

Figure M3.2 Principle of nanopore rotaxane translational position monitoring. **a** Structures of PEG and DNA. **b** Cartoon depiction of the change in the electric field strength across the pore cross-section. **c** Real-time current response of the nanopore rotaxane to a stepped voltage protocol (0 to 70 mV in two second sweeps each 2.5 mV apart). **d** Average current at ten mV potential intervals, leading to the *I/V* trace shape that is characteristic of a rotaxane.

for every one on a section of PEG of the same length (Figure M3.2a). An assembled rotaxane exists in a dynamic equilibrium between two states (A and B) due to the energy penalty associated with the entry of the duplex region of the DNA into the vestibule region of the pore (Figure M3.2b). The position of the equilibrium exhibits a voltage dependence. The difference in cross-sectional area and charge density of the DNA and PEG regions of the thread strand results in a difference in the ion flux through the pore depending on the relative occupation of the stem region of the pore by DNA and PEG. The ion current is thereby indicative of the time averaged translational position of the thread within the pore. The rotaxanes were characterised by applying two second transmembrane potential sweeps from 0 to +70 mV. Lower voltages are insufficient to overcome the activation barrier for duplex entry to the vestibule so the stem is mostly occupied by PEG, such that the current increases approximately linearly with potential. However, at higher positive potentials the equilibrium is perturbed. The red circled region in Figure M3.2c, indicates the voltage range where shuttling of the DNA/PEG in and out of the pore results in fluctuations in the ion current. As the applied potential continues to increase the equilibrium is driven completely to the right, the shuttling stops and the current begins to increase linearly with potential once more. The slope of the increasing current is shallower than before as there is now DNA in the stem rather than PEG. Although this dynamic behaviour is interesting from a single-molecule biophysics perspective, the average current at each potential can be simply interpreted as being diagnostic of the length of the DNA primer strand.

M3.4 Real-time monitoring of enzyme binding

Since at low potentials the equilibrium is mostly towards state A, the binding of proteins such as DNA polymerases to the 3'OH of the primer is also discernable from changes in the current at low positive potentials, since the 'footprint' of the enzyme pulls the thread strand against the applied potential, varying the PEG/DNA ratio inside the pore (Figure M3.3a). On binding the 3'OH end of the primer, the DNA polymerase is able to catalyse both the incorporation of dNTPs and the pyrophosphorolysis of the primer strand. Thus, since polymerase binding, primer extension, or nucleotide removal by pyrophosphorolysis all change the DNA/PEG ratio inside the pore, these events can be detected using the DNA/nanopore rotaxane device. it is possible to record in real-time and filter the data (Figure M3.3b) to reveal transient sub-nanometre changes in the translational position of the thread due to KF exo^{-} binding.

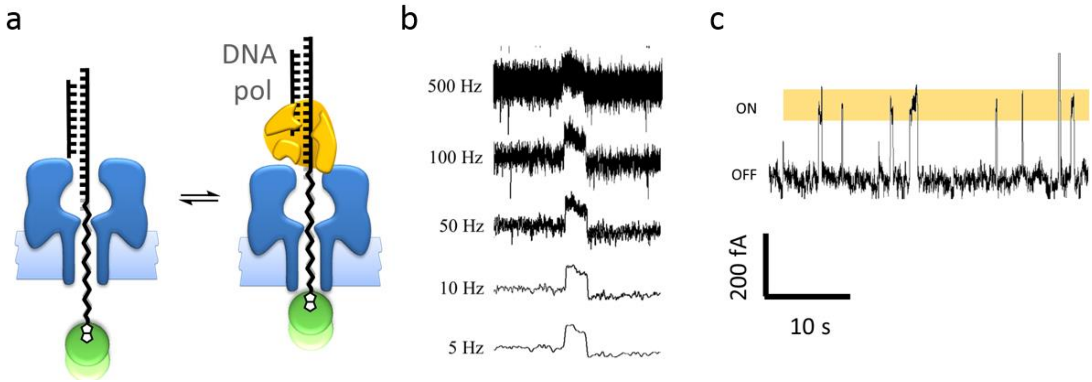

Figure M3.3 **a**, Principle of monitoring DNA polymerase (KF exo^{-}) binding at low constant applied potentials. **b**, Effect of filtering on clarity and detail of signal. Definition between different current states and hence clarity of strand translational position within the pore is improved by applying a low pass Bessel filter to data post-acquisition. It can be seen that a filter level of between 50 and 5 Hz allows the discrimination of similar but distinct translational conformations on the timescale of single molecular machine motions without loss of the main temporal features. **c**, real-time current data filtered post acquisition using an 8-pole Bessel filter of 10 Hz.

In real-time pyrophosphorolysis experiments KF exo$^-$ (Fermentas) [~7 nM] and Na_4PP_i [4 mM] were added to the ground well and a potential of +25 mV was applied and data were recorded using an Axon Axopatch 200B (Molecular Devices) equipped with a CV203BU headstage (Molecular Devices), and digitized using an Axon Instruments Digidata 1332A at a sample rate of 50 kHz. Single-channel ion current recordings were processed with Clampex 10.2 and Clampfit 10.2 software. Ion current traces were digitally filtered at 10 kHz. Events were extracted using the threshold search function in Clampfit 10.2 and then processed using Origin 9 Pro and Microsoft Excel 2010.

M3.5 Viability of data from multiple concurrently assembled rotaxanes

Sometimes a second or third channel would insert after initial formation of a single transmembrane rotaxane. This permitted the concurrent assembly of multiple rotaxanes (RTX) thereby allowing observation of a greater number of enzyme binding events and hence phosphate transfer reactions in a given experimental time. In figure M3.4a, the *I/V* curves resulting from two (triangles) or three (circles) rotaxanes have the same form as for a single rotaxane (squares). In real-time current monitoring experiments at constant applied potential the signal noise increased monotonically with each rotaxane present. However, after filtering both enzyme binding (transient spikes) and phosphate transfer reactions (downward red arrows) were clearly visible (Figure M3.4b).

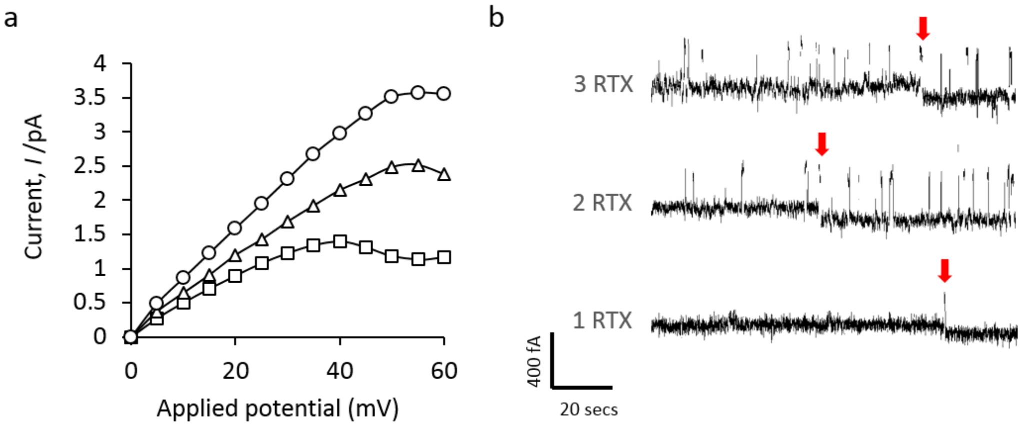

Figure M3.4 Characterisation with multiple rotaxanes. **a**, *I/V* sweeps obtained with one, two or three rotaxanes. **b**, real-time current data showing the small increase in noise and the similarity between enzyme binding and pyrophophorolysis when one, two or three rotaxanes are present. Red arrows indicate the step-change in current level associated with pyrophosphorolysis.

3.6 References

1. Cockroft, S. L.; Chu, J.; Amorin, M.; Ghadiri, M. R., A single-molecule nanopore device detects DNA polymerase activity with single-nucleotide resolution. *J. Am. Chem. Soc.* **2008,** *130* (3), 818-820.
2. Chu, J.; González-López, M.; Cockroft, S. L.; Amorin, M.; Ghadiri, M. R., Real-time monitoring of DNA polymerase function and stepwise single-nucleotide DNA strand translocation through a protein nanopore. *Angew. Chem., Int. Ed.* **2010,** *49* (52), 10106-10109.
3. Berezhna, S. Y.; Gill, J. P.; Lamichhane, R.; Millar, D. P., Single-molecule Förster resonance energy transfer reveals an innate fidelity checkpoint in DNA polymerase I. *J. Am. Chem. Soc.* **2012,** *134* (27), 11261-11268.
4. Hanami, T.; Oyama, R.; Itoh, M.; Yasunishi-Koyama, A.; Hayashizaki, Y., New pyrosequencing method to analyze the function of the Klenow fragment (EXO−) for unnatural nucleic acids: pyrophosphorolysis and incorporation efficiency. *Nucleosides, Nucleotides and Nucleic Acids* **2012,** *31* (8), 608-615.
5. Johnson, S. J.; Taylor, J. S.; Beese, L. S., Processive DNA synthesis observed in a polymerase crystal suggests a mechanism for the prevention of frameshift mutations. *Proc. Natl. Acad. Sci.USA* **2003,** *100* (7), 3895-3900.
6. Joyce, C. M.; Benkovic, S. J., DNA polymerase fidelity: kinetics, structure, and checkpoints†. *Biochemistry* **2004,** *43* (45), 14317-14324.
7. Wu, S.; Beard, W. A.; Pedersen, L. G.; Wilson, S. H., Structural comparison of DNA polymerase architecture suggests a nucleotide gateway to the polymerase active site. *Chem. Rev.* **2013**.
8. Li, Y.; Korolev, S.; Waksman, G., Crystal structures of open and closed forms of binary and ternary complexes of the large fragment of Thermus aquaticus DNA polymerase I: structural basis for nucleotide incorporation. *EMBO J.* **1998,** *17* (24), 7514-7525.
9. Liu, Q.; Sommer, S. S., PAP: Detection of ultra rare mutations depends on P* oligonucleotides: “Sleeping Beauties” awakened by the kiss of pyrophosphorolysis. *Human Mutation* **2004,** *23* (5), 426-436.
10. Shi, J.; Liu, Q.; Sommer, S. S., Detection of ultrarare somatic mutation in the human TP53 gene by bidirectional pyrophosphorolysis-activated polymerization allele-specific amplification. *Human Mutation* **2007,** *28* (2), 131-136.
11. Rozovskaya, T.; Tarussova, N.; Minassian, S.; Atrazhev, A.; Kukhanova, M.; Krayevsky, A.; Chidgeavadze, Z.; Beabealashvilli, R., Pyrophosphate analogues in pyrophosphorolysis reaction catalyzed by DNA polymerases. *FEBS Lett.* **1989,** *247* (2), 289-292.
12. Akabayov, B.; Kulczyk, A. W.; Akabayov, S. R.; Theile, C.; McLaughlin, L. W.; Beauchamp, B.; van Oijen, A. M.; Richardson, C. C., Pyrovanadolysis, a pyrophosphorolysis-like reaction mediated by pyrovanadate, Mn^{2+}, and DNA polymerase of bacteriophage T7. *J. Biol. Chem.* **2011,** *286* (33), 29146-29157.
13. Olsen, T. J.; Choi, Y.; Sims, P. C.; Gul, O. T.; Corso, B. L.; Dong, C.; Brown, W. A.; Collins, P. G.; Weiss, G. A., Electronic measurements of single-molecule processing by DNA polymerase I (Klenow fragment). *J. Am. Chem. Soc.* **2013,** *135* (21), 7855-7860.
14. Wu, E. Y.; Beese, L. S., The structure of a high fidelity DNA polymerase bound to a mismatched nucleotide reveals an “Ajar” intermediate conformation in the nucleotide selection mechanism. *J. Biol. Chem.* **2011,** *286* (22), 19758-19767.

Chapter Four

Towards a prototypical pump based on a reciprocating transmembrane nanoactuator

Abstract

As described in Chapter One, natural transmembrane molecular machines share certain key architectural features that provide a conceptual basis for the rational design of biomimetic functional transmembrane architectures. Such systems are composed of chemically distinct, but mechanically associated moieties. They perform work in response to transmembrane gradients[1] and/or the presence of specific chemical species to bias Brownian motion and undergo hysteretic cycles of conformational change[2]. This work may take the form of a reaction between substrate molecules or the transport of analytes[3]. In Chapter Three an assembled transmembrane rotaxanated complex that allowed observation of DNA polymerase activity in both forward and reverse directions was introduced. This bidirectional translational motion occurred in a random fashion under equilibrium conditions meaning that there was no potential for work to be extracted from the motion. In this Chapter, the nanopore rotaxane approach is further developed by redesigning the thread and primer sequences to include the recognition site for a nicking endonuclease. This affords a system in which the translational motion of the synthetic transmembrane component displays hysteresis and hence a temporally asymmetric transmembrane potential energy surface is generated. The system's applicability as a prototypical transmembrane pump by exploitation of this potential is considered. Natural precedent exists for the use of linear actuation to pump protons across a membrane in the respiratory complex[4].

4.1 Introduction

One key feature of natural molecular machines is their cyclical behaviour[5], which must therefore also be possessed by any candidate transmembrane molecular machine. Molecular machines perform work by cycling through a range of conformational states in a temporally asymmetric fashion. Let us first consider the machine-like properties of nanopore-rotaxane systems[6,7] described in Chapters One and Three. In these systems, a DNA polymerase was used to extend a short DNA primer allowing readout of the number of incorporations by monitoring of the residual ionic current that flowed through a nanopore under an applied transmembrane potential. The system was constrained to terminate primer extension at a precisely defined point in the sequence by withholding one of the required dNTPs. In order to impart cyclical behaviour to that system, a method of removing the extension and returning the system to its initial condition is required. This chapter describes how the sequences of the thread and primer strands were redesigned to include a recognition site for a nicking endonuclease that allows the rotaxanated system to be reset to the initial state. A nicking endonuclease is a restriction enzyme that binds to a specific sequence of double stranded DNA and cleaves one strand selectively by sequence specific catalytic hydrolysis while leaving the other intact. Natural examples have been discovered[8] and many artificial ones have been prepared. In the case of the nicking enzyme Nt.AlwI, this was done by genetic recombination to produce a heterodimeric fusion protein comprising one recognition domain of AlwI fused to the non-functional dimerisation domain of the naturally occurring nicking endonuclease Nt.BstNBI. Previous uses of Nt.AlwI have included DNA signal amplification[8]

4.2 Design of a transmembrane reciprocating nanoactuator

To construct the transmembrane reciprocating nanoactuator (Figure 4.1) an individual α-HL nanopore is inserted in a planar lipid bilayer according to the general procedure outlined in the materials and methods section and monitored with patch clamp apparatus (Figure 4.1a). A DNA-PEG copolymer thread strand is captured in the pore by application of a negative transmembrane potential of −140 mV (Figure 4.1b). The potential is reduced to –28 mV upon capture of the thread to allow rotaxanation by a short primer strand (Figure 4.1c). The assembled transmembrane rotaxanated architecture is then monitored by applying a constant positive potential of +25 mV and observing the changes in ion current through the pore in response to the reciprocal nanomechanical motions of the thread strand due to the actions of KF exo$^-$ DNA polymerase and nicking enzyme Nt.AlwI (Figure 4.1d). KF exo$^-$ incorporates dNTPs at the 3’ OH of the primer to drive a ratcheted power stroke. The duplex sequence containing the synthesised region highlighted in Figure 4.1d) expansion is recognised by the nicking enzyme Nt.AlwI which can nick the primer strand at the position indicated by the red triangle, removing any of the subsequent bases (shown in green). It should be noted that the nicking site lies outside the recognition domain which is included in the initial primer and hence the number of incorporations that can occur before cleavage is not fixed. However, the extent of polymerisation and hence the range of waste products is controlled by withholding dTTP from the experiment so that no more than eight bases can be incorporated. Displacement of the nicked primer fragment waste (green) returns the system to its initial state by a different route than simply the reverse of the polymerisation process as per the requirement for cyclical machine-like behaviour as described in Chapter One.

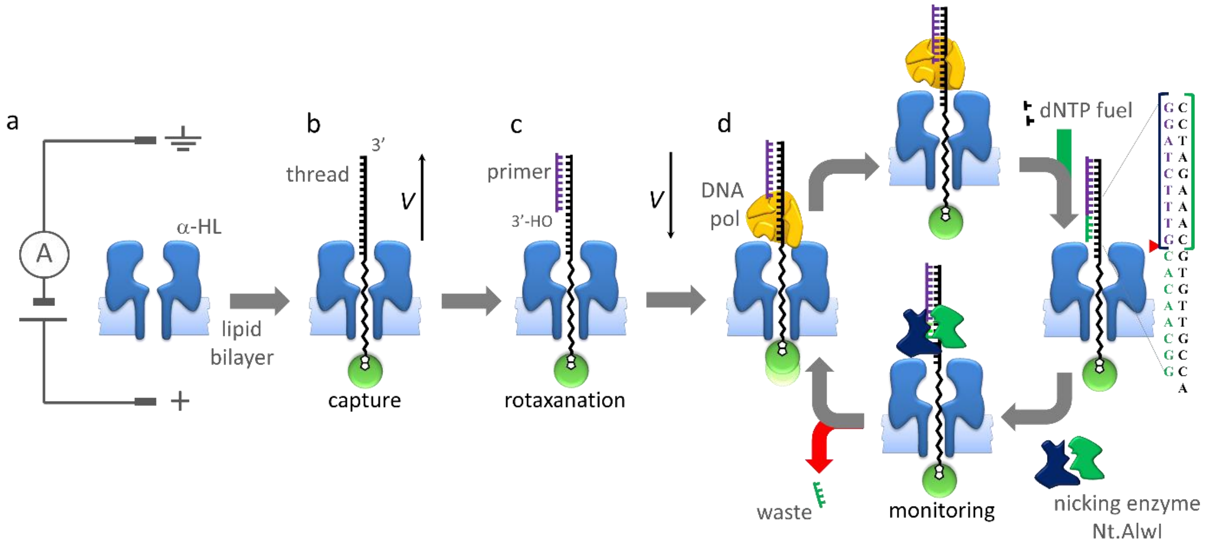

Figure 4.1 Assembly and operation of the reciprocating transmembrane nanoactuator. **a**, an individual α-HL pore is inserted in a lipid bilayer allowing the current through the pore to be measured by a patch clamp apparatus which applies transmembrane potentials. **b**, a DNA-PEG copolymer thread strand is captured at −140 mV. **c**, a single stranded DNA primer strand hybridises to the end of the thread strand protruding through the pore. **d**, at positive applied potentials the ion current through the pore will provide a read out of the position of the thread and thus will report on the nanomechanical state of the assembly during the cycle of operation.

The initial thread and primer sequences were reached by iteratively adapting the thread sequence used in reference[6] to include the recognition domain for Nt.AlwI by using Dinamelt online oligo analysis software to screen the melting temperatures of the sequences’ desired duplex region and any unwanted secondary structures that would compete with the desired assembly. The sequences used are summarised in Figure 4.2. The region in blue shows where the previously proven sequence[6] was changed to incorporate the Nt.AlwI recognition domain,

Oligo	**Sequence (5'→3')**	**T_m °C (homodimer)**	**T_m °C (complex)**
JACS thread	B(PEG)$_8$AAAAAAAAAAAACCGTTGTGCTTCCCTACAGTCAGTCAGTCGTATTA	3.6	78.1
thread 1	B(PEG)$_7$AAAAAAAAAAAAAAACCGTTGTG≠CAAAGATCCCTACAGTCAGTCGTATTA	9.8	76.8
thread 2	B(PEG)$_8$AAAAAAAAAAAACCGTTGTG≠CAAAGATCCCTACAGTCAGTCGTATTA	9.8	76.8
primer 0	TAATACGACTGACT GTAGGGATCTTTG≠	1.2	76.8

Figure 4.2 Comparison of sequences previously published in reference[6] (JACS thread) and those used in the actuator design that employed nicking enzyme Nt.AlwI.

(underlined). 'B' indicates the 5' biotinyl modification and 'PEG' indicates the hexaethylene glycol phosphate spacer. The relative position of the nick site is indicated by '≠'.

The effect of the redesign on the T_m of the desired duplex and of competing secondary structures was minimal given that experiments were conducted at 21 ±2 °C so the unwanted homodimer interactions would be neglible.

4.3 Assembly of a transmembrane rotaxane using thread 1

Having developed a protocol for preparation of the biotinylated thread 1 strand by enzymatic assembly and having established that Nt.AlwI could function in the nanoactuator buffer (see materials and methods) it was attempted to assemble and characterise the rotaxanated system using primer 0 and primer 8. Attempts to form rotaxanes using oligonucleotides prepared by the enzymatic ligation strategy were mostly unsuccessful. Potential reasons for this might include low duplex stability due to damage to the DNA during UV transillumination, electroelution and/or depurinataion during manual detritylation or the presence of residual chaotropic reagents from the agarose gel extraction kit used in the purification of the ligated strands. However, the reasons for failure to obtain rotaxanes were not systematically investigated. A rotaxane was successfully assembled using thread 1 with primer 0 only once and characterised using a similar stepped voltage protocol to that used in Chapter Three. Addition of primer 8 to the assembled rotaxane resulted in the change of shape of the *I/V* trace (Figure 4.3). The current changes seen between 20 and 40 mV was smaller than that previously seen during observation of KF exo$^-$ activity, suggesting that it would be difficult to see the cyclical pattern of activity using a thread with only seven PEG units.

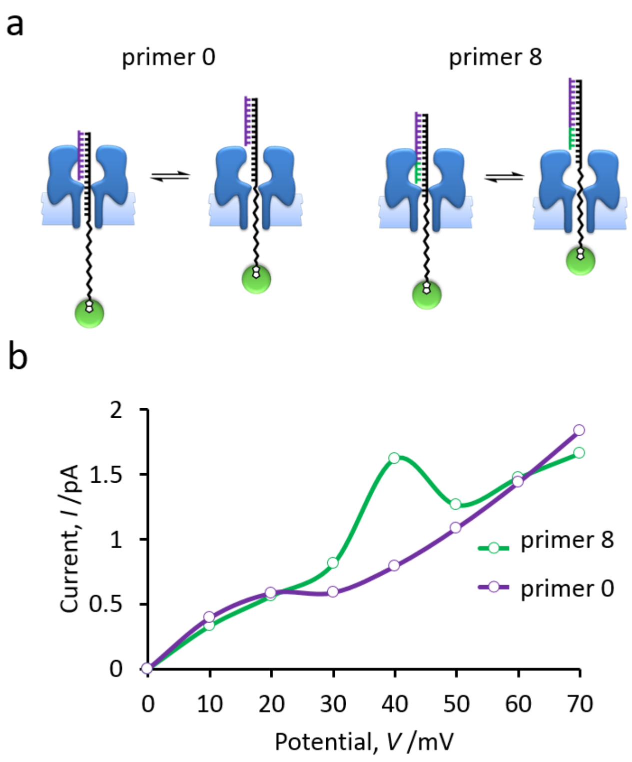

Figure 4.3 *I/V* traces for the control primer rotaxanes formed between thread 1 and primer 0 (purple) or primer 8 (green) . Potentials of 0 to 70 mV were applied in 10 mV steps for two seconds each and the average current taken between t = 0.5 s and t = 1.9 s at each potential. The shape of the curve arises due to the rapid oscillation of the duplex region

The current changes seen between 20 and 40 mV was smaller than that previously seen during observation of KF exo$^-$ activity, suggesting that it would be difficult to see the cyclical pattern of activity using a thread with only seven PEG units.

Thread 1 was constructed from synthesized DNA fragments using an enzymatic assembly strategy (Figure M4.1-4) Difficulties were encountered with forming rotaxanes using thread 1. In light of this and the aforementioned small current changes associated with the thread containing only seven PEG units, a thread strand containing eight PEG units (thread 2) was designed and synthesised in a single solid phase oligonucleotide synthesis run.

4.4 Observation of reciprocating movements in a thread 2 rotaxane

Assembly of transmembrane rotaxanes using thread 2 and primer 0 was still difficult but was accomplished on a number of occasions. The competency of the rotaxane as a substrate for KF exo$^–$ was demonstrated by performing an experiment in which a high concentration of KF exo$^–$ and dA/dC/dGTP were present. The observed changes in shape of the *I/V* curve

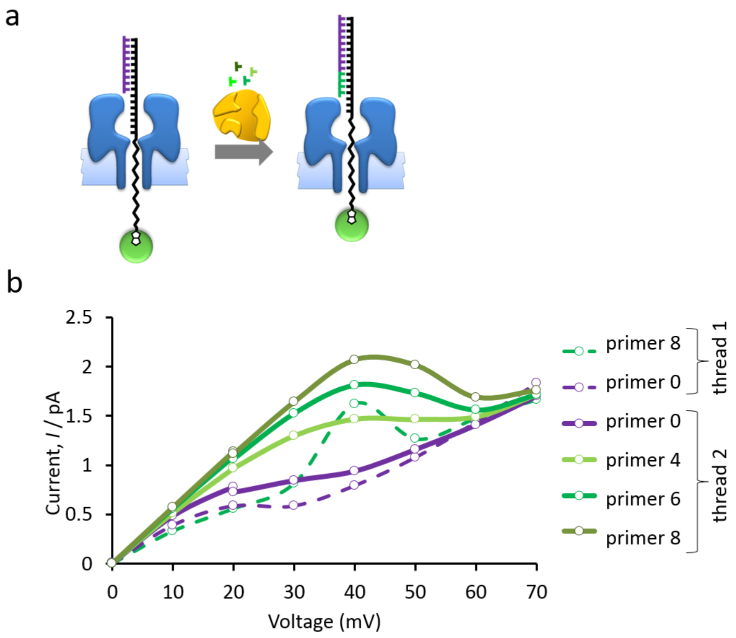

Figure 4.4 **a** Schematic of the states of the rotaxane before and after incorporation of eight dNTPs **(b)** the *I/V* curve of the rotaxane formed with primer 0 (solid red line), which changed rapidly after addition of dA/C/G/TP (100 µM) successively through primer 4, to primer 6 and finally to primer 8 (dark green). The corresponding curves for control +0 and +8 primers with the former thread design, thread 1 are shown for comparison (dashed red and green lines). The greater diagnostic range at lower potentials (20 to 40 mV) afforded by the inclusion of eight rather than seven PEG units is clear, although the absolute maximum current values observed is also sensitive to the condition of the channel itself and slight differences in the concentrations of buffer constituents present. In this case the high concentration of dNTPs most likely contributed to the high current observed for primer 8.

established the feasibility of the first half of the cycle of operation, and allowed identification of the current levels accessed over the course of a cycle (Figure 4.4).

Having monitored multiple incorporation events using KF exo$^-$ by using the stepped voltage protocol, it was observed that the biggest current change resulting from changing the translational position of the thread (primer length) was observed at +40 mV. Therefore, in subsequent experiments data were collected at + 40 mV (whether applying a stepped voltage protocol or applying a constant potential). The experiment shown in Figure 4.5a showed an initially high current level, which dropped sharply to the lower level associated with primer 0. The bilayer became unstable after ~ t = 11000 seconds, the region of the graph around this point might show competition between strand displacement and nicking or it may be due to bilayer instability. In a subsequent experiment shown in Figure 4.5b, a single cycle of operation from state (i) to (iv) was observed using a rotaxane assembled with primer 0 and plotting the data from the +40 mV portion of the stepped voltage protocol. Five incorporations were made

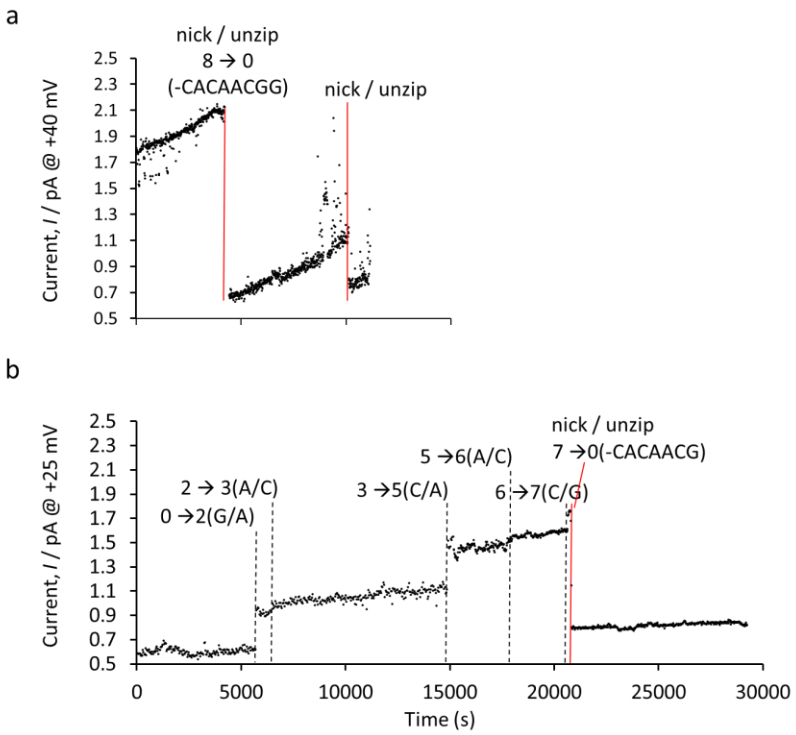

Figure 4.5 Ion current recordings showing the nicking transition from state (iii) to (iv) on a rotaxane prepared using primer 8 at a constant potential of +40 mV. The slopes in the ion current recording are due to electrode drift which is more problematic at constant applied potentials.

before one nicking event and no further incorporations were observed before the bilayer became unstable.

Although these preliminary experiments showed some promise, rotaxane formation using thread 2 remained difficult, and the rotaxanated complexes were often not stable for extended periods. This made incorporation or nicking events difficult to observe. The poor stability of the rotaxanes may have been due to depurination of the thread strand during the manual detritylation step of the DNA synthesis of the thread strands. As the bond between the cyclic nitrogen of the 5’ biotin and the dimethoxytrityl protecting group is known to be less acid labile than the equivalent bond between the 5’oxygen of a standard oligonucleotide and the DMT group, harsher detritylation conditions were used than in standard unmodified DNA synthesis – the reaction was performed for longer in 40% (v/v) rather than 20% (v/v) acetic acid. The limited stability compared to previous studies[6],[7] may have also been due to differences in the sequences used; former work contained a terminal CCC/GGG region which may have stabilised the duplex. In addition, it was reasoned that the nicking enzyme might bind more strongly to the duplex DNA than KF exo^{-} and that this might reduce the rate of nucleotide incorporation. Given this possibility, and the fact that the design of the sequence mean that nicking could occur at any time after a single nucleotide incorporation event, the uniformity of the cyclical behaviour was not guaranteed. Hence, it was decided to further refine the sequence design to improve the separation between the binding sites of the two enzymes, with the hope that this would improve the chances of observing repetitious cyclical behaviour.

4.5 An improved nanoactuator design

A different nicking endonuclease Nb.BbvCI[10] was identified with properties that addressed the concerns outlined in the previous section. This enzyme has also found use in previous work in DNA nanotechnology[11]. By changing the primer and thread strands a system was designed that is ‘un-nickable’ until a certain number of polymerase-catalysed incorporations have taken place at the 3’ end of the primer (Figure 4.6). This circumvents any potential issues of enzyme footprint overlap by ensuring that the nicking enzyme would dissociate from the duplex after a nicking event, potentially improving the cyclical behaviour of the system.

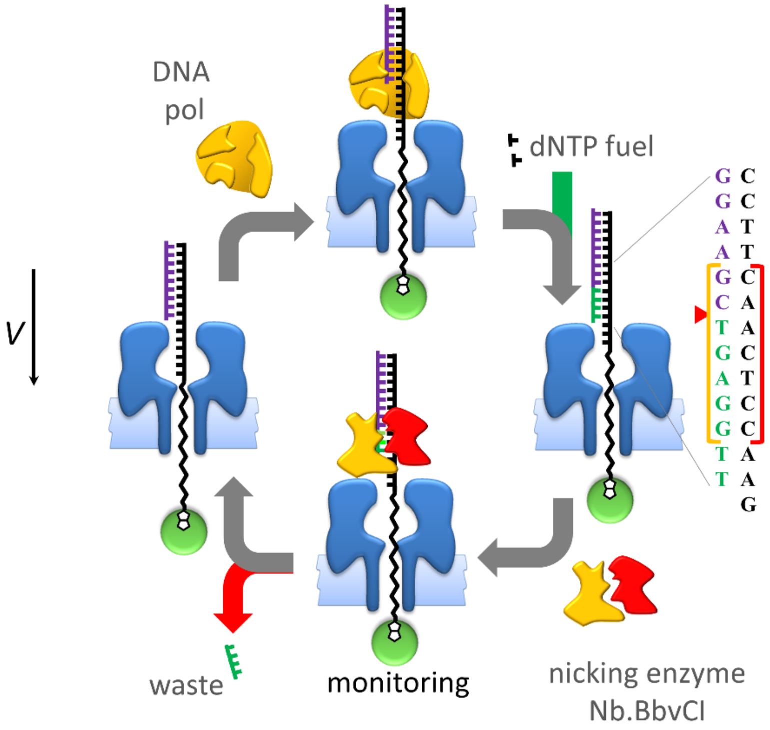

Figure 4.6 Cycle of operation of a reciprocating nanoactuator that uses the nicking enzyme Nb.BbvCI. The operational cycle is similar to that for the actuator using Nt.ALwI, with the exception that the bulk of the sequence recognised by the nicking enzyme (bracketed region in figure above) is synthesised *in-situ* by KF exo^- (green region). Since nicking can only occur after extension by a polymerase this may improve the cyclic behaviour of the system. The duplex can be nicked after only five incorporations but can potentially be extended by as many as seven nucleotides before the termination point, set this time, by withholding dCTP.

Oligo name	**Sequence (5’→3’)**	**T$_m$ °C (homodimer)**	**T$_m$ °C (complex)**
JACS thread	**B(PEG)$_8$AAAAAAAAAAAA CCGTTGTG CTT*CCC*TACAGTCAGTCAGTCGTATTA**	3.6	78.1
thread 2	**B(PEG)$_8$AAAAAAAAAAAACCGTTGTG≠ CAAAGATCCCTACAGTCAGTCGTATTA**	9.8	76.8
thread 3	**B(PEG)$_8$AAAAAAAAAAAAGAACCTCA ≠GCTT*CCC*TACAGTCAGTCAGTCGTATT**	-23.8	80.1
JACS primer 0	**TAATACGACTGACTGACTGTAGGGAAG**	1.2	78.1
primer 0	**TAATACGACTGACTGTAGGGATCTTTG≠**	1.2	76.8
primer 0*	**AATACGACTGACTGACTGTAGGGAAGC≠**	1.2	80.1

Figure 4.7 Comparison of melting temperatures for the rotaxane duplex sequences. The blue region shows where the JACS oligonucleotide sequence was changed to accommodate the recognition domain of Nb.BbvCI (underlined). The italicised CCC domain common to both the JACS oligo and the thread 3 was hoped to increase the stability of the rotaxanes.

Working once more from the thread sequence used in[6] and this time from the recognition domain of Nb.BbvCI a new thread and primer sequence, thread 3 and primer 0* were designed and screened iteratively with the Dinamelt webserver to check for correct duplex formation and competing secondary interactions (Figure 4.7).

4.6 Assembly of a thread 3 rotaxane & observation of ratcheted polymerase-driven power strokes

Stable, reproducible, rotaxanes could be formed routinely using the oligonucleotides that contained the Nb.BbvCI recognition sequence compared to the much less stable previous designs. This could have been due to improved retention of purine bases in the thread 3 compared to thread 2 owing to the shorter exposure to hydrolysing conditions and/or the presence of the CCC-GGG region in the duplex, but may have also been due to general improvement in experimental technique on the part of the researcher. A series of control nanopore experiments where the length of the primer in the rotaxane was varied were performed (Figure 4.8). The shapes of the *I*/*V* traces were similar to those seen in previous studies[6,7]. As described in Chapter One, the shape of the *I*/*V* curve is a result of the difference in size and charge density of PEG and DNA. As the primer length increases the average translational position of the thread strand is shifted upwards and the stem of the pore is occupied by an increasing ratio of PEG to DNA which results in a higher transmembrane ion current.

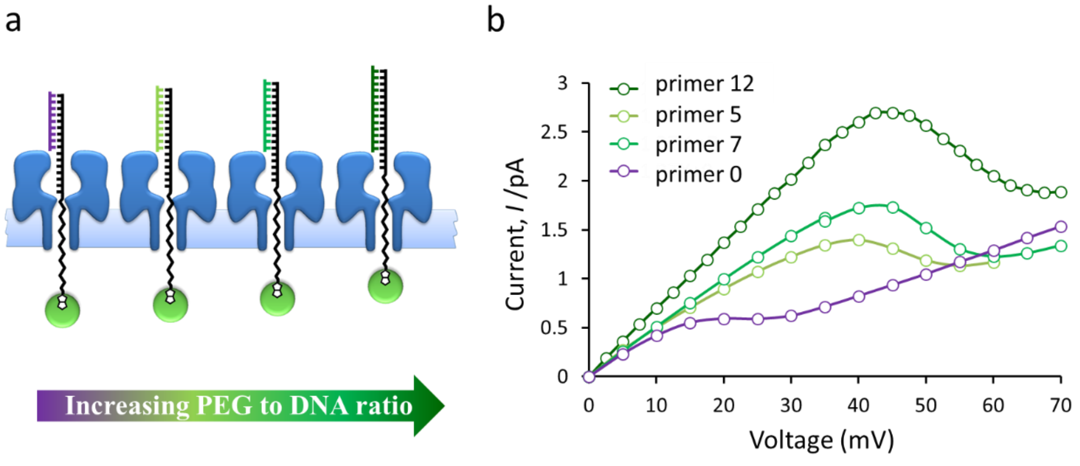

Figure 4.8 *I/V* curves for control rotaxanes. **a** Cartoon of rotaxanes formed from different length primers. **b** *I/V* curves of each rotaxane

The methodology used by Chu et al[7] to monitor nucleotide incorporations by KF exo$^-$ in real time was used to characterise the operation of the nanoactuator. Due to the detrimental effects on membrane stability of applying the +40 mV potential that was used in previous work, a potential of +25 mV was used for the present study. Ion currents were recorded continuously for periods of hours in 200 second sweeps, which were then concatenated to give long recordings. These long recordings were then rapidly scanned by eye to search for stepped increases in the current following KF exo$^-$ binding events (which themselves are denoted by transient spikes in the observed current). These events were then extracted and aligned end-to-end and adjusted for electrode drift, such that a clear picture of the movement of the thread due to the stepwise action of the enzymes could be obtained (Figure 4.9).

The power stroke half of the cycle from primer 0 to primer 0 was observed as shown in Figure 4.9c. Seven incorporations were observed over 40 minutes. Unfortunately, addition of Nb.BbvCI resulted in bilayer noise, and no nicking was observed during the two hour window before the bilayer ruptured.

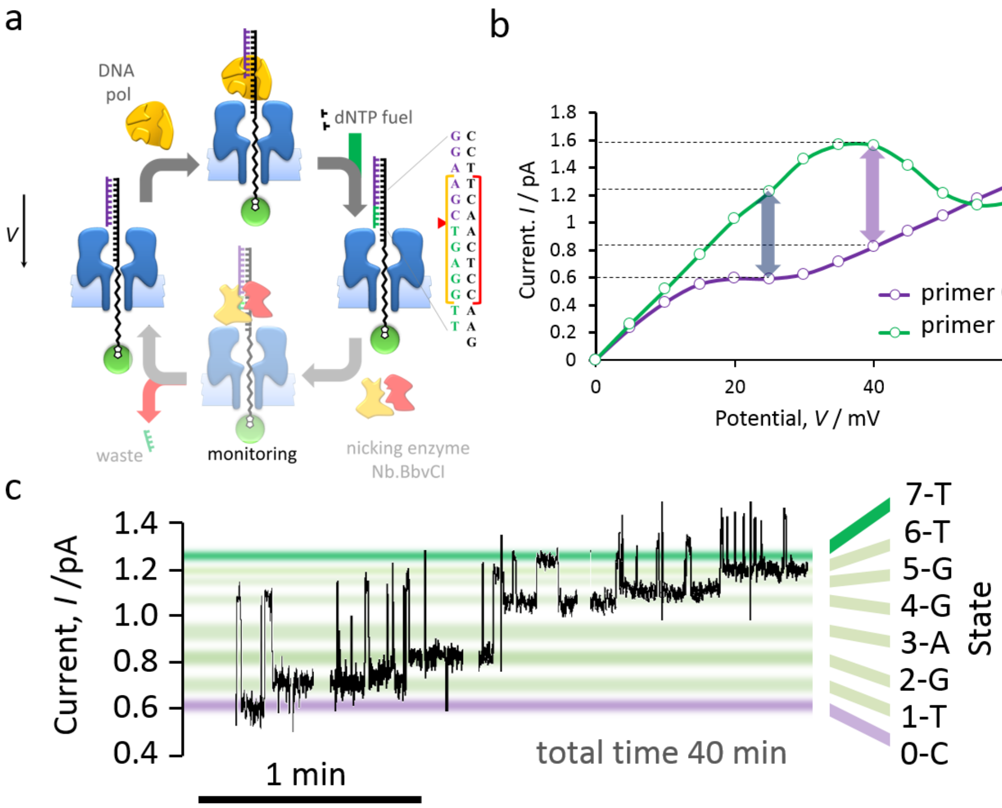

Figure 4.9 Observation of the power stroke part of the operation cycle using the Nb.BbvCI oligonucleotides. **a** A rotaxane was formed using thread 3 and primer 0. **b** The rotaxane was characterised using a stepped voltage protocol, the current range at 25 mV was ~ 0.6 pA (blue double arrow) compared to ~0.8 pA at 40 mV (purple double arrow). **c** After addition of KF exo⁻ to a final concentration of ~ 7 µM and dA/G/TTP (12 pmoles each) the current was recorded as a constant potential of 25 mV. The real-time ion current trace shows polymerase binding events and nucleotide incorporations.

4.7 Multiple rotaxanes to increase the chance of observing nicking

As demonstrated previously in Chapter Three, the likelihood of observing rare events such as nicking could potentially be increased by constructing multiple rotaxanes. Four rotaxanes were assembled concurrently and both enzymes and dNTPs were added at the same time. In the case of a single channel, the optimal applied potential to observe both enzyme binding and incorporation events is ~25 mV. However, the *I/V* trace in Figure 4.10b shows that the ideal potential for probing the states of the four-rotaxane system curve (4 RTX +0) is at ~70 mV due to change in the Boltzmann distribution of states. A continuous ion current recording at 70 mV revealed a series of events, with features 4, 5, and 7 that could be potential nicking events (Figure 4.10c). However, comparison with other similar enzyme binding events where incorporation did not occur suggests otherwise.

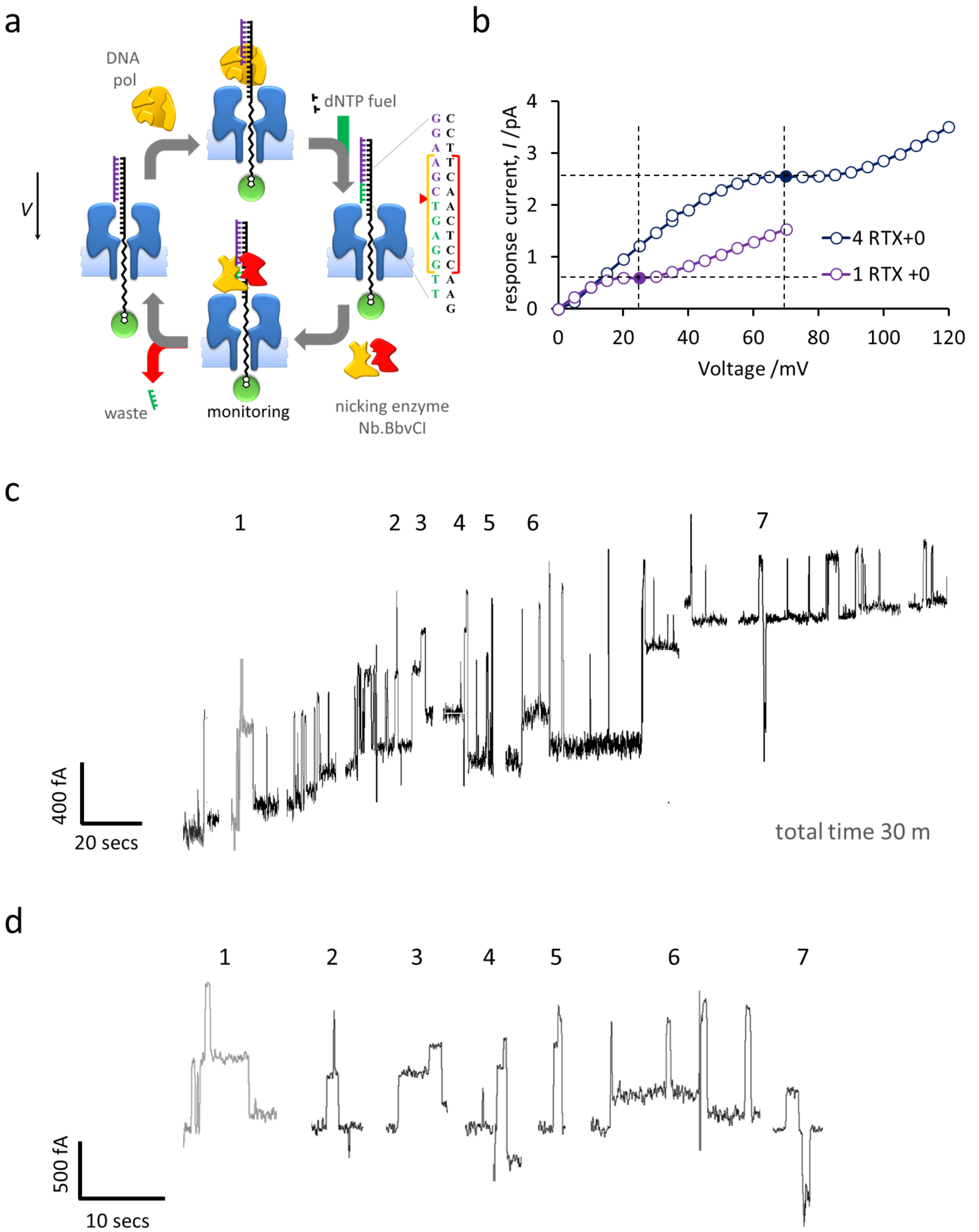

Figure 4.10 a, Four rotaxanes (RTX) are assembled concurrently with primer **0**. **b**, The initial *I/V* curve for the four rotaxanes compared with the initial *I/V* curve for one rotaxane from the previous figure. **c**, Current recording of four rotaxanes at a constant potential of 70 mV after the addition of KF exo$^-$, Nb.BbvCI and dNTPs (N = A,G,T). current levels are not assigned due to degeneracy between states composed of the summation of the distinct states of four rotaxanes **d**, unusual events which cannot be unambiguously assigned to nicking and may be instances of enzyme being bound to two rotaxanes concurrently

Most of the events 1→ 7 detailed in Figure 4.10 appear to be the result of consecutive or concurrent dissociations of KF exo⁻ from two different rotaxanes. Event 7 is most likely a channel gating event as the current returns to its initial level in a single step afterwards rather than in the stepwise fashion associated with nucleotide incorporation by KF exo⁻. However, the possibility remains that event 4 might correspond to nicking as the current after dissociation of the polymerase is lower than prior to association.

Although using multiple rotaxanes produced a signal that might have corresponded to a nicking event the result is ambiguous. Furthermore, the nicking events observed with the previous Nt.AlwI system had taken place at an applied potential of 40 mV, and the possibility remained that 25 mV was not sufficiently high to cause unzipping of the nicked seven base duplex region. A test experiment was conducted to establish the voltage range over which the seven base extension product could be unzipped from the assembled rotaxane (Figure 4.11).

4.8 Control experiment to investigate stability of nicked duplex

A rotaxane was assembled with thread 3 and primer 0 and characterised with a stepped voltage protocol 0 → 70 mV in 2.5 mV steps. Addition of extension +0→+7 resulted in a very clear change in the *I/V* curve observed due to its hybridisation to the thread strand (Figure 4.21b). The nicked duplex did not unzipped at applied potentials <22.5 mV, as shown by the new solid *I/V* curve. At potentials above 22.5 mV fluctuating ion current traces were observed that could be attributed to dissociation and reassociation of the short "nicked" sequence. Longer sweeps were performed at potentials from 25 → 40 mV in 2.5 mV steps to observe the real-time on/off binding events. Of most relevance to this project was the observation that the shorter strand dissociated from the duplex at 25 mV on a timescale of seconds. This proved that the obstacle to observing nicking was likely to be enzyme activity rather than undesirably high stability of the nicked duplex.

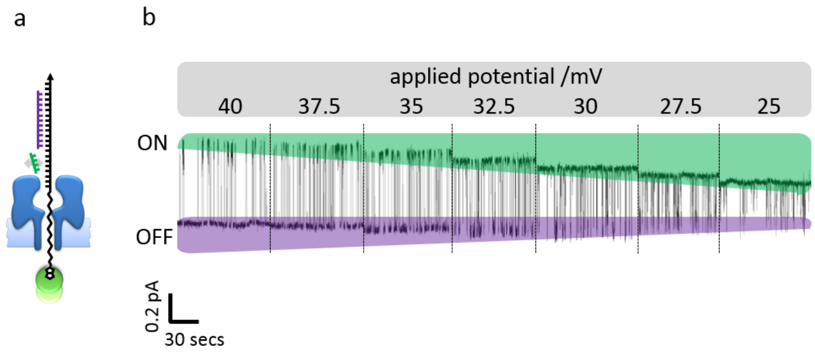

Figure 4.11 'Nicked strand' stability control experiment. This experiment also served as a control in the project discussed in Chapter Six and a more complete analysis of the data are presented there.

4.9 Real-time observation of complete operational cycles

Having ascertained that the stability of the nicked duplex was not impeding the operational cycle, it was decided to increase the quantity of nicking enzyme to increase the frequency of nicking events. However, when attempted this resulted in a gross increase in current and the eventual rupture of the bilayer. The nicking enzymes are supplied in a buffer containing dithiothreitol, glycerol and BSA, and it was reasoned that one or more of these additives may be contributing to bilayer instability. Thus, a sample of the commercially obtained Nb.BbvCI (100 µL) was mixed with 650 µL of molecular biology grade water and dialysed through a membrane of 7000 M.W. cut-off against 500 mL of HPLC grade water for ~18 hours at room temperature. The protein was then concentrated *in vacuo* at 1000 rpm at 70 ^{0}C. The dialyzed enzyme was then used in subsequent attempts to observe the full cycle of operation in nanopore experiments.

Figure 4.12a shows a real-time current trace using this dialysed nicking enzyme. Over a period of 108 minutes, 24 incorporations and three nicking events were observed amounting to nearly four full cycles of operation. Figure 4.12b shows the saw-tooth ratcheted behaviour of the rotaxane by plotting the average current of each step in sequence. Figure 4.12c shows the ratcheted potential energy surface generated by repetitive cycles of dNTP fuelled polymerisations and nicking enzyme catalysed sequence specific DNA hydrolysis.

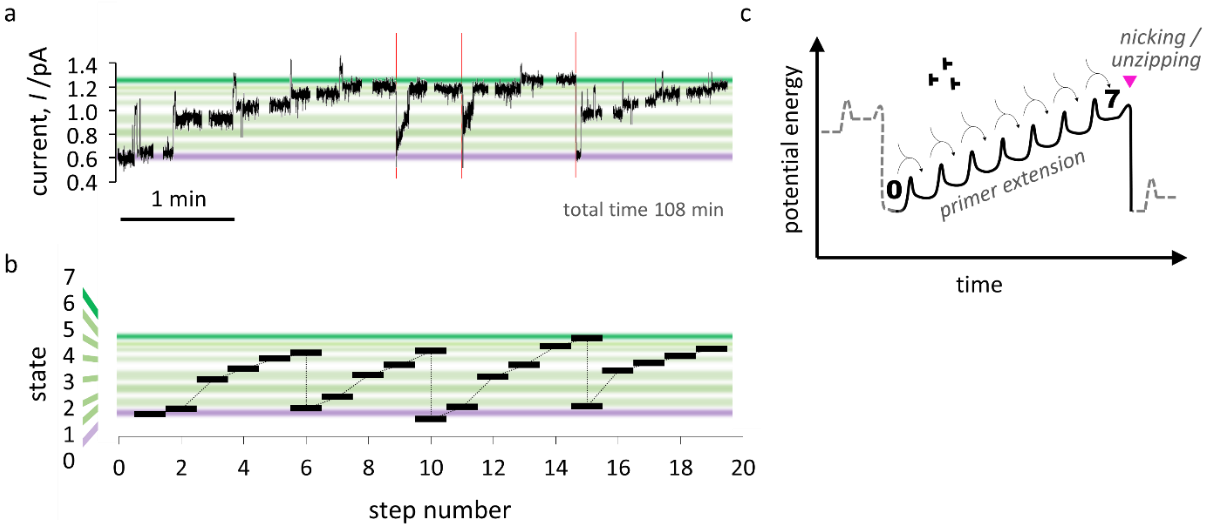

Figure 4.12 Observation of almost four complete cycles of operation. The rotaxane was assembled using primer 0. **a** Real-time current recording showing almost four cycles composed of 24 incorporations and three nicking events. **b** The average current in each state clearly show the expected ‘saw-tooth’ pattern characteristic of a ratcheted cycle of operation. **c** temporally asymmetric ratcheted potential energy surface resulting from operation of the nanoactuator.

4.10 Future work

A few additional attempts with the present system would result in a sufficient data for publication of a synthetic transmembrane reciprocating nanoactuator. However, the initial goal of the project was to develop a system that exhibited an asymmetric operational cycle on the timescale of milliseconds such that work could be extracted in the form of driven transport of analytes across the membrane, which ultimately might be capable of generating a transmembrane potential. The major bottleneck to achieving these ambitious goals with the present system seems to be the low activity of the nicking enzymes employed thus far.

One of the simplest ways of overcoming the low relative activity of Nb.BbvCI compared to KF exo$^-$ polymerase might be to increase the concentration of magnesium used, or to replace magnesium with a more catalytically active metal such as manganese, some precedent exists for improved catalytic activity of DNA processing enzymes with manganese ie. circularisation-ligation of ssDNA by circ ligase[12].

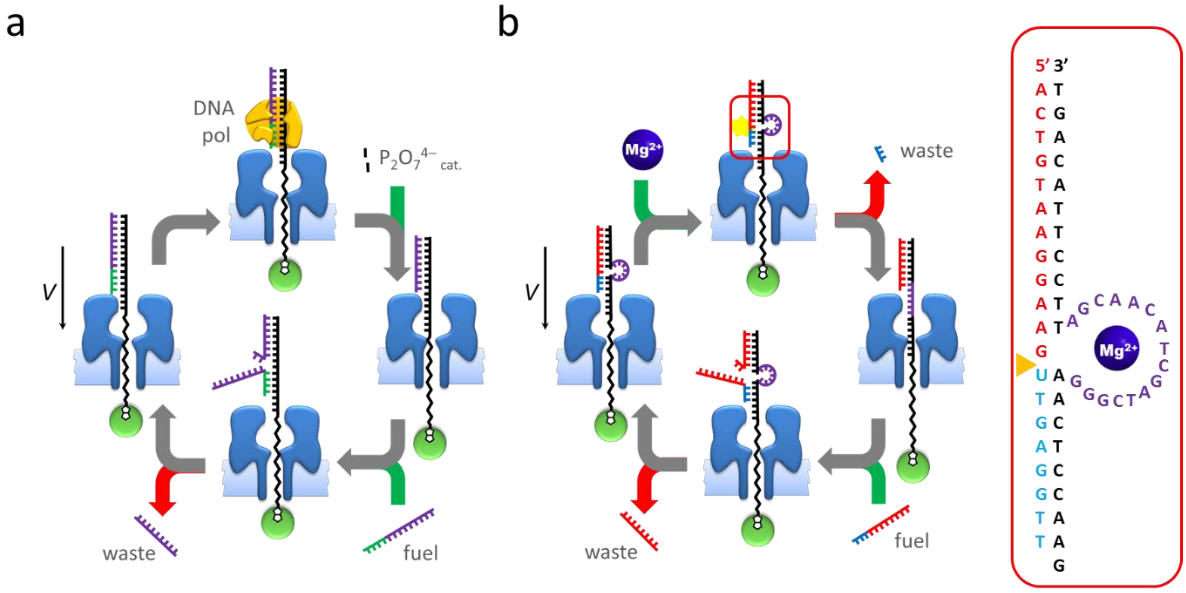

Figure 4.13 Schematic for a reciprocating nanoactuator based on **a**, strand displacement and pyrophosphorolysis. **b**, an RNA-cleaving DNAzyme. The blue/red strand is a DNA/RNA hybrid primer. The thread sequence is adapted from the current Nb.BbvCI actuator sequence to include the 15-nucleotide, RNA-cleaving motif shown in the expansion (red box)

Another approach might be to take advantage of the pyrophosphorolysis reaction that was explored in Chapter 3. In the design depicted in Figure 4.13a, a rotaxane is assembled with thread 3 and primer 7. The DNA polymerase KF exo$^-$ and Na_4PP_i would be added causing pyrophosphorolysis to occur at the 3’ OH of the primer oligonucleotide. Shortening of the primer by pyrophosphorolysis would reveal a toehold on the thread to which primer 7 could bind and strand displace the degraded primer thereby restoring the system to its initial condition. Experimental conditions such as the applied potential could be tuned such that a specific number of pyrophosphorolysis events were required to drive a cycle of the device. A variation of this design could employ an exonuclease enzyme in place of the DNA polymerase.

A more radical approach might be to employ a ‘DNAzyme’ such as that developed by He[13] as part of the work cycle of a transmembrane machine. In the system depicted in Figure 4.13b, the thread strand includes a loop that catalyses the hydrolysis of a specific G – U phosphodiester bond in an RNA primer. The turnover frequency of this DNAzyme sequence has been demonstrated on the timescale of minutes. Indeed, studies in which nicking DNAzymes are used in systems initially designed around nicking enzymes are common[14].

4.11 Conclusions

A transmembrane DNA/PEG▪α-HL rotaxane system was used in the first demonstration of one of the key properties of transmembrane molecular machines – hysteretic cyclical behaviour in the mechanical motion of the synthetic transmembrane component. The project met with difficulties owing to poor stability of the rotaxane system which necessitated a number of alterations from the initial design. Many configurations were tested before one was reached that allowed observation of the desired cycle of operation. The initial goal of the project to build a reciprocating nanoactuator that could be used as a prototypical transmembrane pump was not realised, owing in part to the poor efficiency of the nicking enzymes employed. Nonetheless, the experimental methodology was developed to an extent whereby most days of nanopore experimentation yielded usable results. It is envisaged that a few more attempts will provide sufficient results for publication. Two further experimental configurations to address the bottleneck in the operational cycle were postulated.

4.12 Materials and Methods

M4.1 Oligonucleotide syntheses & enzymatic assembly

Standard solid phase DNA synthesis involving coupling between phosphoramidite analogues of the deoxynucleotides dA, dC, dG and dT often proceeds with a coupling efficiency >99% with high sequence fidelity. However, over the course of a long synthesis the overall yield drops significantly and sequence fidelity also suffers. In addition, the biotin and PEG spacer phosphoramidites exhibit much lower coupling efficiencies, and since they come at the end of the synthesis, the final yield of the PEGylated sequences is heavily affected. Two synthetic strategies were employed in initial syntheses of the thread strand (thread 1) in an attempt to circumvent the low coupling efficiencies of the modifier phophoramidites. As shown in Figure M4.1, the sequence of the thread was modified to include seven rather than eight PEG units, with the disparity in the length of the oligo being made up by inclusion of three extra dA nucleotides. Secondly, a ligation assembly strategy was used to attempt to increase the yield. The thread 1 oligo was hence synthesised in three fragments thread a, thread b and thread c which were synthesised in-house and purified by two stage RP-HPLC while all costrands and splints were bought from Invitrogen with desalt purification. The modular assembly also permits scope for creating other highly modified oligos for different applications by ligating an easily synthesised or bought unmodified sequence to the expensive and synthetically challenging 5'-biotin and PEG-modified thread a.

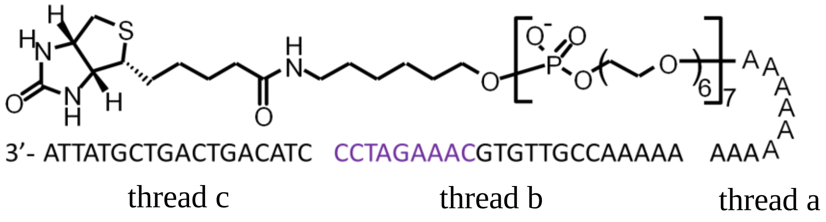

Figure M4.1 Structure of the thread 1 fragmented into three segments thread a, thread b and thread c. The purple region indicates the recognition sequence for the nicking enzyme Nt.ALwI

As in the initial redesign of the thread sequence, the oligo sequences required for enzymatic assembly of the thread 1 strand were screened using the webserver DinaMelt[9] to check that the melting temperatures of the desired duplexes were higher than those of any undesired interactions between the components (Figure M4.2). This was done to ensure that the ligation reactions would proceed as desired without the formation of undesired impurities that would complicate the isolation and downstream processing of the assembled thread strand. The desired duplexes all form at room temperature and undesired ones do not. In addition, the melting temperatures of the duplexes formed by the counter strands and the splints are the highest meaning that the completed thread 1 can be isolated in solution from the splint strands. The sequence fidelity and purity of the thread strand is guaranteed by the use of shorter RP-HPLC purified oligonucleotides, which will contain fewer errors than the full-length thread. Primer 0 and primer 8 were purchased from Sigma with desalt purification.

Species	thread a	thread b	thread c	splint 1	splint 2	co-strand 1	co-strand 2
thread a	9.1				▓	= strong enough	
thread b	-149.9	9.8			░	= weak enough	
thread c	-120.2	-18.1	-14.8				
splint 1	▓ 28.3	▓ 59.5	-8.9	8.4			
splint 2	18.2	▓ 43.2	▓ 40.6	-24.0	10.8		
co-strand 1	-149.9	8.8	-8.9	▓ 69.3	18.2	33.2	
co-strand 2	-273.1	1.5	-27.5	13.8	▓ 71.5	-23.1	4.4

Figure M4.2 Comparison of calculated melting temperatures in °C for oligonucleotides used in the enzymatic assembly of thread 1.

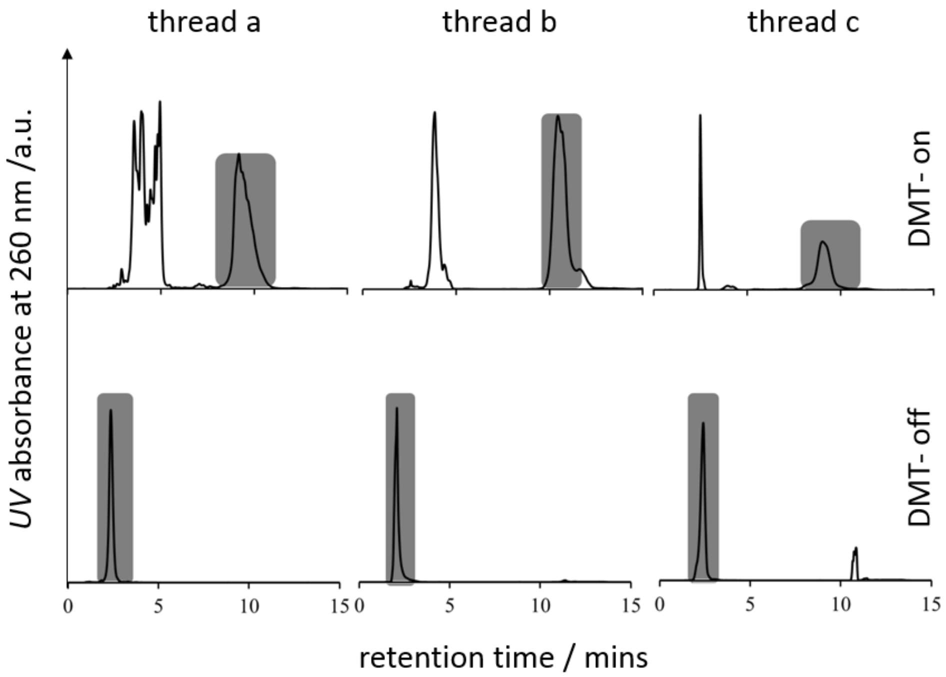

Figure M4.3 HPLC traces of synthesised fragments of thread 1 DMT-off. Manual fraction collection (shaded regions) permitted the exclusion of shoulder peaks. The small residual peak in the DMT off trace for thread c at ~ eleven minutes is due to incomplete detritylation of the recovered DMT protected oligo thread c.

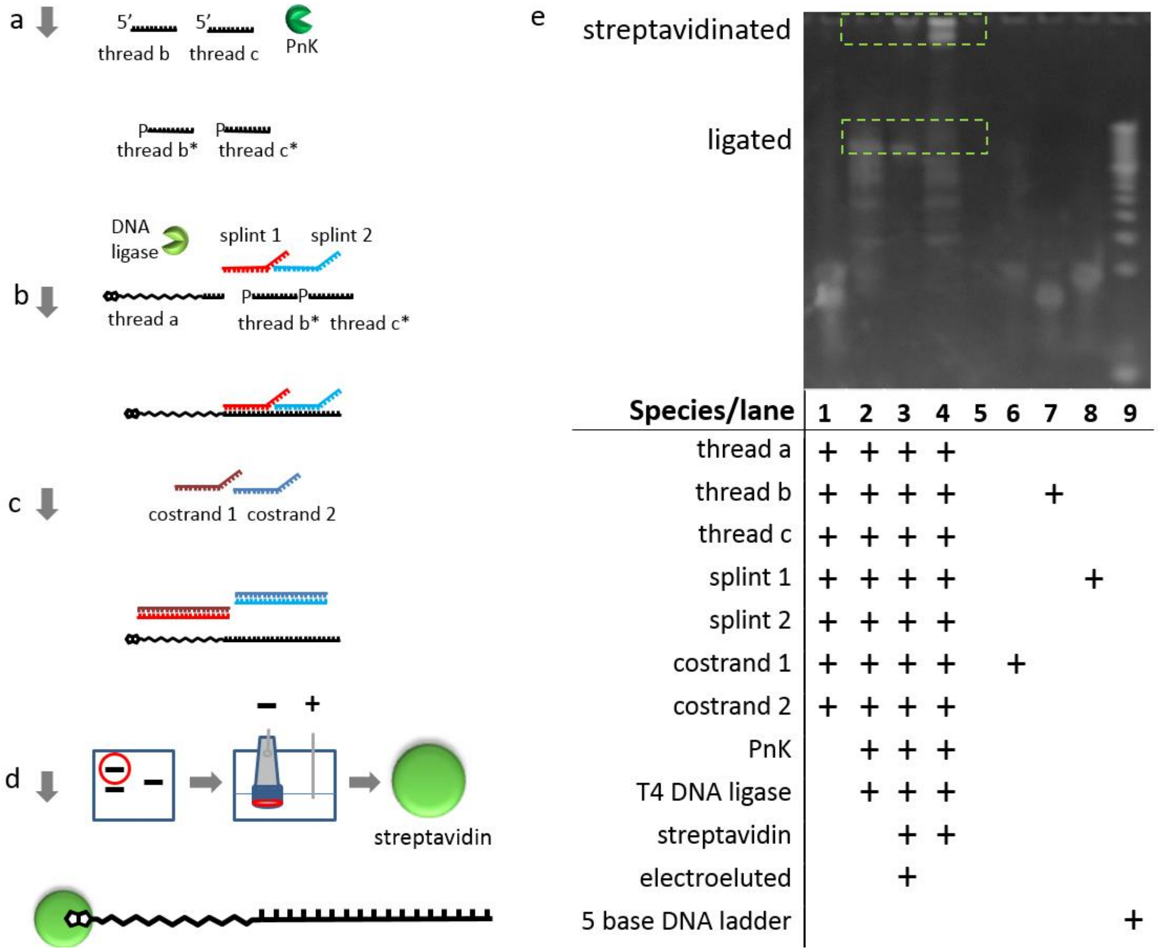

Species/lane	1	2	3	4	5	6	7	8	9
thread a	+	+	+	+					
thread b	+	+	+	+			+		
thread c	+	+	+	+					
splint 1	+	+	+	+				+	
splint 2	+	+	+	+					
costrand 1	+	+	+	+		+			
costrand 2	+	+	+	+					
PnK		+	+	+					
T4 DNA ligase		+	+	+					
streptavidin			+	+					
electroeluted			+						
5 base DNA ladder									+

Figure M4.4 The thread sequence was synthesised in three short parts, thread a, thread b and thread c. **a**, the 5' ends of thread b and thread c were phosphorylated using polynucleotide kinase (3U) at 37 ˚C in a total reaction volume of 50 μL. **b**, templated for ligation using complementary splint strands splint 1 and splint 2, which aligned the thread strands in the correct order and ligated with T4 DNA ligase which coupled the adjacent 5' phosphate and 3' hydroxyl groups together. 1.1 equivalent of each thread strand and one equivalent of each splint were used with 3U of ligase in a total reaction volume of 50 μL **c** The splint strands both contained toehold regions which allowed their displacement from the thread strand using fully complementary sequences. **d** PAGE was carried out and the band corresponding to the ligated thread was identified by brief illumination by shortwave UV 254 nm and excised from the gel using a clean scalpel. **e** The full-length oligonucleotide was isolated from the acrylamide matrix by electroelution before being complexed with Streptavidin **f**, ready for use in nanopore experiments. **g** The correct length, pure, biotin-containing oligonucleotide can clearly be seen in lane three of the analytical PAGE which was run at 120 V for 2 hours on a 15% TBE 7 M urea gel.

The enzymatic assembly of thread 1 involved the use of two enzymes, polynucleotide kinase (PnK) and T4 DNA ligase. PnK catalyses the transfer of the terminal phosphate group from a molecule of ATP to the 5' end of an oligonucleotide. DNA ligases usually catalyse the coupling reaction between adjacent 5'-phosphate and 3'-hydroxyl ends in nicked duplexes. In this case, two splint strands template the single adjacent 5'- phosphate and 3'- hydroxyl ends of threads a,b and c in two distinct duplex regions and the DNA ligase catalyses the coupling of each phosphate to its adjacent hydroxyl group (Figure M4.4).

M4.2 Synthesis and characterisation of thread 2

Thread 2 was synthesised by standard oligonucleotide synthesis and purified by two-step RP-HPLC. Thread 2 was combined with streptavidin in a five to one ratio. The complexation of thread 2 with streptavidin was confirmed by PAGE (Figure M4.5), and this streptavidinated DNA was used without further purification in nanopore experiments.

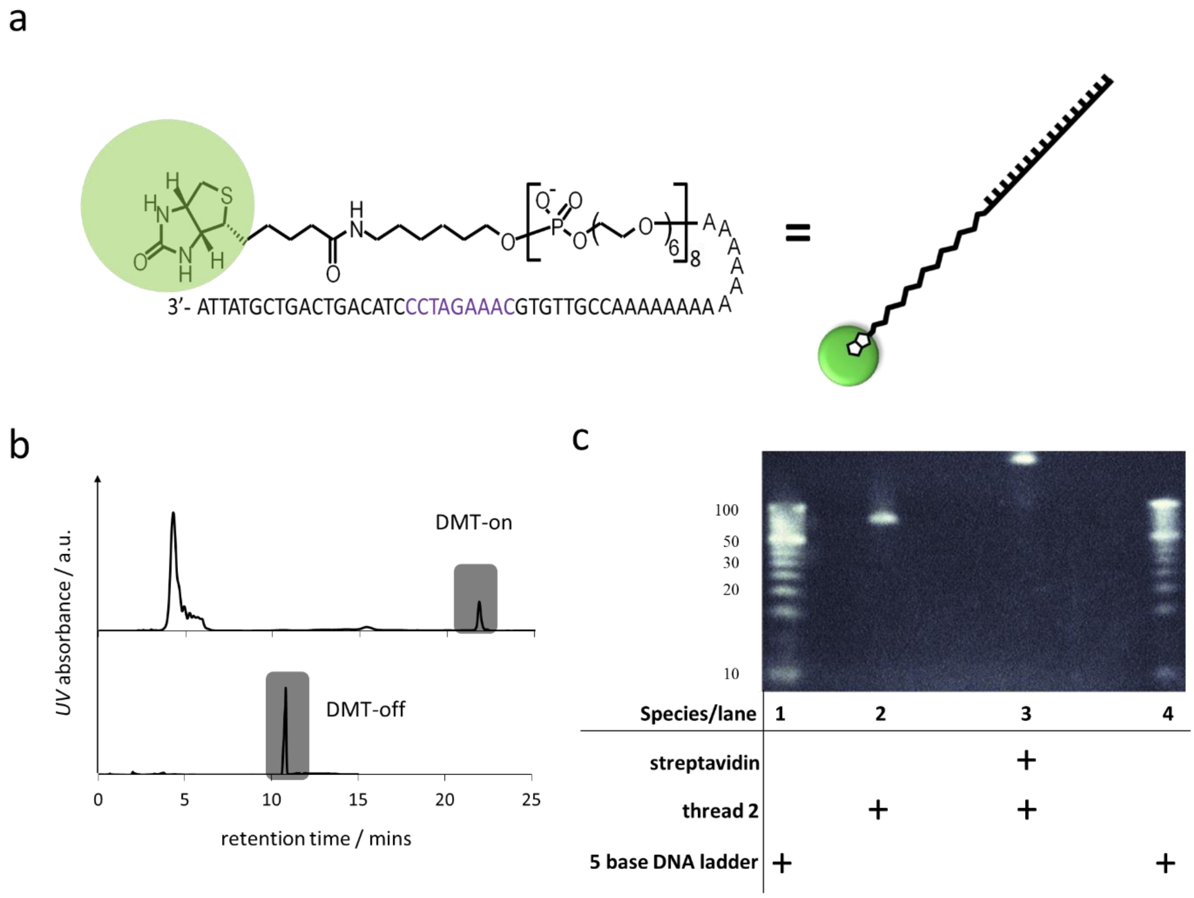

Species/lane	1	2	3	4
streptavidin			+	
thread 2		+	+	
5 base DNA ladder	+			+

Figure M4.5 Structure and characterisation of thread 2. **a** Structure of thread 2, the recognition domain for Nt.AlwI is shown in purple. **b** HPLC chromatograms of thread 2, collected peaks are highlighted in green. **c** Schematic and PAGE [10 % TBE, 7M urea gel run at 120 V for 2 hours] of streptavidination of thread 2, the retardation of gel shift resulting from complexation with streptavidin is clearly visible.

M4.3 Synthesis and purification of thread 3

The thread 3 oligonucleotide was synthesised by standard solid-phase DNA synthesis. Primer 0 was purchased from Sigma with desalt purification and reconstituted to 300 μM, 5 mL was used per experiment. To minimise the risk of depurination by overly long exposure to acid conditions the synthesis of thread 3 was performed DMT-off. By this approach, the DMT group was removed from the biotin by brief exposure to triiodoacetic acid by the DNA synthesis in the course of the automated DNA synthesis. The full-length biotinylated oligonucleotide was successfully purified using a shallow RP-HPLC gradient since biotin acts like a hydrophobic purification tag compared to the polar terminal OH groups present on unwanted truncated sequences. As this was the first time that separation had been attempted in this way, all the peaks were collected to be screened by PAGE to ensure that the correct oligonucleotide was not inadvertently disposed of.

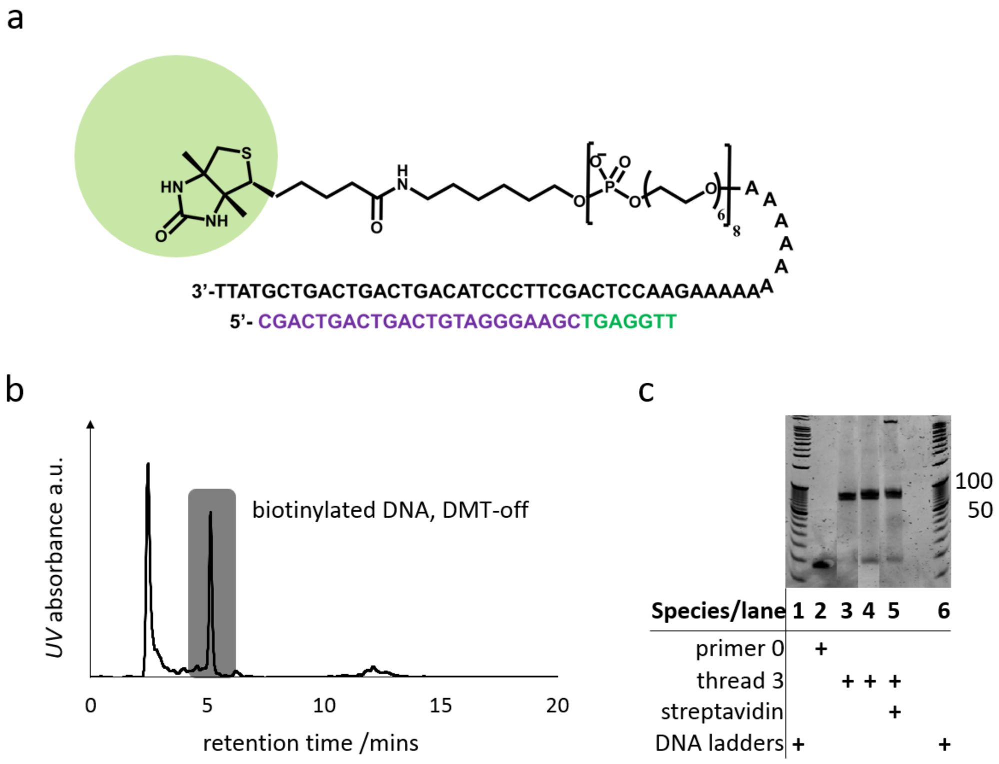

Species/lane	1	2	3	4	5	6
primer 0		+				
thread 3			+	+	+	
streptavidin					+	
DNA ladders	+					+

Figure M4.6 Thread 3 and corresponding primer 0. **a** Structure of thread 3 bound to streptavidin, although streptavidin is teteravalent and actually binds four thead strands only one is shown for clarity. **b**, HPLC chromatogram of runs of primer 0. **c** Scheme of confirmatory interactions screened. **d** PAGE analysis of recovered fractions [12% acylamide, 7 M urea, run for 2 hours at 120 V, T2 was found to be the full length, complementary, biotinylated strand.

4.4 Confirmation of Nt.AlwI nicking enzyme activity

Prior to conducting nanopore experiments it was first necessary to confirm the activity of Nt.AlwI in the buffer in which KF exo$^-$ is known to be competent, and which nanopore ion current recordings can be performed. The buffer supplied with Nt.AlwI by the manufacturer contains a different composition and concentration of ions in addition to bovine serum albumin (BSA) which is not present in our usual nanopore buffer. Since the nanopore experiment is very sensitive, major changes to the composition of the buffer should be avoided.

Buffer	Monovalent Salt	Tris base anion	Magnesium source	Additives
NEB Cutsmart	KOAc 50 mM	OAc^- 25 mM pH 7.9	$Mg(OAc)_2$ 10 mM	BSA 100 µg/mL
KF exo$^-$ nanopore	KCl 150 mM	Cl^- 25 mM pH 8	$MgCl_2$ 4.5 mM	N/A
Nanoactuator buffer	KCl 150 mM	Cl^- 25 mM pH 8	$MgCl_2$ 10 mM	N/A

Figure M4.5 Comparison of compositions of Nt.AlwI and KF exo$^-$ nanopore buffers

Reasoning that the higher concentration of magnesium would result in optimal activity of Nt.AlwI without having a deleterious effect on the activity of KF exo$^-$ (NEB's proprietary polymerase buffers also contain 10 mM $Mg(OAc)_2$, it was decided to use 10 mM $MgCl_2$. It was also decided not to use BSA, not to change the identity of the anions from chloride to acetate and not to change the concentration of monovalent salt from 150 mM to 50 mM as this would worsen the signal-to-noise ratio in the ion current recordings. A lower signal-to-noise ratio might make it more difficult to distinguish different states of the system. The nicking enzyme was then screened for activity in the new 'nanoactuator buffer'. To ascertain whether the rate of nicking by Nt.AlwI would be comparable to the polymerase activity of KF exo$^-$, a time-course experiment was run using a model reaction (Figure 4.6). An unmodified 46 base oligonucleotide containing the same sequence as thread 1 was used (template). 1.1 equivalents of template was combined with 1 equivalent of a 40-base complementary strand (primer), which when nicked would give two 20mer ssDNAs. 1 µL samples were taken from the test reaction (starting volume 50 µL) at regular intervals and added to a large excess (3 µL) of gel-loading dye. This dye mixture contains a high concentration of EDTA which sequesters magnesium ions in the sample, ceasing the enzyme activity from that point on. To each sample was then added a costrand (2 equivalents) that was fully complementary to the template and thus displaced the nicked and un-nicked primer strands from the template allowing them to be visualised by PAGE. The appearance of faint bands in lanes 3 to 7 of Figure M4.6 that have the same gel shift as the 20mer control strands showed that Nt.AlwI operates on a reasonable timescale in the nanoactuator buffer.

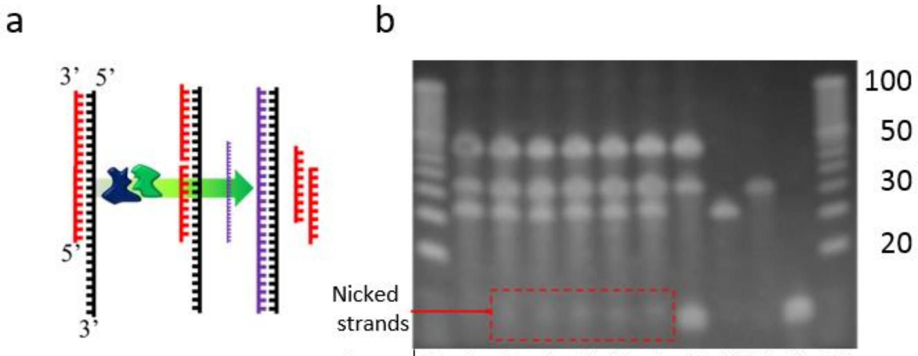

Species/lane	1	2	3	4	5	6	7	8	9	10	11	12
time /mins		0	15	30	60	90	120					
Nt.AlwI			+	+	+	+	+	+				
primer		+	+	+	+	+	+	+	+			
template		+	+	+	+	+	+	+		+		
control a								+			+	
control b								+			+	
costrand		+	+	+	+	+	+	+				
5 base DNA ladder	+											+

Figure M4.6 Schematic of the Nt.AlwI test reaction. **a** The 40 nucleotide primer (red strand) is hybridised to the template (black strand). Nt.AlwI (blue and green) nicks the primer giving the nicked duplex (two shorter red strands) bound to the template. Addition of the costrand (purple) displaces the nicked duplex by toehold binding and three-way branch migration giving the full length duplex and 20mer nicking products. **b** confirmation of Nt.AlwI activityby PAGE 12% TBE 7M Urea gel

4.9 Confirmation of Nb.BbvCI nicking enzyme activity

In contrast to Nt.AlwI, the supplier recommends that nicking reactions performed with Nb.BbvCI should employ 12 mM magnesium acetate (rather than 10 mM). The effect of magnesium concentration on the activity of the nicking enzymes was examined on test DNA substrates under different conditions (Figure M4.7). The increased intensity of the band corresponding to the nicked product in lanes 2 to 5 showed that higher magnesium acetate concentrations promoted the activity of Nb.BbvCI. The nanopore buffer was subsequently changed to include 12 mM $Mg(OAc)_2$, as it was anticipated that this would have no deleterious effect on the activity of the DNA polymerase KF exo⁻, the stability of the bilayer, or the correct folding and insertion behaviour of α-HL.

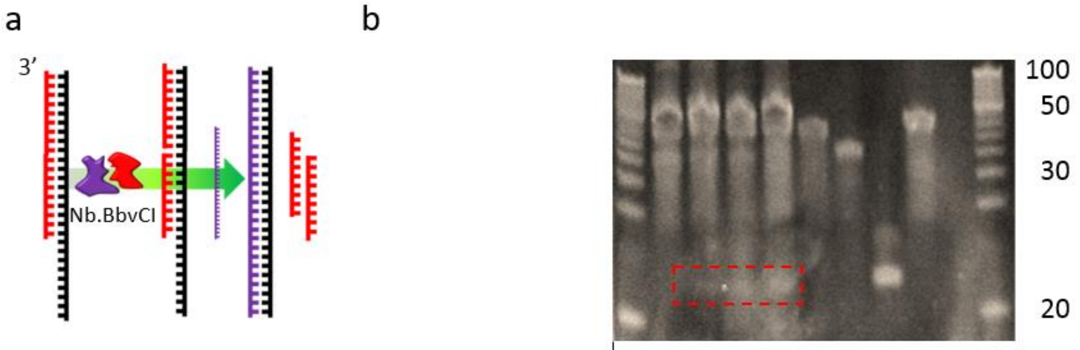

Species/lane	1	2	3	4	5	6	7	8	9	10	11
$Mg(OAc)_2$ mM		0	4.5	10	12						
Nb.BbvCI		+	+	+	+	+					
template		+	+	+	+	+					
primer		+	+	+	+	+		+			
control a and b							+				
5 base DNA ladder	+										+

Figure M4.7 Effect of magnesium concentration on nicking activity of Nb.BbvCI. PAGE was performed on a 12% TBE 7M Urea gel

Electrical Measurements

Single-channel ion current recordings of transmembrane rotaxanes. A single channel was obtained in a suspended bilayer according to the general procedure outlined in Chapter Two of the present work. The buffer used in the final nanoactuator experiment contained KCl [150 mM], Tris-HCl [25 mM] and $Mg(OAc)_2$ [12 mM]. A rotaxane was prepared in the following general manner. The streptavidin-capped 5’-biotinylated DNA-PEG copolymer thread strand was added to the live well to a final concentration of ~100 nM. DNA primer 0 was added to a final concentration of ~2.5 μM to the ground well of the experimental cell. The thread strand was captured by applying a transmembrane potential of –140 mV until a reduction in the transmembrane current (from ca. –18 to –5pA at –140 mV) was observed that corresponded to a capture. The potential was then reduced to –28 mV to allow the primer to hybridize to the 5’-end of the thread protruding through the pore into the ground well for ~eight minutes, thereby forming the desired rotaxane. The rotaxane was characterized by applying potential sweeps in 5 mV steps, each of 2 second duration across a 70 mV range, from 0 to +70 mV, giving characteristic *I/V* profiles e.g. Figure 4.7b. After confirmation of a rotaxane assembled using primer 0, the following were added to the ground well: DNA polymerase KF exo^{-} (NEB) [~7 nM], deoxynucleotide triphosphates (dNTPs, for the experiments involving Nb.BbvCI, N = A, G, T) (Bioline) [~12 μM] each and the nicking enzyme Nb.BbvCI (NEB) [~7 nM]. A constant transmembrane potential of +25 mV was applied and the ion current was recorded. The data were then filtered to 10 Hz after acquisition using an eight-pole Bessel filter.

4.13 References

1. Kusters, I.; Driessen, A. J., SecA, a remarkable nanomachine. *Cellular and molecular life sciences : CMLS* **2011,** *68* (12), 2053-2066.
2. Green, S.; Bath, J.; Turberfield, A., Coordinated chemomechanical cycles: A mechanism for autonomous molecular motion. *Phys. Rev. Lett.* **2008,** *101* (23).
3. Chen, I.; Christie, P. J.; Dubnau, D., The ins and outs of DNA transfer in bacteria. *Science* **2005,** *310* (5753), 1456-1460.
4. Efremov, R. G.; Baradaran, R.; Sazanov, L. A., The architecture of respiratory complex I. *Nature* **2010,** *465* (7297), 441-445.
5. Noji, H.; Yasuda, R.; Yoshida, M.; Kinosita, K., Direct observation of the rotation of F1-ATPase. *Nature* **1997,** *386* (6622), 299-302.
6. Cockroft, S. L.; Chu, J.; Amorin, M.; Ghadiri, M. R., A single-molecule nanopore device detects DNA polymerase activity with single-nucleotide resolution. *J. Am. Chem. Soc.* **2008,** *130* (3), 818-820.
7. Chu, J.; González-López, M.; Cockroft, S. L.; Amorin, M.; Ghadiri, M. R., Real-time monitoring of DNA polymerase function and stepwise single-nucleotide DNA strand translocation through a protein nanopore. *Angew. Chem. Int. Ed.* **2010,** *49* (52), 10106-10109.
8. Kiesling, T.; Cox, K.; Davidson, E. A.; Dretchen, K.; Grater, G.; Hibbard, S.; Lasken, R. S.; Leshin, J.; Skowronski, E.; Danielsen, M., Sequence specific detection of DNA using nicking endonuclease signal amplification (NESA). *Nucl. Acid. Res.* **2007,** *35* (18), e117.
9. dinamelt. http://mfold.rna.albany.edu/?q=dinamelt.
10. Duan, R.; Zuo, X.; Wang, S.; Quan, X.; Chen, D.; Chen, Z.; Jiang, L.; Fan, C.; Xia, F., Quadratic isothermal amplification for the detection of microRNA. *Nat. Prot.* **2014,** *9* (3), 597-607.
11. Bath, J.; Green, S. J.; Turberfield, A. J., A free-running DNA motor powered by a nicking enzyme. *Angew. Chem. Int. Ed.***2005,** *44* (28), 4358-4361.
12. Shroff, H.; Sivak, D.; Siegel, J. J.; McEvoy, A. L.; Siu, M.; Spakowitz, A.; Geissler, P. L.; Liphardt, J., Optical measurement of mechanical forces inside short DNA loops. *Biophys. J.* **2008,** *94* (6), 2179-2186.
13. He, Y.; Liu, D. R., Autonomous multistep organic synthesis in a single isothermal solution mediated by a DNA walker. *Nat. Nanotechnol.* **2010,** *5* (11), 778-782.
14. Wang, F.; Freage, L.; Orbach, R.; Willner, I., Autonomous replication of nucleic acids by polymerization/nicking enzyme/DNAzyme cascades for the amplified detection of DNA and the aptamer–cocaine complex. *Anal. Chem.* **2013,** *85* (17), 8196-8203.

Chapter Five

A transmembrane DNA rolling circle amplifier

Abstract

Chapter Five develops the idea of cyclical behaviour as a defining feature for true molecular machines and employs a continuation of the nanopore rotaxane approach to investigate a different synthetic transmembrane system. A rotaxane is constructed using the same thread 3 strand as used in Chapters Three and Four, but this time using a circularised strand to form the duplex region with the thread. The circular strand lacks a 3’-OH end to ‘prime’ a DNA polymerase and extension is therefore primed and takes place at the 3’-OH end of the thread strand instead. The thread is translocated through the pore by the electric field at a rate determined by the polymerase’ nucleotide incorporation, while the enzyme tracks around the rotating circular strand. The current through the pore is recorded at a constant potential and changes in a repetitive way that is proposed to depend on the identity of the base in the recognition domain of the pore and corresponds to amplification/extrusion of a DNA transcript. The approach allows the operation of the mechanical cycle to be monitored in real time. The implications for single molecule DNA sequencing using the system are discussed.

5.1 Introduction

Rolling circle amplification (RCA) is a process utilised in the replication of genomic or plasmid DNA by some simple organisms, one notable example being *Bacillus subtilis* bacteriophage phi 29[1]. The natural process involves the synthesis of DNA by specific polymerases from small circular DNA templates and is often self-primed by the polymerase[2] rather than a short duplex region of DNA. Extension proceeds until the polymerase approaches the existing duplex region, thereafter the extending strand continually displaces the duplex region as it is synthesised (rolling circle amplification). This process results in a very long (hundreds of nanometres to microns) single-stranded DNA containing a repeat sequence that is the reverse complement, or DNA transcript, of the initial circle[3].

The robust and simple nature of the mechanism have meant that RCA has been adapted for use in many applications, from ultra-sensitive diagnostics that can geometrically amplify very low copy number DNA samples in a clinically useful time at room temperature[4], to the templating of one-dimensional plasmonic nanomaterials[5], proteins[6], as well as in the construction of DNA-based molecular machines[7]. Phi 29 is the most commonly used polymerase in artificial RCA and has also been used previously in nanopore experiments[8] owing to its high salt tolerance, which allows for a good signal-to-noise ratio in single-molecule experiments. In addition, the high processivity of this enzyme affords multiple observations of incorporation events and reduces fluctuations that might arise from on/off binding events. Indeed, phi 29 is perhaps the enzyme being employed by the Oxford Nanopore group in their α-HL based next generation DNA sequencing platform. To our knowledge the work in the present chapter is the first successful demonstration of direct, real-time, single-molecule rolling circle amplification (RCA) through an α-HL nanopore.

5.2 Design of a transmembrane rotaxane to monitor rolling circle amplification at the single-molecule level

Rolling circle amplification with phi 29 polymerase provides an ideal process to interface with the previously described nanopore-rotaxane approach to develop new synthetic transmembrane molecular machines. The following design can be considered as a nanomechanical mimic of biological membrane signal transduction, or DNA-transfer processes such as bacterial conjugation[9],[10]. The proposed artificial system recognises a circular ssDNA and uses RCA to extrude an ssDNA transcript of the sequence information through the nanopore to the opposite side of the bilayer.

The system shown in Figure 5.1 is assembled using the previously introduced thread strand, but with the exception that the complementary strand is pre-circularised. Phi 29 Polymerase is used in preference to KF exo^{-} as it has higher processivity. The cyclical behaviour of the system is embodied in the unidirectional rotation of the circular strand as the ssDNA transcript unreels through the pore. The unreeling of the ssDNA transcript is driven by the electric field and the strand-displacement activity of the polymerase. The system satisfies other criteria of being a true molecular machine in that it operates autonomously, consuming dNTP fuel, undergoing cycles of rotation and generating a long ssDNA product. Successful operation of the device may also be confirmed by the detection of the ssDNA product using RCA amplification strategies previously reported in the literature[4].

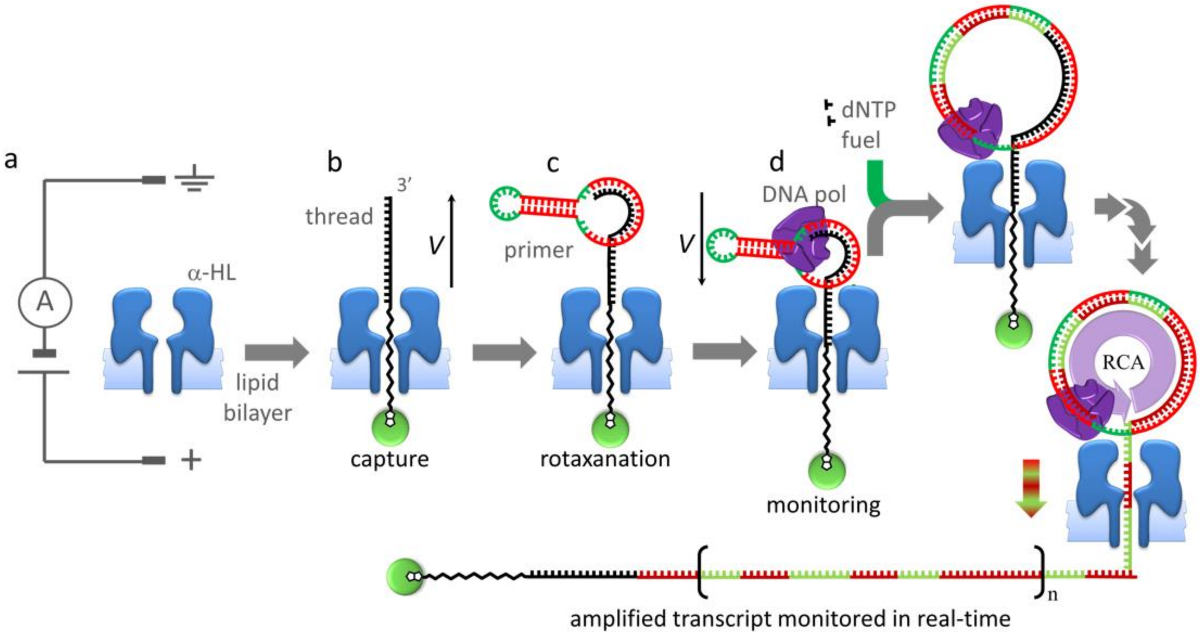

Figure 5.1 Schematic of the assembly and operation of the single-molecule rolling-circle DNA amplifier.

5.3 Preliminary rotaxane assembly and nanopore experiments

Rotaxanes between thread 3 and circle 1 could be formed readily with no alteration to the protocol for assembling linear rotaxanes. However, the shape of the *I/V* curve for the rotaxane formed from a circular hybridizing strand was slightly different from the linear primer 0 case (Figure 5.2a). Furthermore, the circular rotaxane complex was found to be less stable than the linear form so a stepped voltage protocol covering a smaller range from 0 to +40 mV was used to characterise the assembly. The differences in shape can be explained by the difference in the geometry of the assemblies (Figure 5.5a). In the case of the linear primer, the current at a given voltage is the time-average of the equilibrium between two states, with the equilibrium being driven to favour positions where the duplex resides in the pore at higher potentials. The ability of the duplex DNA to enter the vestibule of the pore confers stability at higher potentials. However, in the case with a circular duplex-forming strand, the circle is too large to be accommodated in the pore. The lower ion current suggests that the average position of the DNA threaded through the pore is lower than the linear case. At higher potentials the bulky circular duplex region is not afforded extra stabilisation by inclusion within the vestibule and thus can be easily peeled off, it was hence only usually characterised up to 40 mV.

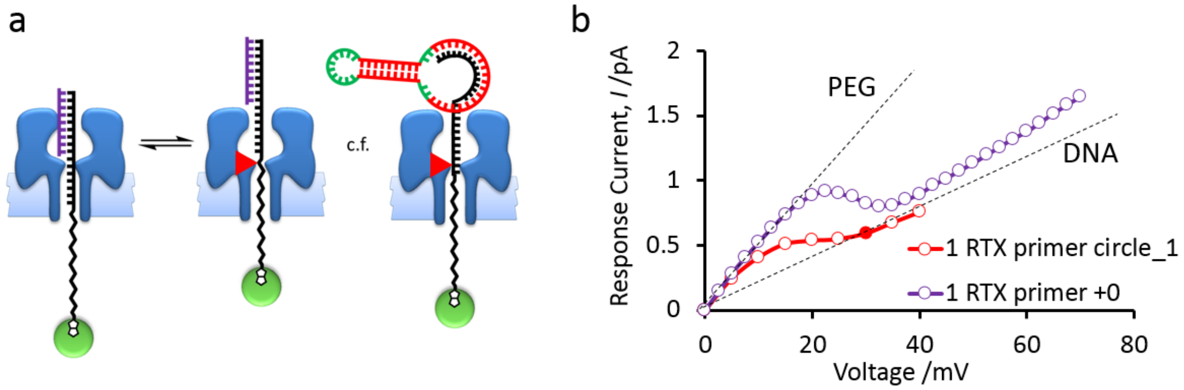

Figure 5.2 **a**, comparison of rotaxanes with linear primer **0** and circular duplex forming strands. **b** the *I/V* curve for the rotaxane formed between thread 3 and circle 1(red) c.f. primer 0 and thread thread 3 (purple)

Due to the size of the circle sequence, many nucleotide incorporations would be required before the system shows induced changes in the current level due to the displacement of the thread strand. To see multiple cycles of the device would require many times more sequential incorporations than have been recorded in single experiments in previous chapters. As it is known from previous experiments that the bilayer can become unstable over extended periods at constant potentials, the conditions of the experiment were altered to increase the rate of nucleotide incorporation. The concentration of each dNTP was increased from 12 pmoles to 300 nmoles. However, it was found that addition of higher quantities of phi 29 caused very large increases in the observed current similar to that seen in Chapter Four upon addition of high concentrations of Nb.BbvCI. As the proprietary buffer in which the enzyme is supplied contains detergents, this could explain the resulting destabilisation of the bilayer. Consequently, phi 29 was dialysed to remove surfactants and concentrated prior to use in later experiments.

5.4 Real-time observation and data analysis of smRCA coupled to translocation of ssDNA through a transmembrane protein pore

A rotaxane was assembled using thread 3 and circle 1 as described in previous sections. Phi 29 polymerase ~ 7nM (dialysed prior to use) and dNTPs (300 nmoles each) were added to the ground well. The current data were recorded at an applied potential of 30 mV in 200 second sweeps, sampled at 5 kHz and filtered at 1 kHz, concatenated into a single file and then filtered post acquisition with a lowpass Bessel filter at 0.5 Hz. The concatenated ion current trace is shown in Figure 5.6.

Figure 5.3 Real-time current trace during transmembrane rolling circle amplification

Existing literature data provides a starting point for attempts to decipher the complicated states observed in the ion current recording shown in Figure 5.3. Bayley et al[12] mapped the nucleobase recognition capabilities of different regions of the stem of wild-type and a mutant strain of α-HL. This was achieved by performing nanopore recordings on multiple variants of streptavidin/biotin-capped poly dC oligonucleotides in which a single variant base was systematically scanned through different positions in the sequence. They identified three recognition domains – R1, R2 and R3 which differed in their capacity to distinguish each base (Figure 5.7a). The measured values in[12] were used to calculate an average value for each base (Figure 5.7b). The calculated average values were then used to calculate the relative expected values in the present system (Figure 5.7d) by referring to the upper observed state which was assumed to correspond to occupation of the pore by dA as this was the base that had the highest average current level based on the results in[12].

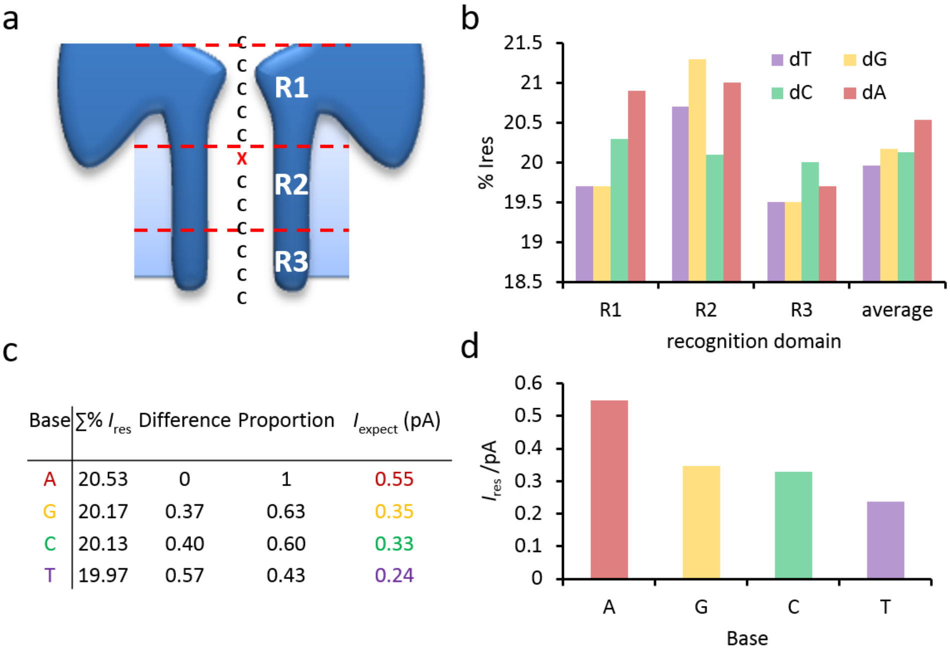

Base	∑% I_{res}	Difference	Proportion	I_{expect} (pA)
A	20.53	0	1	0.55
G	20.17	0.37	0.63	0.35
C	20.13	0.40	0.60	0.33
T	19.97	0.57	0.43	0.24

Figure 5.4 Determination of correspondence between current states and base identity. **a** Bayley's identification of recognition domains and **b** measured current resolution of each domain and the calculated average for each base. **c** schematic of base identity of present system. **d** calculation of current levels in the present work **e** calculated relative residual currents for each base in the present system.

In order to understand the data generated by the transmembrane rolling circle amplifier, the trace of real-time data was overlaid on the relative values for each base calculated from reference[12]. This was then analysed to identify repetitive patterns indicative of complete rotations of the circle (Figure 5.5). The calculated values for d C/G/T are indicated on the trace, but as they are all rather close. Furthermore, it has been previously shown in another pore system (MspA) that the sequence immediately flanking a base affects the overall signal at any point as the resolving power is different for each base in each recognition domain[13]. This is relevant in our system due to the heteropolymeric context of each base as it translocates meaning that the model transcript repeat sequence (Figure 5.a) could not be unambiguously mapped onto the trace in Figure 5.5b. However, the dA calculated value indicated by the red overlay is sufficiently distinct from the other levels to allow a tentative

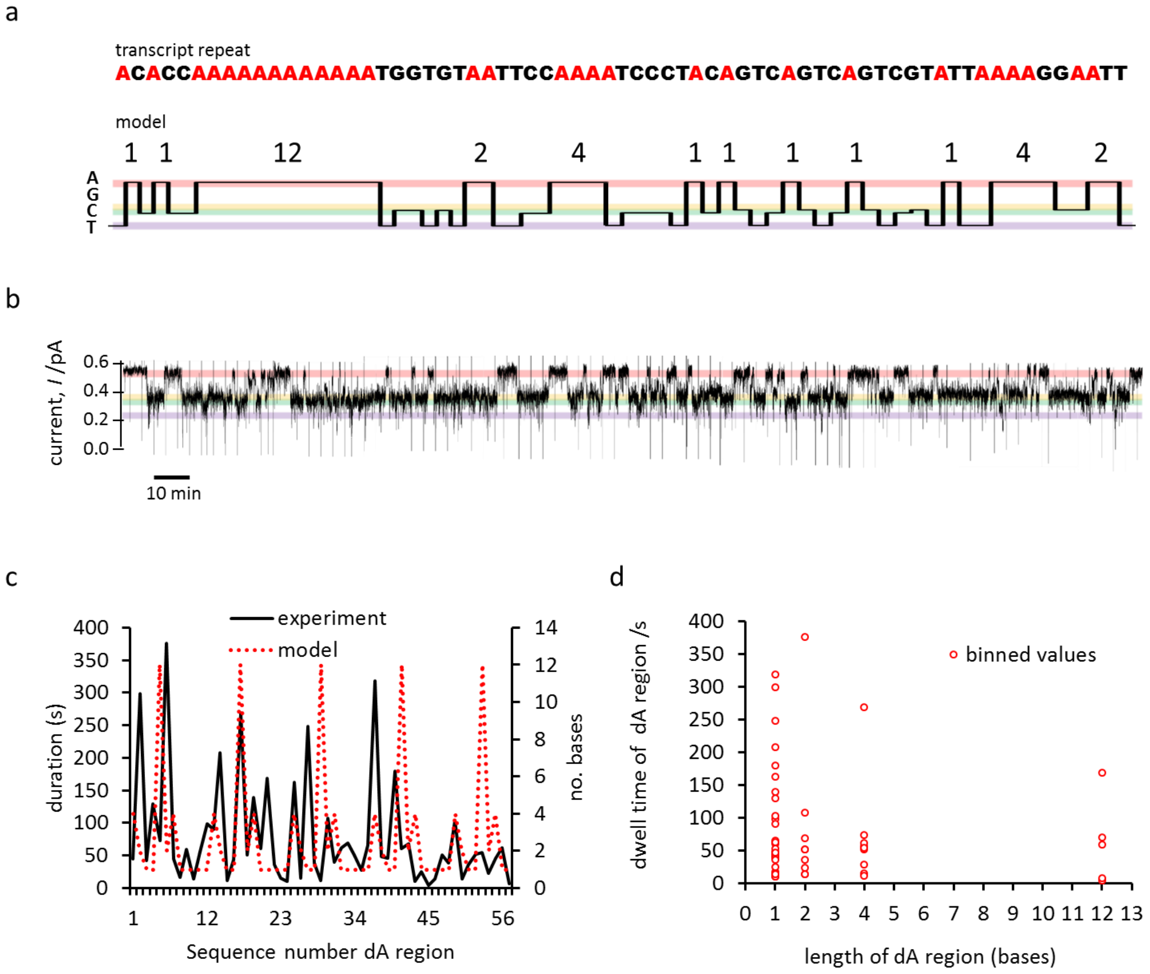

e

	A states			
Length	1	2	4	12
Counts_{EXP}	28	8	9	4
Counts_{CYC}	7	2	2	1
Quotient	4	4	4.5	4

f

Number cycles	bases / cycle	Total time (s)	Cycle duration (s)	Average dwell time base^{-1}	Speed (bases min^{-1})	rate of rotation (Å min^{-1})
4.125	67	18725	4539.4	67.8	0.89	0.30

Figure 5.5 Analysis of real-time current recording as ssDNA was translocated through a nanopore by RCA. **a**, repeat sequence of the DNA transcript from RCA and corresponding model current levels based on reference[12]. **b**, real-time current data during single-molecule nanopore RCA overlaid on model current levels. **c**, plots of durations of manually extracted experimental regions suggested as corresponding to dA (black line) and corresponding repeat model data dA region length. **d**, binning of the experimental values into the model values. **e** calculated number of cycles of operation **f** calculated rate of rotation of the circular strand.

identification of repetitive sequence information. While it is tempting to try to directly assign the sequence, the task is further complicated by the stochastic nature of the enzymatic process which means that a given number of incorporations will not necessarily occur in the same amount of time in each cycle. The duration of each putative A state event was plotted against the order in which they occurred (Figure 5.5c black trace) and compared to the equivalent model data based on the length of the A regions in the repeat transcript (Figure 5.5c red trace). Visual inspection suggests a moderate alignment between the longest measured events and the longest A regions in the model repeat transcript. Plotting of the measured event durations against five repeats of the model transcript (Figure 5.5d) followed by division of the number of events for each resulting set (Figure 5.5e $\text{counts}_{\text{EXP}}$) by the number of counts of each length per cycle (Figure 5.5e $\text{counts}_{\text{CYC}}$) gave suggested values for the number of cycles that had occurred. These were then averaged and used as a basis to calculate the putative rate of rotation of the circular strand as the amplifier operated (Figure 5.5f). Thus an average of ~4 cycles was implied by the correlation analysis and a rate of rotation for the circular strand of ~ 0.21 Å min^{-1}. This corresponds to roughly 1 base per minute, presumably this could be increased by increasing the concentration of dNTPs and enzyme present.

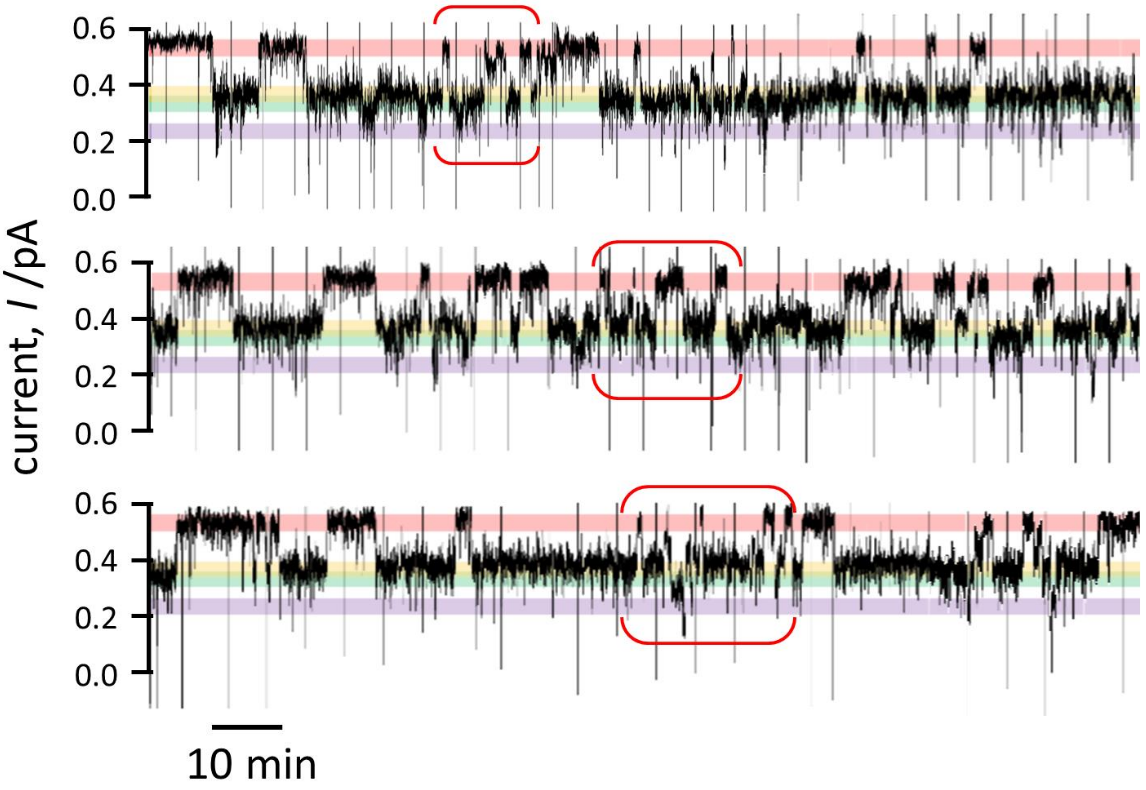

Figure 5.6 Suggested interpretation of repetitive pattern, new cycles are indicated by the red brackets, the assignment is based on the similarity of the regions.

We have suggested that the observed trace corresponds to roughly four cycles of rolling circle amplification, using key repetitive features indicated by the red brackets in Figure 5.6. The region at the start of the trace, we believe corresponds to the translocation of the thread region which is not involved in complexation to the circle and is hence not repeated in the transcript.

5.5 Conclusions & future work

A new synthetic transmembrane machine based on a DNA-PEG/α-HL rotaxane was constructed and the successful autonomous operation monitored for four cycles was characterised at the single-molecule level. The machine-like behaviour was quantified using a simple correlation analysis to determine the number of cycles observed and the rate of rotation of the circular strand component. The system functions as an elementary nanomechanical mimic of biological membrane signal transduction as the information containing product of the mechanism's operation is extruded on the opposite side of the bilayer from the initial circular input strand and the output is amplified with respect to the input. The system shows some promise for certain applications in single-molecule DNA sequencing which will be further developed in future work.

Steps towards the most ambitious goal of reading unambiguous sequence information include performing future experiments at higher applied potential and higher concentrations of KCl, since phi 29 has been shown to remain functional at 300 mM[8]. Higher salt concentrations would hopefully improve the signal-to-noise ratio. Also, a series of experiments could be performed in which the poly dT region of the circular strand was modified to include a region of each of the other bases allowing the current level associated with each base to be better determined. Furthermore the concentration of each dNTP could be systematically varied such that the average durations of each current state were altered in order that the sequence could be better inferred. It is certainly worth noting that the methodology employed to analyse the data was rather crude, a possible collaboration with Nacho Molina would attempt a more detailed analysis employing Bayeesian Hidden Markov Models (BHMM) to obtain more detailed sequence information from the present and future datasets. Markov models have previously been used to identify patterns in many single-molecule studies in which the processes being investigated include a stochastic component, for example the burst kinetics of mammalian gene transcription[14] and the analysis of single-molecule FRET trajectories[15].

5.6 Materials and Methods

M5.1 Synthesis of circular strand circle 1

The sequence of circle 1 (Figure M5.1a) (purchased from sigma with 5' phosphorylation) was designed to include a region complementary to thread 3, a 12 base region of dT and a self-complementary motif. The poly dT regions mean that the DNA transcript will contain poly dA regions, which provide an opportunity for monitoring thread translocation in nanopore experiments (since polyA has been shown to exhibit the largest residual current of the standard DNA bases when threaded through α-HL[12]). The self-complementary region in the sequence design allowed the ligation of the circle to proceed with very high yields by exploiting the high effective molarity of the 5’ and 3’ ends which are brought together in the adjacent hair-pin structures (Figure M5.1a). This approach avoids the limitations of other methods to construct circular strands. For example, the use of DNA splints in ligation reactions often leads to lower yields, or can give concatenated, linear assemblies. The success of the ligation reaction was confirmed by denaturing PAGE (Figure 5.2c). The circularised strand has a different mobility through the gel matrix due to its reduced conformational flexibility compared to the non-circularised form. Comparison of lanes 3, 6 and ii show the development of a new band corresponding to the circularised strand when ligase is present and the elimination of the lower band when exo I and exo III (which catalyse the hydrolysis of ssDNA) were present. The thread strand used was thread 3, the synthesis and characterisation of which are described in Chapter Four of the present work section M4.3

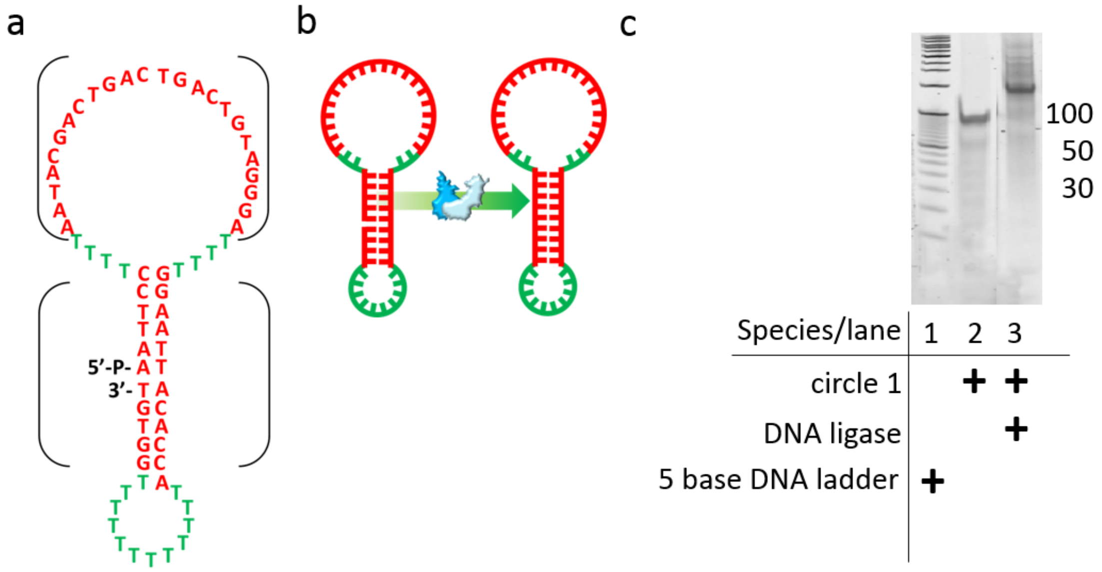

Species/lane	1	2	3
circle 1		+	+
DNA ligase			+
5 base DNA ladder	+		

Figure M5.1 Sequence, ligation and characterisation of circular strand. **a** The sequence contained two coding domains (red), one was complementary to the thread strand (loop) while the other was self-complementary (duplex),. The strand was bought with 5’ phosphorylation allowing the strand to be ligated into a true circle using DNA ligase. **b**, scheme of ligation **d**, PAGE analysis of the assembly reaction.

M5.2 Computer simulation of rotaxane assembly

According to the Dinamelt webserver, the melting temperature of the duplex formed between the thread 3 and circle 1 strands was higher than that formed by circle 1 with itself (Figure M5.2b). However, the Dinamelt algorithms do not allow a very sophisticated simulation and can only model isolated duplex regions, and does not take strain that might be induced by the loop regions into account. The process of hybridisation in this case involves the formation of a length of double-stranded DNA within a circularised single strand. Given the difference in the persistence length of dsDNA compared to ssDNA it was reasoned that strain would provide a significant factor in determining complexation. Thus, to gain an insight into whether the hybridisation could proceed to form the desired rotaxane, a course-grained simulation was run using the Linux software, oxDNA[11]. oxDNA is tolerant of both circular and linear ssDNA and can perform simulations in which both are present, as here.

The oxDNA simulation was performed in two parts. First, the circle 1 was run alone with one of its internal base pairs established. A second simulation was then performed with the thread 3 sequence (blue) added to the minimised circle 1 structure (red). The simulation was started with a pre-formed base pairing interaction between one of the nucleotides in each sequence. This initial pairing assists the subsequent minimisation of the simulation (which seeks to maximise the number of base pairs, while taking basic strain and steric factors into account). After a large number of minimisation cycles, the snapshot shown in Figure 5.3 was obtained showing that the strain of the loops does not completely prevent binding of the thread strand. Indeed, the simulation showed that thread-circle hybridisation outcompetes intramolecular circle-circle self-hybridisation to reduce strain in the system.

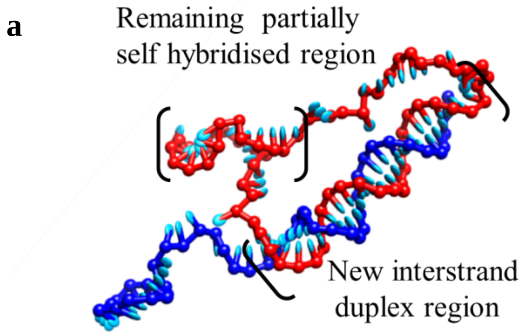

b

	T_m (° C)	
Species	Thread_Nb	Circle_1
Thread_Nb	-23.8	77.0
Circle_1	77.0	44.4

Figure M5.2 a oxDNA model of rotaxane assembly using circle 1 and thread 3. **b** The melting temperatures obtained from Dinamelt suggests that the hybridisation between thread 3 and circle 1 occurs in the desired fashion. **oxDNA** simulations were performed by Justinas Slikas

M5.3 Competency of components for RCA

To confirm that the thread 3 and circle 1 sequences would be competent substrates for RCA, a test reaction was carried out in the buffer usually used for nanopore experiments. The components for RCA were mixed together and reacted overnight at room temperature. The red ringed band at the top of lane 8 in Figure 5.4 shows that the extension products of RCA (which are too large to enter the gel) were successfully obtained. Short primers that hybridise to the single-stranded product of RCA were then added at the end of the RCA reaction, and the mixture was subjected to a restriction digest with two enzymes Mse 1 and Mlu 1. These enzymes were selected by scanning a duplex composed of circle 1 and its complement for restriction sites using NEB cutter V 2.0. These primers allow the putative RCA product to be cleaved by the restriction enzymes, generating new fragments of distinct length from those previously present, which could be seen on a denaturing PAGE (Figure 5.4, lane 9).

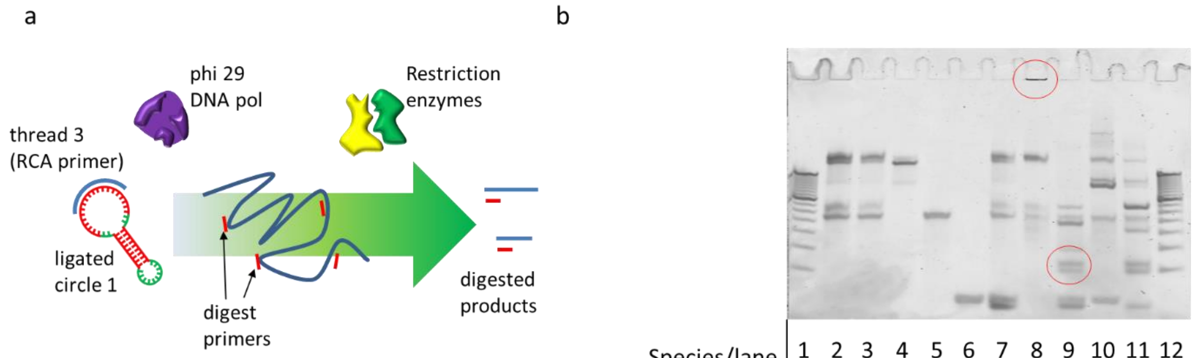

Species/lane	1	2	3	4	5	6	7	8	9	10	11	12
circle 1		+	+	+			+	+	+	+	+	
thread 3		+	+		+		+	+	+	+	+	
phi 29 DNA pol			+					+	+	+	+	
dNTPs								+	+	+	+	
primer Mse						+	+		+	+		
primer Mlu						+	+		+		+	
Mse							+		+	+		
Mlu							+		+		+	
5 base DNA ladder	+											+

Figure M5.3 Denaturing PAGE confirmation of RCA competency of components. Samples were run on a 7M urea 12% PAGE at 300 V for 55 minutes in 1 xTBE buffer.

Electrical Measurements

Single-channel ion current recordings of transmembrane rotaxanes. A single channel was obtained in a suspended bilayer according to the general procedure outlined in Chapter Two of the present work. The buffer used in the final rolling circle amplifier experiment contained KCl [150 mM], Tris-HCl [25 mM] and Mg(OAc)2 [12 mM]. A rotaxane was prepared in the following general manner. The streptavidin-capped 5'-biotinylated DNA-PEG copolymer thread strand was added to the live well to a final concentration of ~100 nM. DNA circle 1 was added to a final concentration of ~2.5 μM to the ground well of the experimental cell. The thread strand was captured by applying a transmembrane potential of –140 mV until a reduction in the transmembrane current (from ca. –18 to –5pA at –140 mV) was observed that corresponded to a capture. The potential was then reduced to –28 mV to allow the primer to hybridize to the 5'-end of the thread protruding through the pore into the ground well for ~eight minutes, thereby forming the desired rotaxane. The rotaxane was characterized by applying potential sweeps in 5 mV steps, each of 2 second duration across a 40 mV range, from 0 to +40 mV, giving characteristic *I/V* profiles e.g. Figure 5.2b. After confirmation of a rotaxane assembled using circle 1, the following were added to the ground well: DNA polymerase phi 29 [~7 nM], deoxynucleotide triphosphates (dNTPs, N = A, C, G, T) (Bioline) [~12 μM] each. A constant transmembrane potential of +25 mV was applied and the ion current was recorded. The data were then filtered to 1 Hz after acquisition using an eight-pole Bessel filter.

Enzymes phi 29 polymerase was purchased from both NEB and Fermentas, the successful nanopore experiment involved enzyme that had been dialysed with an 8000 MWCO dialysis cartridge (Thermoscientific) prior to use. Quickstick (T4) DNA ligase was purchased from Bioline.

DNA thread 3 was prepared in house as previously described, see Chapter Four for full characterisation data. Circle 1 was purchased from Sigma-Aldrich with 5' phosphorylation and desalt purification before being circularised using DNA ligase as described in Figure M5.1.

5.7 References

1. Inciarte, M. R.; Salas, M.; Sogo, J. M., Structure of replicating DNA molecules of Bacillus subtilis bacteriophage phi 29. *J. Virol.* **1980,** *34* (1), 187-199.
2. Méndez, J.; Blanco, L.; Esteban, J. A.; Bernad, A.; Salas, M., Initiation of phi 29 DNA replication occurs at the second 3' nucleotide of the linear template: a sliding-back mechanism for protein-primed DNA replication. *Proc. Natl. Acad. Sci. USA* **1992,** *89* (20), 9579-9583.
3. Johne, R.; Müller, H.; Rector, A.; van Ranst, M.; Stevens, H., Rolling-circle amplification of viral DNA genomes using phi29 polymerase. *Trends Microbiol.* **2009,** *17* (5), 205-211.
4. Cheng, W.; Yan, F.; Ding, L.; Ju, H.; Yin, Y., Cascade signal amplification strategy for subattomolar protein detection by rolling circle amplification and quantum dots tagging. *Anal. Chem.* **2010,** *82* (8), 3337-3342.
5. Deng, Z.; Tian, Y.; Lee, S.-H.; Ribbe, A. E.; Mao, C., DNA-encoded self-assembly of gold nanoparticles into one-dimensional arrays. *Angew. Chem., Int. Ed.* **2005,** *44* (23), 3582-3585.
6. Cheglakov, Z.; Weizmann, Y.; Braunschweig, A. B.; Wilner, O. I.; Willner, I., Increasing the complexity of periodic protein nanostructures by the rolling-circle-amplified synthesis of aptamers. *Angew. Chem., Int. Ed.* **2008,** *120* (1), 132-136.
7. Sahu, S.; LaBean, T. H.; Reif, J. H., A DNA nanotransport device powered by polymerase ϕ29. *Nano Lett.* **2008,** *8* (11), 3870-3878.
8. Lieberman, K. R.; Cherf, G. M.; Doody, M. J.; Olasagasti, F.; Kolodji, Y.; Akeson, M., Processive replication of single DNA molecules in a nanopore catalyzed by phi29 DNA polymerase. *J. Am. Chem. Soc.* **2010,** *132* (50), 17961-17972.
9. Gomis-Ruth, F. X.; Moncalian, G.; Perez-Luque, R.; Gonzalez, A.; Cabezon, E.; de la Cruz, F.; Coll, M., The bacterial conjugation protein TrwB resembles ring helicases and F1-ATPase. *Nature* **2001,** *409* (6820), 637-641.
10. Chen, I.; Christie, P. J.; Dubnau, D., The ins and outs of DNA transfer in bacteria. *Science* **2005,** *310* (5753), 1456-1460.
11. Romano, F.; Hudson, A.; Doye, J. P. K.; Ouldridge, T. E.; Louis, A. A., The effect of topology on the structure and free energy landscape of DNA kissing complexes. *J. Chem. Phys.* **2012,** *136* (21), -.
12. Stoddart, D.; Heron, A. J.; Mikhailova, E.; Maglia, G.; Bayley, H., Single-nucleotide discrimination in immobilized DNA oligonucleotides with a biological nanopore. *Proc. Natl. Acad. Sci. USA.* **2009,** *106* (19), 7702-7707.
13. Manrao, E. A.; Derrington, I. M.; Pavlenok, M.; Niederweis, M.; Gundlach, J. H., Nucleotide discrimination with DNA immobilized in the MspA nanopore. *PLoS ONE* **2011,** *6* (10), e25723.
14. Suter, D. M.; Molina, N.; Gatfield, D.; Schneider, K.; Schibler, U.; Naef, F., Mammalian genes are transcribed with widely different bursting kinetics. *Science* **2011,** *332* (6028), 472-474.
15. McKinney, S. A.; Joo, C.; Ha, T., Analysis of single-molecule FRET trajectories using hidden Markov modelling. *Biophys. J.* **2006,** *91* (5), 1941-1951.

Chapter Six

α-HL as a potential transmembrane DNA ligase

Abstract

In this chapter the design and experimental data from early attempts to mimic enzymatic DNA ligation using a transmembrane rotaxane approach are presented. In this case, the vestibule of α-HL is assumed to provide a privileged solvent environment, much like that found in most enzymes, in which substrate molecules are isolated from the aqueous phase and hence more predisposed to react with each other. The dynamic equilibrium of the thread as it moves against and within the vestibule region of the pore under an applied potential is proposed to approximate the fluctuation which in an enzyme help to minimise the energy gap between the ground state and the transition state of the enzyme substrate complex.

6.1 Introduction

Enzymatic DNA ligation is a key process in natural DNA replication. Archetypal DNA ligases bind to a nicked region of duplex DNA and form a complex with adenosine triphosphate (ATP) and an Mg^{2+} ion to catalyse the rearrangement of the covalent bonds in the system. First, a phosphodiester bond in the bound ATP is broken to give PP_i which is released from the complex while AMP is transferred to the 5’ phosphate group of the nicked DNA. The AMP activates the phosphorus atom of the original phosphate group to attack by the hydroxyl group at the adjacent 3’ end of the nicked DNA forming a new phosphodiester bond between the adjacent 5’- phosphate and 3’- hydroxyl ends of the nicked DNA (with the AMP acting as a good leaving group) (Figure 6.1).

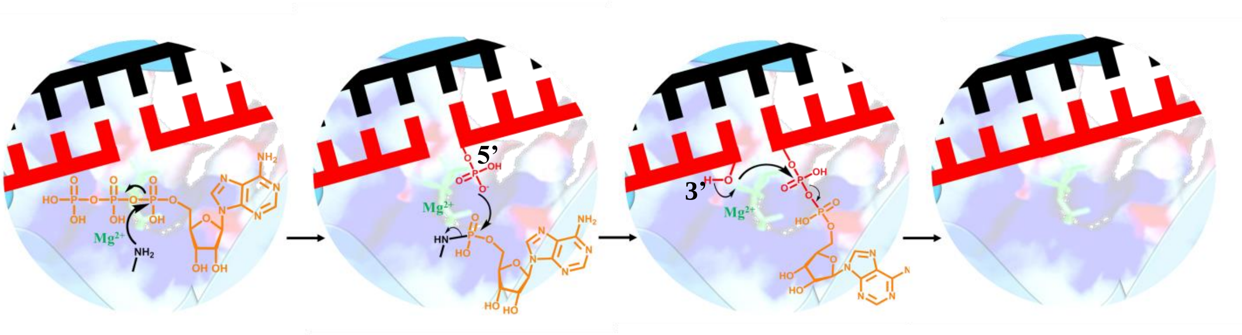

Figure 6.1 Ligation of a nicked duplex of DNA in the active site of an archetypal DNA ligase enzyme.

The favourability of the reaction is increased because of the enzymes dictation of the precise orientations of the components which in turn depends on the geometry of the active site[1]. The active site includes a DNA binding domain and an ATP binding pocket, the hydrophobic interior of the DNA binding domain accommodates the bases of the DNA and excludes water while key residues within the ATP binding pocket ensure the correct relative orientations of the substrates for the reaction to occur.

DNA ligases are often used in molecular biology for inserting genetic sequences of interest (vectors) into plasmid DNA[2] and as components in signal amplification schemes of various assays[3]. In addition, enzyme-free methods of DNA ligation have been developed[4] that make use of so-called DNAzymes. DNAzymes bind to specific DNA sequences while coordinating ATP and Mg^{2+} to facilitate the transfer of AMP to the 5’- phosphate of substrate DNA. DNAzymes have been used in signal amplification cascades in solution[4], on DNA-functionalised surfaces[5], and as stimuli-responsive ‘smart gates’ on drug containing silica nanoparticles.

6.2 Design and assembly of a putative synthetic transmembrane DNA ligase

A preliminary investigation was performed to see if the vestibule region of α-HL could be used as a suitable environment to catalyse ligation in the presence of ATP and $Mg(OAc)_2$. DNA ligase binds to nicked duplex DNA, coordinating ATP with specific lysine residues and in the presence of Mg^{2+} it catalyses the transfer of a phosphate group from ATP to the 5'phosphate end of the nicked DNA improving conditions for reaction with the 3' end of the nick. Similarly, the vestibule of α-HL contains many protruding lysine residues that might provide a similar enough coordination environment to accomplish the transfer of the phosphate group thereby favouring the DNA ligation reaction. In addition, it was hoped that the DNA being held within the pore vestibule might approximate DNA-ligase binding such that the substrate ends have some increased probability of approaching each other with the correct orientation and energy to react. Although the presently proposed system would not possess cyclical machine-like behaviour since the ligated product would be a dead-end, it would still constitute the first example of an rate acceleration by a designed transmembrane system.

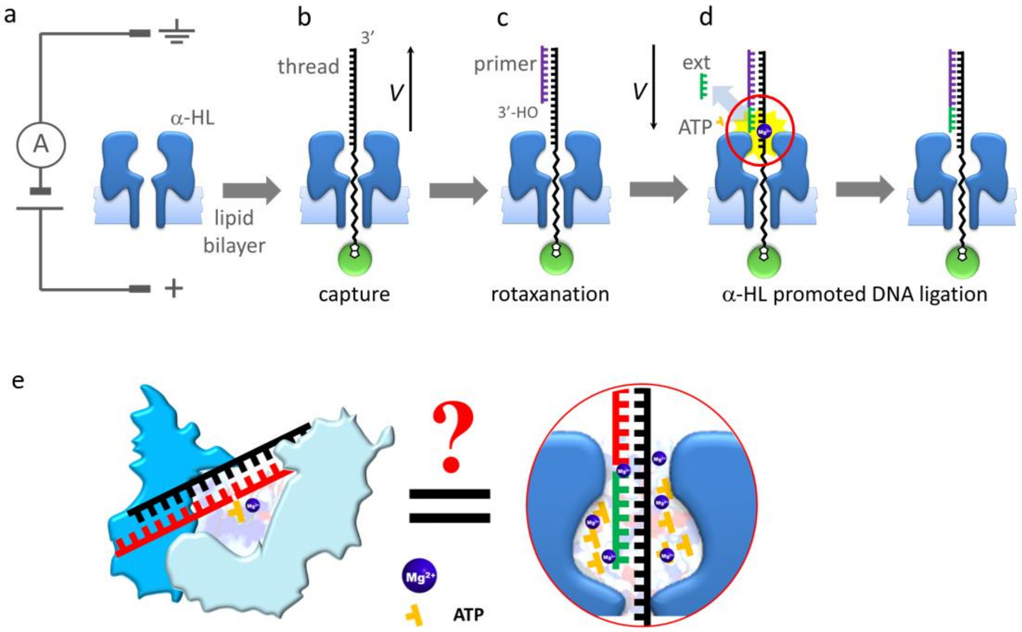

Figure 6.2 Proposed enzyme mimicry by α-HL. **a** Addition of a seven-base oligonucleotide 5'monophosphate (5'-ONMP) to a conventional thread_Nb/primer+0_Nb rotaxane results in transient formation of a nicked duplex that will spend a variable proportion of time within the vestibule region of the pore under applied potentials. **b** Cartoon comparing ligase-DNA binding and capture of a nicked duplex within α-HL.

6.3 Analysis of binding for a seven base oligonucleotide 5'-monophosphate

The model system shown in Figure 6.1 was characterised using a stepped voltage protocol as described in previous chapters and the changes to the I/V behaviour upon addition of the 7-base oligonucleotide 5'-monophosphate (ONMP) were monitored (Figure 6.2).

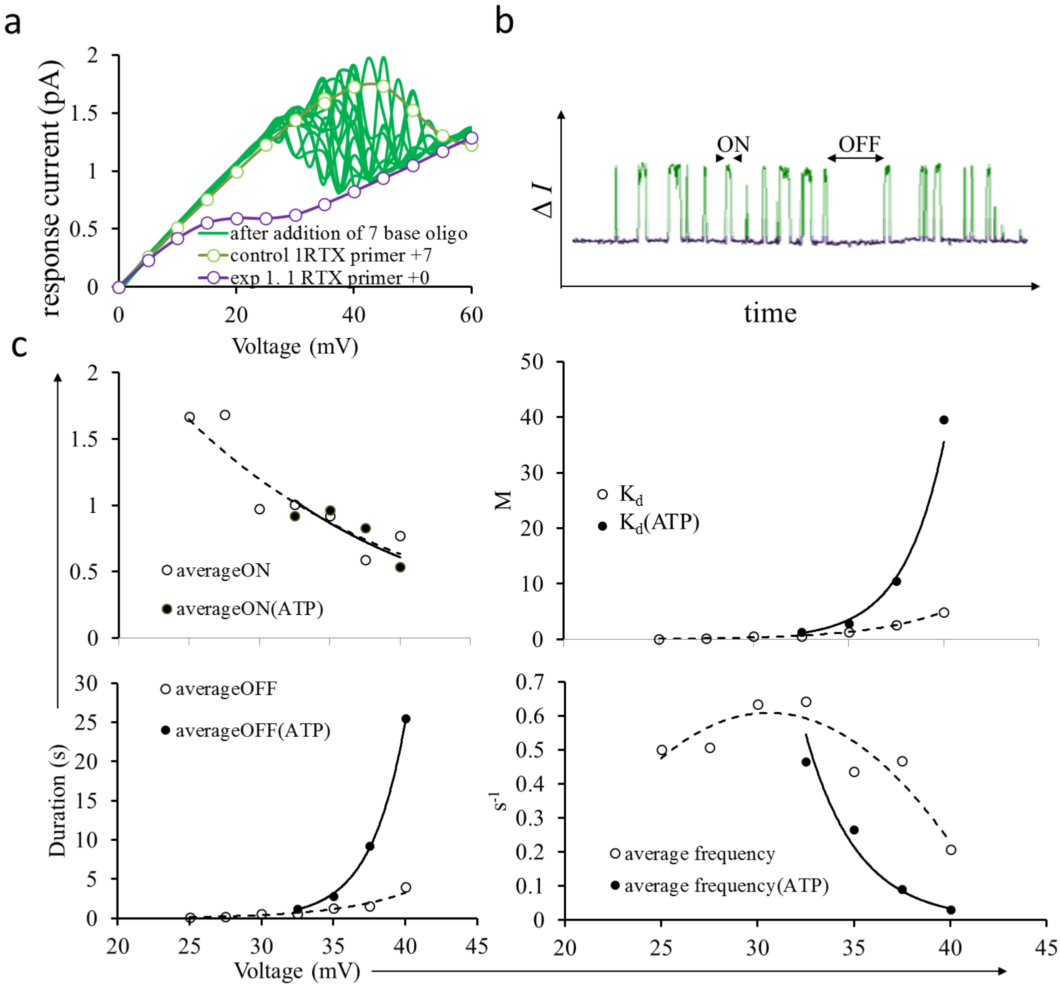

Figure 6.2 Addition of seven-base 5'-ONMP to thread_Nb/primer+0_Nb rotaxane and the effect of the addition of ATP. **a** The effect of adding ONMP to the *cis*-well after rotaxane formation, the I/V curve for a rotaxane with primer+7_Nb corresponding to the end condition of the system after the intended ligation is shown as a control (light green). **b** The corresponding real-time current data generated at a fixed applied potential. **c** Comparison of event characteristics at different applied potentials with and without ATP (5 mM).

The binding of 5'-ONMP to the primer+0 rotaxane resulted in an increase in the observed current response. If ligation were to occur then this current change would be expected to irreversible.

The durations of the states where the 5’-ONMP is bound (on) and unbound (off) were monitored at a range of applied potentials to establish the force dependence of the stability of the nicked duplex. This was defined in terms of the average event duration, dissociation constant K_d and the frequency of on events by analysing the event durations. The experiment was then repeated after the addition of ATP to establish the effect of ATP on the K_d of the nicked duplex and hence to determine the optimum applied potential to apply during continuous recording. The ligation reaction is proposed to require the nick to be within the vestibule of the pore, this happens only above certain potentials as demonstrated by the curve of the control primer+7_Nb. However, the likelihood of dissociation also increases with applied potential. Reasoning that sometimes the ONMP remains associated with the thread and brings the nick into the pore, we can assume that the optimum potential to apply to observe ligation is when the frequency of association events is greatest.

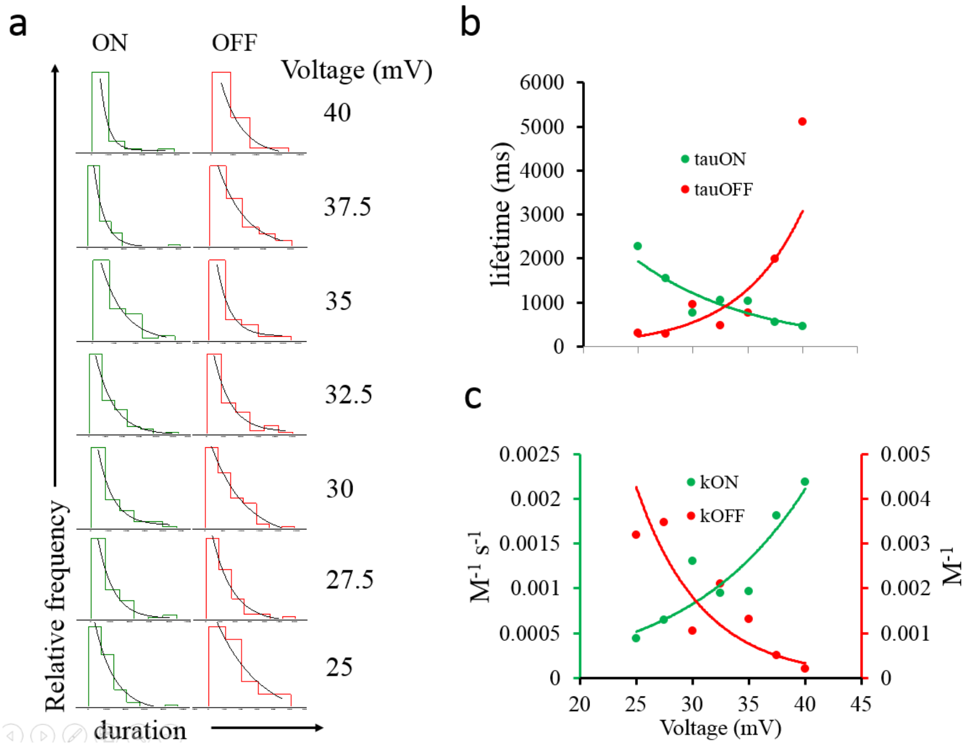

Figure 6.3 Determination of rate constants k_{ON} and k_{OFF} for the formation of the nicked duplex at different potentials. **a** histograms of on and off event durations **b** lifetimes of on and off states **c** rate constants of on and off states.

Analysis of the event durations shows that these events are most frequent at around 32.5 mV (Figure 6.3). The single molecule nature of the experiment allows extraction of the lifetimes of the nicked duplex and the unbound state. The event durations are binned, bin width (h) is determined according to the Scott formula[6]

$$h = 3.5\sigma/\sqrt[3]{n}$$

The histogram peaks are fitted to a single exponential decay, this relates the duration of events to the most probable lifetime of the nicked duplex and the initial rotaxane via the simple equation:

$$y = A_0 \exp^{(-t/\tau)} + C$$

The rate constants for the on and off events k_{ON} and k_{OFF} are then given by taking the reciprocals of the lifetimes τ_{ON} and τ_{OFF}.

The results shown in Figure 6.3 indicate that the presence of ATP has little effect on the duration of on events, but the duration of off events is affected by ATP, particularly at higher potentials. This may be due to competitive interactions between ATP and the T bases in the ONMP which will raise the barrier to hybridisation with the thread strand. The unimolecular dissociation event appears to be less affected by the presence of ATP than association. The presence of ATP was not shown to have much effect on the off duration below about 32.5 mV. Hence, a potential of 32.5 mV was used thereafter with the aim of observing the transition from a two-state behaviour corresponding to on/off binding to a single state corresponding to an irreversible ligation reaction.

Unfortunately, no such irreversible current change was seen in the course of this project. It is likely that the energetics of the intended reaction provide a fundamental barrier to the reaction. A more successful approach might be to employ substrates that are preactivated by the addition of a triphosphate leaving group in place of the much less activated 5’-mono-phosphate, as has been used in previous non-enzymatic ligation reactions[4]. Nonetheless, the system provided useful data to conduct preliminary investigations into the dynamic behaviour of the system that might aid future work using more reactive substrates.

6.4 Conclusions & future work

The possibility of using α-HL as a transmembrane mimic of a DNA ligase using a DNA/PEG α-HL rotaxane approach was suggested and an initial investigation undertaken. The optimum voltage in which a substrate strand was held within the pore was determined, and the effect of ATP on the binding characteristics of a 5'-ONMP was investigated. The results suggest that the presence of Mg^{2+} does not affect the binding of the 5'-ONMP to the thread although it does appear to counteract the effects of ATP on binding. The key experiment was performed only once and the attempt to observe ligation failed. Nonetheless, a starting point for future work has been established

While further attempts using the current oligonucleotides and approximate methodology may result in successful demonstration of α-HL-catalysed DNA ligation, alternative strategies to investigate could include simple alterations of the current approach. Different lengths of ONMP could be screened in nanopore experiments such that the range of positions of the nicked region with respect to the interior surface is varied. An alternative approach could be to use an oligonucleotide bearing a much better leaving group such as a 5'-triphosphate, negating the need for a preliminary adenyl/phosphoryl transfer step to activate the substrate oligonucleotide.

6.5 Materials and methods

Electrical Measurements

Single-channel ion current recordings of transmembrane rotaxanes. A single channel was obtained in a suspended bilayer according to the general procedure outlined in Chapter Two of the present work. The buffer used in the final rolling circle amplifier experiment contained KCl [150 mM], Tris-HCl [25 mM] and Mg(OAc)2 [12 mM]. A rotaxane was prepared in the following general manner. The streptavidin-capped 5'-biotinylated DNA-PEG copolymer thread strand was added to the live well to a final concentration of ~100 nM. DNA primer 0 was added to a final concentration of ~2.5 μM to the ground well of the experimental cell. The thread strand was captured by applying a transmembrane potential of –140 mV until a reduction in the transmembrane current (from ca. –18 to –5pA at –140 mV) was observed that corresponded to a capture. The potential was then reduced to –28 mV to allow the primer to hybridize to the 5'-end of the thread protruding through the pore into the ground well for

~eight minutes, thereby forming the desired rotaxane. The rotaxane was characterized by applying potential sweeps in 5 mV steps, each of 2 second duration across a 70 mV range, from 0 to +70 mV, giving characteristic *I/V* profiles e.g. Figure 5.2b. After confirmation of a rotaxane assembled using primer 1, the following were added to the ground well: adenosine triphosphate (Bioline) [~12 μM] and a seven base region complementary to the thread strand region abutting the 3' end of the primer. A constant transmembrane potential of +25 mV was applied and the ion current was recorded. The data were then filtered to 1 Hz after acquisition using an eight-pole Bessel filter.

DNA thread 3 and primer 0 were prepared in-house as previously described, see Chapter Four for full characterisation data. 5'-ONMP was purchased from sigma with 5' phosphorylation and desalt purification.

6.6 References

1. Subramanya, H. S.; Doherty, A. J.; Ashford, S. R.; Wigley, D. B., Crystal structure of an ATP-dependent DNA ligase from bacteriophage T7. *Cell* **1996,** *85* (4), 607-615.
2. Dugaiczyk, A.; Boyer, H. W.; Goodman, H. M., Ligation of EcoRI endonuclease-generated DNA fragments into linear and circular structures. *J. Mol. Biol.* **1975,** *96* (1), 171-184.
3. Deng, J.-Y.; Zhang, X.-E.; Mang, Y.; Zhang, Z.-P.; Zhou, Y.-F.; Liu, Q.; Lu, H.-B.; Fu, Z.-J., Oligonucleotide ligation assay-based DNA chip for multiplex detection of single nucleotide polymorphism. *Biosens. Bioelec.* **2004,** *19* (10), 1277-1283.
4. Wang, F.; Elbaz, J.; Willner, I., Enzyme-free amplified detection of DNA by an autonomous ligation DNAzyme machinery. *J. am. chem. Soc.* **2012,** *134* (12), 5504-5507.
5. Wang, F.; Orbach, R.; Willner, I., Detection of metal ions (Cu^2+, Hg^2+) and cocaine by using ligation DNAzyme machinery. *Chem. Eur. J.* **2012,** *18* (50), 16030-16036.
6. SCOTT, D. W., On optimal and data-based histograms. *Biometrika* **1979,** *66* (3), 605-610.

Appendix 1

Materials and general experimental methods

A1.1 DNA synthesis

DNA synthesis was carried out on a MerMade 4 solid-phase DNA synthesiser (Bioautomation) using phosphoramidites and coupling reagents (Link Technologies) for standard 3’ to 5’ DNA synthesis according to the manufacturer’s instructions. Highly modified oligonucleotides were synthesised in by the same approach but with extended coupling times and extra coupling steps for modifier reagents. Attempted strategies to improve yields of these difficult oligos are detailed in Chapter Four.

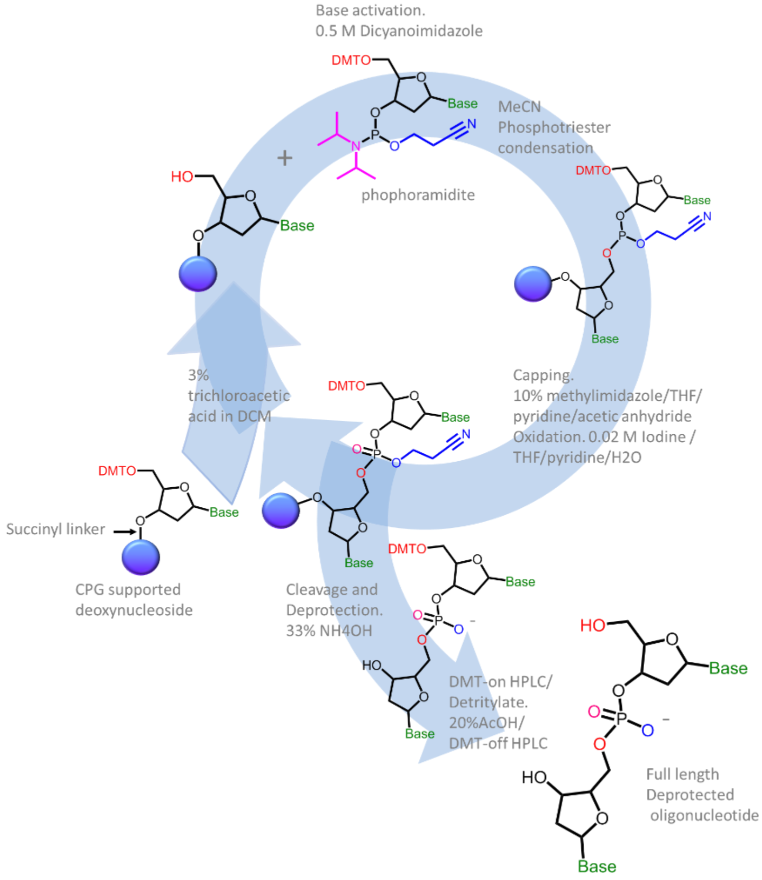

Figure A1.1 Cycle of solid-phase DNA synthesis used in the present work, CPG-supported dimethoxytrityl-protected deoxynucleosides were subjected to a cycle of deprotection, reaction with activated phosphoramidite nucleotide monophosphate analogues and capping and oxidation. Post-synthesis, the oligonucleotide was cleaved from the support and purified usually by two-step reverse-phase HPLC

A1.2 RP-HPLC

Oligonucleotides were purified by two-stage reverse-phase high-performance liquid chromatography (RP-HPLC) using a C-18 semi-preparative column (Supelco Sigma Aldrich) with an acetonitrile / 100 mM triethylammonium acetate in 5:95 acetonitrile: water pH 8 gradient buffer system at a flow rate of 7 ml/min. A column temperature of 65 °C was used to minimise secondary structure (which could complicate retention behaviour) and elution of DNA fractions was monitored by an integrated UV/vis spectrometer at 260 nm on a Dionex ultimate 3000 series HPLC running Chromeleon software. Oligonucleotides were usually synthesised with the final detritylation step omitted prior to cleavage from the controlled porosity glass (CPG) support. The dimethoxytrityl (DMT) protecting group is very hydrophobic compared to the 5’ hydroxyl group of deprotected oligonucleotides. Oligonucleotides bearing the DMT group therefore have a higher affinity for the hydrophobic C-18 column than those without, and hence possess a longer retention time. This permitted the facile separation of the full-length oligonucleotide from deletion/truncation products that did not include the final nucleotide.

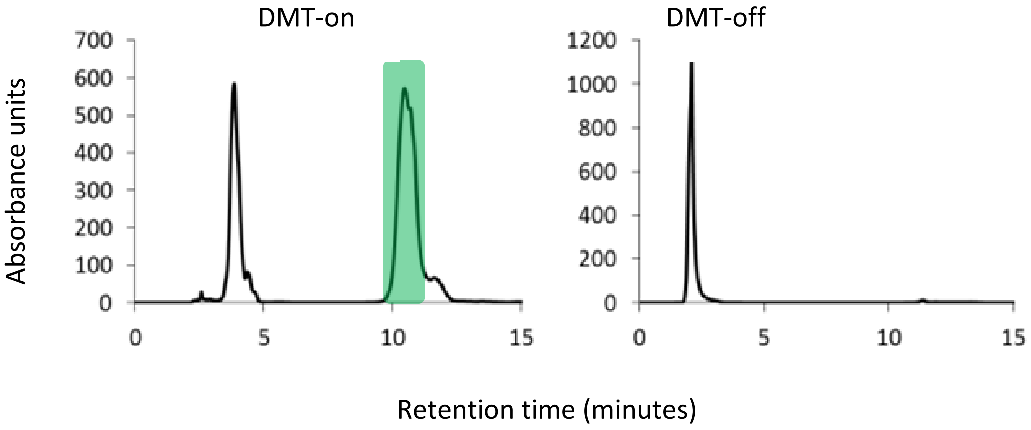

Figure A1.2 Representative HPLC traces for DMT-on and DMT-off oligonucleotides prepared in-house.

Fractions were collected manually as this was found to allow the cleanest separation and avoid collecting shoulder peaks (which were attributed to partially non-deprotected sequences). After collection, the oligo was speedvacced to concentrate it before being detritylated in 40 % AcOH for 1 hour then speedvacced once more before running a second HPLC using a shallower gradient than before. The aim of the shallower gradient was to separate any remaining truncation or deletion products.

A1.3 PAGE and electroelution

Analytical PAGE was usually performed on tris-borate urea gels prepared in-house with the percentage of acrylamide varying according to the length of oligonucleotide being separated. Gels were visualised by staining with SYBR gold (Invitrogen) for ~10 minutes followed by transillumination with UV (254 nm). Lately, the lab has benefited from access to a high- resolution gel fluorescence imager (Typhoon) leading to greatly improved quality of gel pictures obtainable. At times, PAGE was used to purify oligonucleotides for further use and the desired band recovered by careful excision under brief UV illumination. The DNA was then recovered by electroelution at 200 V for 10 minutes with a gel electrophoresis power pack using a homemade electroelution column made from a 1 mL plastic screw cap vial with an integral rubber seal in the cap.

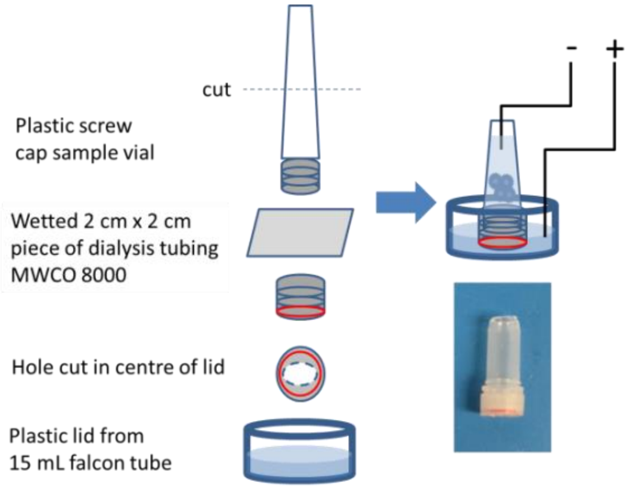

Figure A1.3 Home-made miniature electroelution column. The excised band of interest is crushed using the side of a clean scalpel and placed in the top of the column to which is then added a small volume of standard gel electrophoresis buffer, then the column is clamped in place over the lid from a 15 mL Falcon tube containing more buffer, sufficient to submerge the membrane but not above the level of the lid of the column. Platinum wires were used as electrodes to complete the circuit. DNA fragments of molecular weight above the cut off were recovered while smaller oligos were removed.

A1.4 Electronic current recording

Transmembrane potentials were applied and currents recorded using an Axon Axopatch 200B Patchclamp Amplifier and digitised using an Axon Instruments Digidata 1332A. The sampling rate, filter and gain settings are specified for each set of experiments in the appropriate chapter.

Figure A1.4 Patchclamp apparatus and digidata used in the nanopore experiments. The digidatas are very sensitive to electrical discharge and hence are turned off as rarely as possible and always only once the connected PC and patchclamp have been turned off first.

The apparatus allows the application of potentials from 1 to –1 V D.C. and accurate measurement of currents down to the tens of femtooamperes (such as in our experiments due to the passage of ions through individual protein pores). The sensitivity of the apparatus can cause problems with signal noise due to mechanical vibrations and ambient electric fields intersecting those of the microelectrodes. Thus, to shield the microelectrodes and patchclamp headstage from electrical noise and mechanical vibration our experimental setup is customised with an electroacoustic shielding enclosure (green dashed box, Figure A1.5). In addition, an electronic anti-vibration platform with feedback control (A.V.P., blue dashed box, Figure A1.5) was also used to reduce the effects of low frequency mechanical vibration on the signal. The A.V.P. also reduced low frequency electrical noise stemming from ground loops which can otherwise account for large deviations from the true signal depending on the ionic strength of the buffer used and the sampling rate employed. Low frequency noise contributes less significantly to the signal at high ionic strength and at high sampling rates. However, at high sampling rates the A.V.P. does introduce high frequency electrical noise which becomes a major component of the signal observed. This constrains the utility of the A.V.P. to situations where both sampling rate and buffer ionic strength are low.

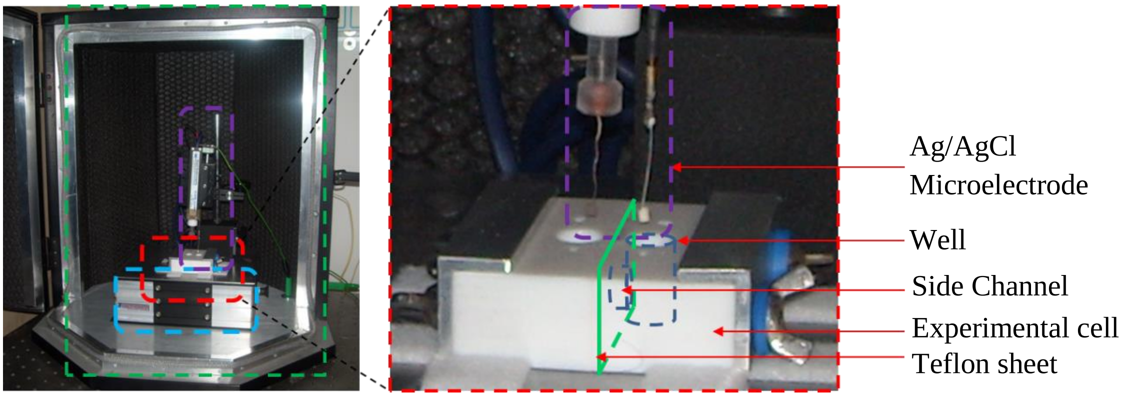

Figure A1.5 Experimental setup for single channel ion current recordings. The patchclamp headstage including the Ag/AgCl microelectrodes (purple dashed box), experimental cell (red dashed box) and anti-vibration platform (blue dashed box) are housed within a custom-built electroacoustic enclosure (green dashed box). An expansion of the experimental cell (red dashed box) which is composed of two teflon blocks bolted together each with a machine-drilled well ~1 mL in volume. Each well contained a side opening such that when the blocks are clamped together the wells are connected through their side openings. A 25 µm thick Teflon sheet is clamped between the two blocks, separating the side openings and glued in place with silicone (3140 RTV coating, Dow Coring). The Teflon sheet contains an aperture of ~ 100 µm diameter and is positioned such that the aperture is in the centre of the lower half of the inter-well channel.

A1.5 Reproducible formation of 100 µm apertures

Apertures are formed in 25 µm thick Teflon sheets (Goodfellow). One sheet (10 x 10 cm) is cut into 10 cm x 2 cm strips, which are further demarked into 2 cm x 2 cm squares using a permanent marker. To form an aperture, one strip is placed such that the centre of one rectangle intersects the path of a spark generated between the electrodes of a spark generator (Figure A1.6a). The generator is set to apply a potential difference of 35 kV at 0.5 Hz. 20-25 discharges are performed, successful apertures are formed when each successive spark follows the path of the first and widens the diameter of the aperture, it is immediately apparent if the attempt has been successful because there is an audibly distinct difference between a spark passing through the sheet and passing around the edges without penetrating it, which can cause damage to the sheet. The size and smoothness of the apertures and the good condition of the surrounding Teflon were confirmed using an optical microscope (Figure A1.6b).

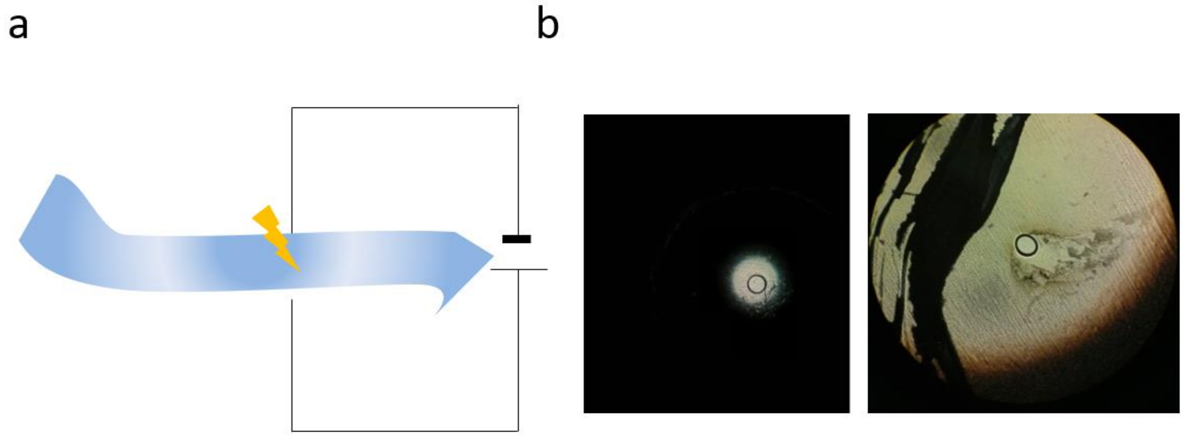

Figure A1.6 **a** The spark gap apparatus. **b** A satisfactory aperture produced using the spark gap technique , and **c** An unsatisfactory aperture displaying scorched / damaged regions around the aperture.

A1.6 Formation of stable supported lipid bilayers

In aqueous solution, at sufficiently high local concentration phospholipids will spontaneously self-assemble into bilayers, thus, a model bilayer can be formed within the 100 µm aperture in the Teflon sheet separating the wells in our experimental cell (Figure A1.7). A robust protocol for the formation of bilayers has been developed within the lab to ensure that stable bilayers can be readily and reproducibly obtained.

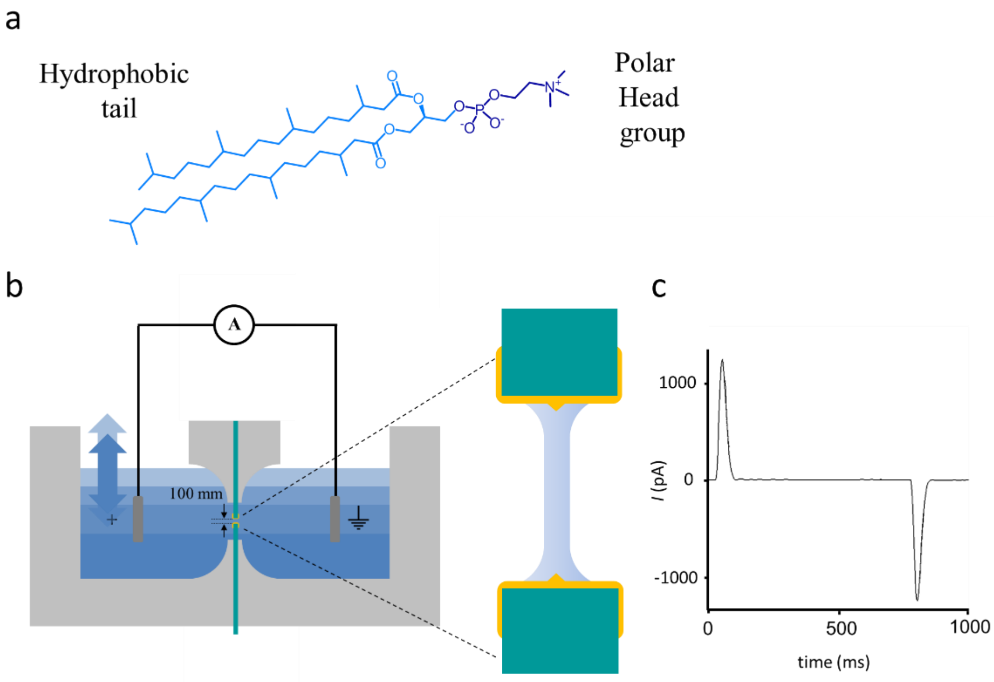

Figure A1.7 **a**. Self-assembly of phospholipid into liposomes in aqueous media. **b**. Schematic cross-section of the experimental cell used in single channel recordings, a small layer of hexadecane has been deposited on each side of the Teflon sheet by evaporation from a hanging drop ~ 5 µL of 10% solution of hexadecane in pentane. A buffered solution ~ 600 µL of KCl(aq) containing a low concentration of phospholipid (6 µL of 10 mg/mL solution in *n*-pentane) is aspirated and dispensed into each well multiple times using a Hamilton syringe to ‘paint’ a bilayer across the aperture as the level of the solution falls and rises. This causes the tail of the phospholipid to partition into the hexadecane while the polar head group remains in the aqueous phase. It is speculated that the suspended bilayer across the aperture is supported by the annulus formed by hexadecane on the rim of the aperture and separating two aqueous compartments **c**. Capacitance trace of a typical bilayer with a +/ – 1 mV pulse applied at 13.3 Hz

A1.7 Obtaining single α-HL channels rapidly and reproducibly

One popular technique involves adding a high enough concentration of α-HL to the well that a channel will insert stochastically within about an hour. However, for many nanopore experiments (such as those presented in Chapters Three to Six, which involved the assembly and investigation of complex mechanically interlocked states) it is often desirable to perform single channel recordings over a number of hours. In such cases, a concentration of α-HL sufficiently high to cause spontaneous insertion within an hour will often result in further unwanted insertions and complication of experimental data. Thus, to afford reproducible, rapid insertion of individual channels and long experimental durations we have devised a different method.

In this approach, a gel loading tip fitted to a 20 µL Gilson type pipettor is introduced into am aqueous solution of α-HL (~267 µM), without aspirating, such that a tiny amount << 1 µL of α-HL solution remains on the tip. A small LED light on a flexible stem with a magnetic base is shone into the live well such that the Teflon sheet is back illuminated and the position of a pipette tip on the opposite side of the sheet can be easily seen. The pipette tip is then submerged ~ 5 mm from the aperture in the Teflon sheet. The pipettor is then depressed to 'shoot' a bubble of air at the membrane.

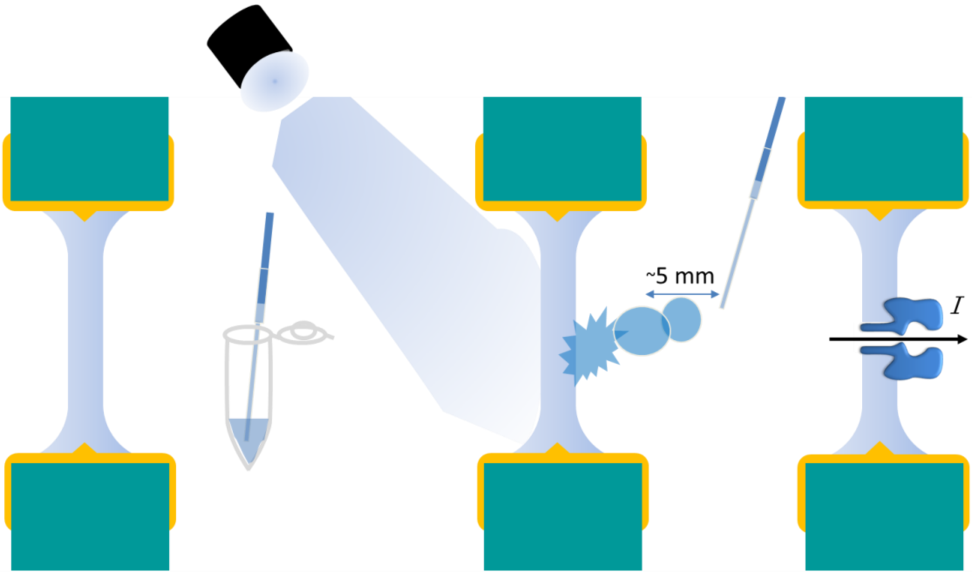

Figure A1.8 Approach used to get single channels.

This approach propels a locally high concentration of α-HL towards the membrane. This increase in local concentration (and possible associated mechanical attenuation of the membrane) is very brief. Throughout this process the concentration of α-HL is being depleted by diffusion into the relatively large volume of buffer thereby precluding the insertion of unwanted channels within an experimentally useful time frame. Using this approach it is often possible to obtain a single channel in a matter of seconds and for the system to persist in a single channel condition for many hours. By using this approach it is possible to screen many channels in a relatively brief period of time (which was useful for the studies conducted in Chapter Two, for example).

It should be noted that the approach does have limitations; the insertion of multiple channels does still occur, and the repeated application of pressure near the aperture can lead to a degradation of the bilayer and difficulty in forming a bilayer over the course of a day. This may be due to the gradual degradation of the hexadecane layer around the aperture and perhaps due to damage caused to the Teflon sheet. Accidental tearing of the Teflon by the pipette tip can occasionally occur. In addition, if multiple successive attempts have failed to obtain a suitable single channel, then the global concentration of α-HL in solution will tend to increase such that it becomes progressively more likely that undesired additional channels will insert. However on balance, the methodology described is superior to the “sit and wait” approach that would be used otherwise, and it is now the approach of choice in our lab.

A1.8 storage of materials and care of apparatus

DNA when synthesised in-house DNA was concentrated at reduced pressure by speedvac to high concentration ~ 300 µM and stored in aliquots of 5 µL in PCR tubes in press sealed plastic bags at –20 °C. Commercially obtained DNA was also reconstituted to 300 µM and stored in the same way.

α-Haemolysin was purchased from Sigma Aldrich as a lyophilised powder and reconstituted with 1.6 mL of molecular biology grade water (5 PRIME Hamburg, Germany) affording a solution of approximately 10 mM which was divided in 4 µL aliquots in PCR tubes and stored at –80 °C. No significant degradation in average channel quality was noticed over the course of greater than one year. At the beginning of a typical week of nanopore experiments one aliquot was removed from the –80 °C freezer and reconstituted with 45 µL of molecular biology grade H_2O. This sample was then subdivided into ten ~5 µL aliquots that were stored at –20 °C until needed. One of these smaller aliquots was removed and diluted with 10 µL of buffer giving a final α-HL concentration of ~ 267 µM which was then used to obtain a single channel. During a typical week, all ten aliquots would be used by a single researcher. Importantly, any unused aliquots were discarded at the end of the week as they were found to degrade at the lower concentration when held at –20 °C for over one week.

1,2-diphytanoyl-*sn*-glycero-3-phosphocholine was purchased from Avanti polar lipids as a waxy white solid. Small quantities were carefully weighed out ~ 5 mg into 1 mL glass sample vials which were then labelled with the volume of *n*-pentane required to reconstitute the lipid to a concentration of 10 µg/µL (500 µL for a 5mg portion), and were stored at – 80 °C until needed. At the start of a typical week of nanopore experiments one sample of lipid was removed from the –80 °C freezer and reconstituted with *n*-pentane and then subdivided into 50 µL aliquots in 1 mL glass sample vials. The vials were left open to the air for ~10 minutes to allow the pentane to evaporate. The aliquots were then sealed, placed in a press-seal plastic bag and stored at –20 °C until needed. One of these smaller lipid aliquots was removed from the –20 °C freezer and reconstituted with 50 µL of *n*-pentane to use each day.

Hexadecane was stored at room temperature and 50 µL was reconstituted in a 1 mL glass sample vial with *n*-pentane (450 µL) to give a 10% solution ready for use. This is replaced roughly every two weeks.

Ag/AgCl Microelectrodes purchased from Warner become increasingly prone to noise from use over time. Thus, to reduce this noise and extend the useful lifetime of each microelectrode the black AgCl surface was replenished approximately every two weeks. This was achieved by performing electrolysis in an aqueous solution of saturated KCl for ~ 1 minute at 10 V (using a gel electrophoresis power supply) where the microelectrodes served as the positive electrode and a platinum wire was used as the negative electrode.